Advancements in cardiovascular imaging: serial coronary CT and myocardial CT perfusion quantification techniques

Driest, F.Y. van

Advancements in Cardiovascular Imaging:
Serial coronary CT and myocardial CT perfusion quantification techniques

Finn Yesse van Driest

Colofon

The studies described in this thesis were conducted at the Department of Cardiology of the Leiden University Medical Center, Leiden, The Netherlands.

Financial support for this thesis by Medis Medical Imaging and Walaeus Bibliotheek are gratefully acknowledged.

Printing: Ridderprint, ridderprint.nl
Layout and design: Henry Smaal, persoonlijkproefschrift.nl

Advancements in Cardiovascular Imaging:
Serial coronary CT and myocardial CT perfusion quantification techniques

Proefschrift

ter verkrijging van
de graad van doctor aan de Universiteit Leiden,
op gezag van de (waarnemend) rector magnificus,
volgens besluit van het college voor promoties
te verdedigen op donderdag 12 februari 2026
klokke 14:30 uur
door
Finn Yesse van Driest
geboren te Den Haag
in 1990

Promotiecommissie
Promotor
Prof. Dr. J.W. Jukema

Copromotor
Dr. A.J.H.A. Scholte

Leden promotiecommissie
Prof. Dr. P.H.A. Quax
Prof. Dr. L.F. de Geus-Oei
Prof. Dr. R. Nijveldt, Radboud Universitair Medisch Centrum
Dr. S.M. Boekholdt, Amsterdam Universitair Medisch Centrum

Table of contents

1 General introduction

Coronary computed tomography angiography (CCTA) is a widely used non-invasive imaging modality in the diagnosis of coronary artery disease (CAD), allowing for both quantitative and qualitative plaque assessment (1). It fulfils a very important role in the early diagnosis of CAD which still remains one of the leading causes of mortality and loss of disability-adjusted life years worldwide (2). In recent years use of serial CCTA has emerged in which baseline and follow-up CCTA scans can be compared thus allowing for the assessment of changes in plaque burden and plaque morphology (3, 4). Serial CCTA has not only demonstrated its value in the assessment of plaque progression or regression but also in the assessment of changes in epicardial adipose tissue (EAT) in which relatively larger volumes of EAT are associated with rapid and early plaque progression (5). However, as mentioned earlier CCTA is primarily capable of quantitative and qualitative plaque assessment. Yet, the assessment of ischemic myocardium using CT myocardial perfusion (CTP) could allow for functional assessment of CAD, the latter is of importance for prognosis assessment and in the decision to revascularize patients (6, 7).

CCTA and MRI both offer advantages in the assessment of left ventricular (LV) mass and wall thickness but MRI remains the gold standard (8, 9). However, recent technological advancements in CCTA such as improved spatial resolution have enabled its application beyond coronary assessment allowing for the assessment of LV mass and wall thickness (8). This is particularly important as this may offer a resolution for patient with contraindications to MRI, such as those with cardiac implanted devices or severe claustrophobia (10).

The introduction of machine learning algorithms may further refine these imaging techniques for the assessment of LV dimensions.

This thesis focuses on the development and validation of novel CT-based methods for quantifying ischemia, quantifying plaque changes on serial CCTA and quantification of LV mass and wall thickness as opposed to the gold standard MRI. By expanding the methodological capabilities of CCTA, this research aims to support the broader application of this imaging modality in comprehensive cardiac assessment.

Role of serial coronary artery CT in the evaluation of coronary artery disease

Serial CCTA allows for a non-invasive assessment of changes in plaque burden (Figure 1) and plaque morphology as well as changes in EAT (3-5). EAT is associated with CAD development as it has been shown to share the same embryologic origin as intra-abdominal fat which in turn is associated with CAD development (11). Multiple studies using serial CCTA have shown that baseline quantitative plaque characteristics, along

with measurable changes in plaque volume, are more predictive of plaque progression and major adverse cardiac events (MACE) over time than qualitative plaque features (4, 12-14). This underlies the importance of accurate identification and risk stratification of patients at risk for future atherosclerosis progression and MACE.

Several studies have shown that serial CCTA is a viable method for evaluating plaque changes (4, 13). Nevertheless, the process of co-registering coronary vessels and analyzing plaque changes between baseline and follow-up scans continues to rely on manual techniques using anatomical landmarks (15-17). Ideally an automatic co-registration of coronary vessels would be used as has recently been developed by Cao et al(18). Yet, cut-off values for plaque progression and or regression remain to be identified. A technique for objectively evaluating plaque dynamics on CCTA involves the use of patient-specific thresholds as is demonstrated in this thesis. These thresholds are derived from calibration graphs generated using two-phase scan sets, where differences in negative and positive plaque thickness are plotted against the scan quality, measured as the contrast to noise ratio (CNR). This allows for the assessment of plaque progression using patient specific and vessel specific thresholds based on scan quality.

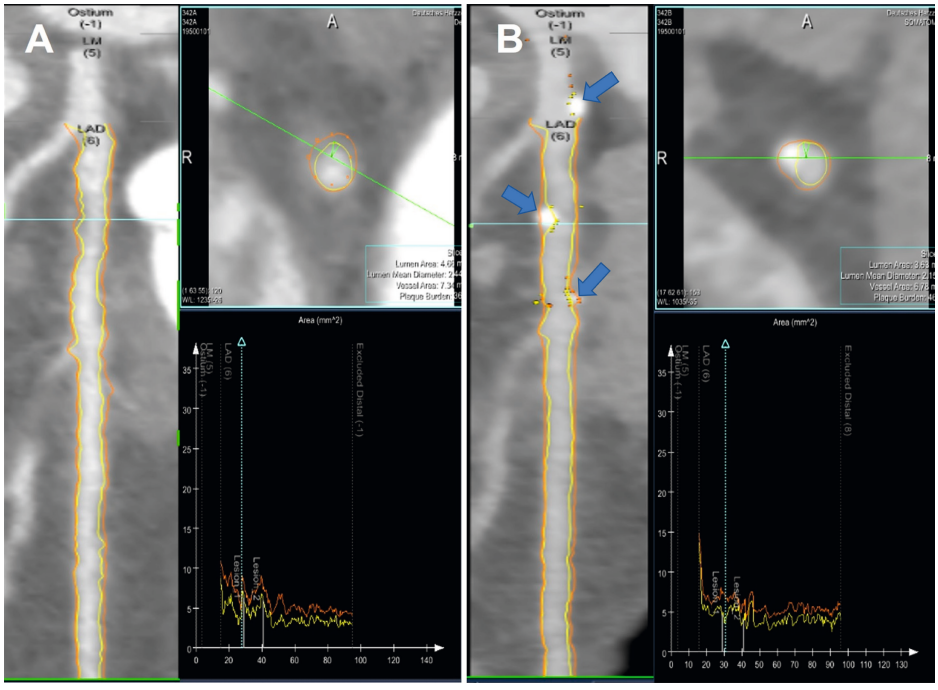

Figure 1. Example adapted from Weber et al (3). of a patient who has undergone serial CCTA in which the baseline scan is shown in panel A and the follow-up scan in panel B. A total of three newly formed calcified plaques are seen in the follow-up scan as marked by the blue arrows.

Myocardial cardiac CT perfusion and quantification

As mentioned before, CCTA is a valuable non-invasive imaging modality in CAD assessment. However, its main role involves assessment of stenosis severity. Additional CTP allows for the evaluation of ischemic myocardium which is important for prognosis and plays a key role in determining whether patients should undergo revascularization. This decision is influenced by the degree of hypoperfusion (ischemia) in the myocardium relative to the mass of myocardial tissue distal to the coronary stenosis (1, 6, 7). However, nowadays CTP is still assessed routinely by visual analysis in a semi quantitative manner. Full quantification of myocardial ischemia is discussed in this thesis using the Voronoi algorithm.

The Voronoi algorithm is a mathematical method used to partition a two-dimensional plane or three-dimensional space into regions based on the shortest distance to predefined points. Applying this algorithm to myocardial tissue allows for segmentation of the myocardium according to the supplied territory of each coronary vessel (19). Subsequently, areas of ischemia on CTP can be correlated to the corresponding area perfused by each of the coronary arteries. In the case of a severe stenosis this also allows for the correlation of the "subtended mass" to the subsequent area of ischemia. In which the subtended mass is defined as the mass of myocardial tissue supplied by a coronary artery distally from the stenosis (Figure 2).

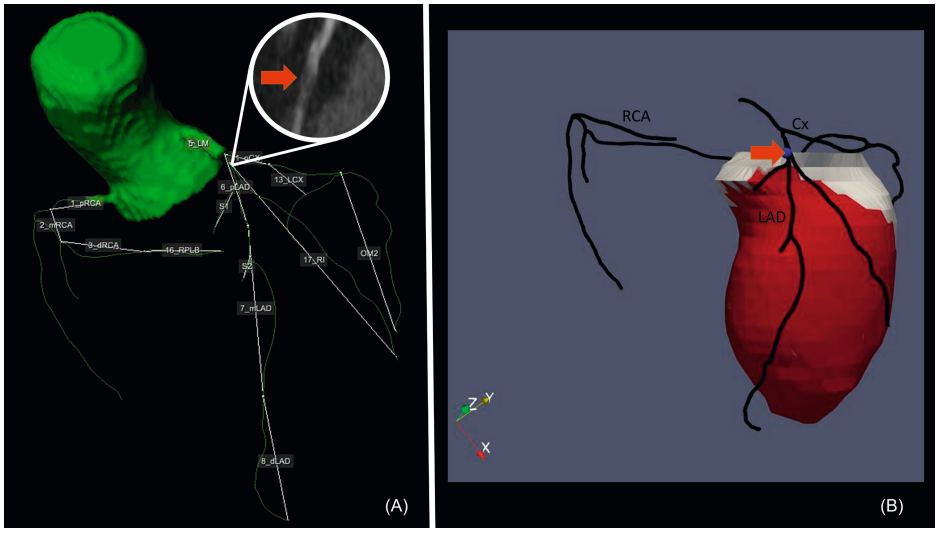

Figure 2. Example of a patient with a stenosis in the proximal left anterior descending artery (LAD) as marked by the red arrow in panel A and B. The red area in panel B represents the "subtended mass" calculated using the Voronoi algorithm.

MRI is still considered the gold standard in the assessment of LV mass and wall thickness (9). However, the high diagnostic accuracy of CCTA for the detection of CAD have made it a widely used imaging modality over the past few years (20). The role of CCTA as a tool for LV mass and LV wall thickness is less explored but would be especially beneficial for patients with contraindications for MRI (8, 10). LV dimension assessment is especially important as both LV hypertrophy and increased LV wall thickness are independent risk factors for cardiovascular morbidity and mortality, regardless of the underlying cause (21). Nowadays, advancements in artificial intelligence have opened the door for its use in LV contour placement, a crucial step of LV dimension quantification. Using AI driven algorithms for LV contour placement on both CCTA and MRI – as opposed to manual contour placement - has been regarded as a time saver (22, 23). Its applicability in the comparison of LV mass and LV wall thickness on CCTA versus MRI is explored in this thesis.

Thesis outline

Part 1 of the thesis describes the role of serial CCTA scanning in the evaluation of coronary artery disease and demonstrates a novel method for visualization of plaque differences applied to serial CCTA. **Chapter 2** presents a comprehensive review of literature on how serial CCTA may be used for the assessment of both quantitative and qualitative plaque features as predictors of plaque progression and MACE. **Chapter 3** describes a novel method for the quantification of local plaque thickness differences on CCTA using scan-quality-based-vessel-specific thresholds for the assessment of coronary plaque progression and or regression. **Part 2** focusses on methods that allow for quantification of myocardial ischemia using CTP as well as quantification of LV dimensions using artificial intelligence (AI) for contour placement. **Chapter 4** describes the relationship between quantified myocardial ischemia as assessed by CTP and the myocardial area at risk, defined as the myocardial area distal from a 50% or 70% coronary stenosis. **Chapter 5** outlines the correlation of the quantified ischemia on CTP and the myocardial area at risk. **Chapter 6** analyses the assessment of LV mass and wall thickness on CT by comparing LV mass and wall thickness measured on CT versus the gold standard of MRI using machine learning algorithms for LV contour placement.

References

1. Hoffmann U, Moselewski F, Nieman K, Jang IK, Ferencik M, Rahman AM, et al. Noninvasive assessment of plaque morphology and composition in culprit and stable lesions in acute coronary syndrome and stable lesions in stable angina by multidetector computed tomography. J Am Coll Cardiol. 2006;47(8):1655-62.
2. Roth GA, Johnson C, Abajobir A, Abd-Allah F, Abera SF, Abyu G, et al. Global, Regional, and National Burden of Cardiovascular Diseases for 10 Causes, 1990 to 2015. J Am Coll Cardiol. 2017;70(1):1-25.
3. Weber C, Deseive S, Brim G, Stocker TJ, Broersen A, Kitslaar P, et al. Coronary plaque volume and predictors for fast plaque progression assessed by serial coronary CT angiography-A single-center observational study. Eur J Radiol. 2020;123:108805.
4. Yu M, Li W, Lu Z, Wei M, Yan J, Zhang J. Quantitative baseline CT plaque characterization of unrevascularized non-culprit intermediate coronary stenosis predicts lesion volume progression and long-term prognosis: A serial CT follow-up study. Int J Cardiol. 2018;264:181-6.
5. Nakanishi K, Fukuda S, Tanaka A, Otsuka K, Jissho S, Taguchi H, et al. Persistent epicardial adipose tissue accumulation is associated with coronary plaque vulnerability and future acute coronary syndrome in non-obese subjects with coronary artery disease. Atherosclerosis. 2014;237(1):353-60.
6. Neumann FJ, Sousa-Uva M, Ahlsson A, Alfonso F, Banning AP, Benedetto U, et al. 2018 ESC/EACTS Guidelines on myocardial revascularization. Eur Heart J. 2019;40(2):87-165.
7. Vavere AL, Simon GG, George RT, Rochitte CE, Arai AE, Miller JM, et al. Diagnostic performance of combined noninvasive coronary angiography and myocardial perfusion imaging using 320 row detector computed tomography: design and implementation of the CORE320 multicenter, multinational diagnostic study. J Cardiovasc Comput Tomogr. 2011;5(6):370-81.
8. Kara B, Nayman A, Guler I, Gul EE, Koplay M, Paksoy Y. Quantitative Assessment of Left Ventricular Function and Myocardial Mass: A Comparison of Coronary CT Angiography with Cardiac MRI and Echocardiography. Pol J Radiol. 2016;81:95-102.
9. Fulton N, Rajiah P. Utility of magnetic resonance imaging in the evaluation of left ventricular thickening. Insights Imaging. 2017;8(2):279-93.
10. Sammet S. Magnetic resonance safety. Abdom Radiol (NY). 2016;41(3):444-51.
11. Psaltis PJ, Talman AH, Munnur K, Cameron JD, Ko BSH, Meredith IT, et al. Relationship between epicardial fat and quantitative coronary artery plaque progression: insights from computer tomography coronary angiography. Int J Cardiovasc Imaging. 2016;32(2):317-28.
12. Han D, Kolli KK, Al'Aref SJ, Baskaran L, van Rosendael AR, Gransar H, et al. Machine Learning Framework to Identify Individuals at Risk of Rapid Progression of Coronary Atherosclerosis: From the PARADIGM Registry. J Am Heart Assoc. 2020;9(5):e013958.
13. Lee SE, Sung JM, Andreini D, Al-Mallah MH, Budoff MJ, Cademartiri F, et al. Differences in Progression to Obstructive Lesions per High-Risk Plaque Features and Plaque Volumes With CCTA. JACC Cardiovasc Imaging. 2020;13(6):1409-17.
14. van Rosendael AR, Lin FY, van den Hoogen IJ, Ma X, Gianni U, Al Hussein Alawamlh O, et al. Progression of whole-heart Atherosclerosis by coronary CT and major adverse cardiovascular events. J Cardiovasc Comput Tomogr. 2021;15(4):322-30.
15. Lee SE, Chang HJ, Sung JM, Park HB, Heo R, Rizvi A, et al. Effects of Statins on Coronary Atherosclerotic Plaques: The PARADIGM Study. JACC Cardiovasc Imaging. 2018;11(10):1475-84.
16. Lee SE, Sung JM, Andreini D, Budoff MJ, Cademartiri F, Chinnaiyan K, et al. Differential association between the progression of coronary artery calcium score and coronary plaque volume progression according to statins: the Progression of AtheRosclerotic PlAque DetermIned by Computed TomoGraphic Angiography Imaging (PARADIGM) study. Eur Heart J Cardiovasc Imaging. 2019;20(11):1307-14.
17. Smit JM, van Rosendael AR, El Mahdiui M, Neglia D, Knuuti J, Saraste A, et al. Impact of Clinical Characteristics and Statins on Coronary Plaque Progression by Serial Computed Tomography Angiography. Circ Cardiovasc Imaging. 2020;13(3):e009750.
18. Cao Q, Broersen A, Kitslaar PH, Yuan M, Lelieveldt BPF, Dijkstra J. Automatic coronary artery plaque thickness comparison between baseline and follow-up CCTA images. Med Phys. 2020;47(3):1083-93.
19. Guibas L, Stolfi J. Primitives for the manipulation of general subdivisions and the computation of Voronoi. ACM Trans Graph. 1985;4(2):74–123.

20. Abdelrahman KM, Chen MY, Dey AK, Virmani R, Finn AV, Khamis RY, et al. Coronary Computed Tomography Angiography From Clinical Uses to Emerging Technologies: JACC State-of-the-Art Review. J Am Coll Cardiol. 2020;76(10):1226-43.
21. Haider AW, Larson MG, Benjamin EJ, Levy D. Increased left ventricular mass and hypertrophy are associated with increased risk for sudden death. J Am Coll Cardiol. 1998;32(5):1454-9.
22. Koo HJ, Lee JG, Ko JY, Lee G, Kang JW, Kim YH, et al. Automated Segmentation of Left Ventricular Myocardium on Cardiac Computed Tomography Using Deep Learning. Korean J Radiol. 2020;21(6):660-9.
23. Alabed S, Alandejani F, Dwivedi K, Karunasaagarar K, Sharkey M, Garg P, et al. Validation of Artificial Intelligence Cardiac MRI Measurements: Relationship to Heart Catheterization and Mortality Prediction. Radiology. 2022;304(3):E56.

Part 1

Role of serial coronary computed tomography angiography in the evaluation of coronary artery disease

2 Utilizing (serial) coronary computed tomography angiography (CCTA) to predict plaque progression and major adverse cardiac events (MACE): results, merits and challenges

F. Y. van Driest
C. M. Bijns
R. J. van der Geest
A. Broersen
J. Dijkstra
A. J. H. A. Scholte
J. W. Jukema

Abstract

Objectives: To present an overview of studies using serial coronary computed tomography angiography (CCTA) as a tool for finding both quantitative (changes) and qualitative plaque characteristics as well as epicardial adipose tissue (EAT) volume changes as predictors of plaque progression and/or major adverse cardiac events (MACE) and outline the challenges and advantages of using a serial non-invasive imaging approach for assessing cardiovascular prognosis.

Methods: A literature search was performed in PubMed, Embase, Web of Science, Cochrane Library and Emcare. All observational cohort studies were assessed for quality using the Newcastle–Ottawa Scale (NOS). The NOS score was then converted into Agency for Healthcare Research and Quality (AHRQ) standards: good, fair and poor.

Results: A total of 36 articles were analyzed for this review, 3 of which were meta-analyses and one was a technical paper. Quantitative baseline plaque features seem to be more predictive of MACE and/or plaque progression as compared to qualitative plaque features.

Conclusions: A critical review of the literature focusing on studies utilizing serial CCTA revealed that mainly quantitative baseline plaque features and quantitative plaque changes are predictive of MACE and/or plaque progression contrary to qualitative plaque features. Significant questions regarding the clinical implications of these specific quantitative and qualitative plaque features as well as the challenges of using serial CCTA have yet to be resolved in studies using this imaging technique.

Abbreviations

%DS: Percentage diameter stenosis
ACS: Acute coronary syndrome
CAD: Coronary artery disease
CCTA: Coronary computed tomography angiography
CI: Confidence interval
CX: Circumflex artery
EAT: Epicardial adipose tissue
EFV: Epicardial fat volume
HR: Hazard ratio
HRP: High-risk plaque features
HU: Hounsfield units
ICA: Invasive coronary angiography
IQR: Interquartile range
IVOCT: Intravascular Optical Coherence Tomography
IVUS: Intravascular Ultrasound
LAD: Left anterior descending artery
LAPV: Low-attenuation plaque volume
LAP: Low-attenuation plaque
LM: Left main
MACE: Major adverse cardiac events
OR: Odds ratio
PAV: Percentage atheroma volume
PR: Positive remodeling
TPV: Total plaque volume

1. Introduction.

Coronary artery disease (CAD) is still one of the leading causes of death and loss of disability-adjusted life years worldwide (1). The clinical course of CAD mainly consists of progression of atherosclerosis punctuated by merely unpredictable clinical events despite treatment (2). Plaque phenotypes are clinically relevant as vulnerable plaque is prone to rupture and may lead to major adverse cardiac events (MACE) (3). Also, it has been demonstrated that epicardial adipose tissue (EAT) shares the same embryologic origin as intra-abdominal fat, which is associated with CAD(4). This underlies the importance of accurate identification and risk stratification of patients at risk for future atherosclerosis progression and MACE. Besides invasive techniques such as intravascular ultrasound (IVUS), intravascular optical coherence tomography (IVOCT) and invasive coronary angiography (ICA), coronary computed tomography angiography (CCTA) is a non-invasive imaging approach that allows for both qualitative and quantitative assessment of coronary plaque (5). A previous meta-analysis has shown high correlations between CCTA features and measures of coronary plaque as compared to IVUS (6). As such, CCTA has rapidly emerged as a non-invasive tool for plaque assessment (7). More recent studies have demonstrated the ability of serial CCTA to assess changes in plaque burden and plaque morphology as well as changes in EAT volume (8-11). Use of serial CCTA may be beneficial for both symptomatic and asymptomatic patients as recent expert recommendations state that CCTA may be performed as the first-line test for evaluating patients with no known CAD who present with stable typical or atypical chest pain, or other symptoms which are thought to represent a possible anginal equivalent. Subsequently, CCTA may be performed in asymptomatic high-risk individuals, especially in those who have a higher likelihood of having a large amount of noncalcified plaque (12).

This review presents an overview of studies using serial CCTA as a tool for finding both quantitative (changes) and qualitative plaque characteristics as well as EAT volume changes as predictors of plaque progression and/or MACE and outlines the challenges and advantages of using a serial non-invasive imaging approach for assessing cardiovascular prognosis. Details regarding the search strategies, quality assessment and selection criteria can be found in the supplementary material.

2. Image analysis of serial CCTA.

Recent development in plaque quantification software allows for semiautomated methods to quantify plaque volume on a single CCTA, drastically increasing the speed of assessment (13). Plaque volumes can be automatically sub-classified by composition using predefined intensity cutoff values in Hounsfield units (HU). These predefined intensity cutoff values in HU currently available have been obtained by comparing CCTA with IVUS or by histological examination. However, cutoff values vary (14). Nowadays,

an algorithm which uses adaptive attenuation thresholds based on the principle that plaque attenuation values are influenced by luminal contrast densities may be used. These contrast densities in turn are affected by a variety of factors including cardiac output and patient body size. Furthermore, luminal contrast densities decrease along the length of vessels and are lower in vessel segments with a severe stenosis. Adaptive HU cut-off values may overcome these problems by depending on regional attenuation contrast in the lumen (14, 15). In a recent study by de Knegt et al., fixed HU cutoff values were compared to adaptive HU cutoff values. Fixed HU thresholds underestimated fibrous and fibrofatty plaque volumes and overestimated necrotic core and dense plaque volumes compared to adaptive HU thresholds. Also, volumes of dense calcium plaque differed with increasing tertiles of luminal contrast density when using fixed HU thresholds instead of using adaptive HU thresholds. This highlights the importance of using an adaptive HU threshold algorithm when evaluating plaque composition (16). An imaging example demonstrating the superiority of adaptive HU thresholds over fixed HU values is depicted in Fig. 1. When assessing serial CCTA, analysis of the same coronary segments in baseline and follow-up scans is crucial for serial plaque comparison. Several studies utilizing serial CCTA facilitate co-registration of coronary segments and lesions by using anatomical landmarks like branching vessels and distance from the ostium which is done manually by visual analysis (17-19). Figure 2 depicts an example of serial CCTA.

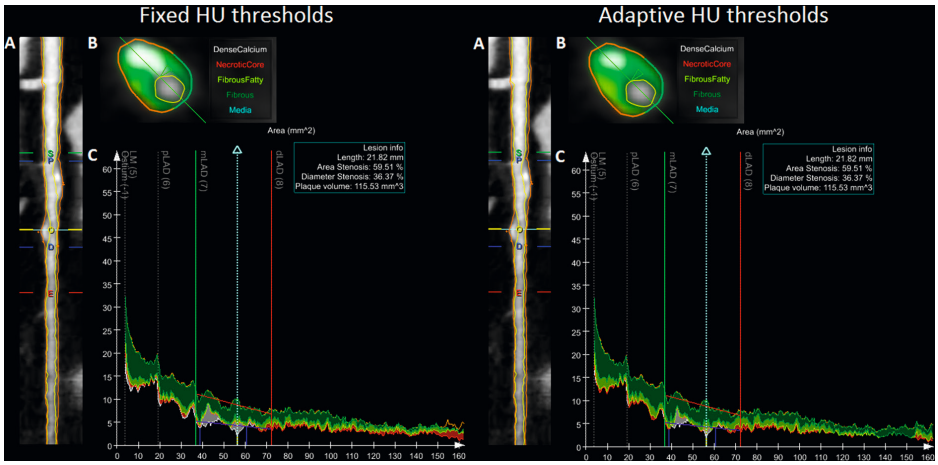

Fig 1. Example of quantitative analysis of the left anterior descending coronary artery (LAD) using fixed and adaptive HU thresholds. Panel A represents the straightened multiplanar reconstruction where S and E are the start and the end of the segment respectively; P and D are the proximal and distal borders of the lesion respectively. O represents the point of maximal obstruction. Consequently, panel B represent the transverse view of the vessel at this point. The color overlay in both the graph (Panel C) and the transverse view represents the different plaque tissue types. It must be noted that from visual assessment of the color overlay it can be seen that the fixed HU method characterized this plaque as having more dense calcium and less fibrofatty tissue compared to the adaptive method (16).

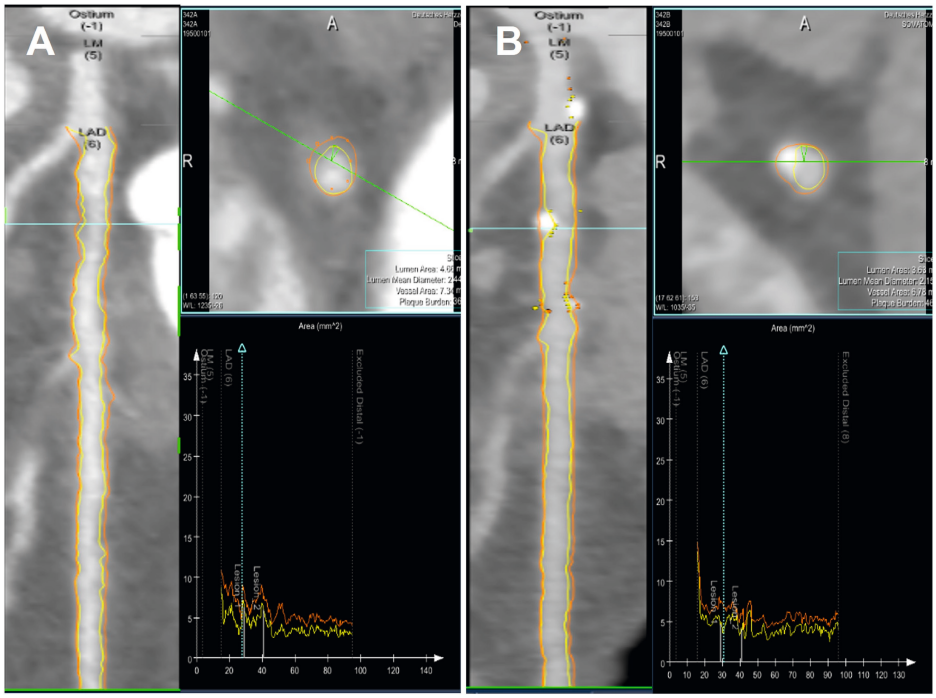

Fig 2. Example of a patient with an interscan period of six years between the baseline (shown on the left side, panel A) and follow-up scan (shown on the rights side, panel B). The investigated vessel is the left main (LM) and left anterior descending artery (LAD) demonstrating a total of three newly formed calcified plaques; one in the LM and two in the proximal segment of the LAD. In this case branching of the circumflex artery (CX) can be used as an anatomical landmark for co-registration by visual analysis. The orange line marks the outer vessel wall and the yellow line the lumen of the coronary artery (8).

3. Quantitative and qualitative plaque features.

Assessment of CCTA images can be performed on a quantitative or qualitative basis. Quantitative analysis focusses on volumetric plaque measurements such as total plaque volume (TPV), calcified or noncalcified plaque volume, low-attenuation plaque volume (LAPV) and percentage atheroma volume (PAV). The latter is calculated as a percentage by dividing the plaque volume by the vessel volume (20). Quantitative analysis on CCTA is an adequate predictor of cardiac death and the occurrence of acute coronary syndrome (ACS) (21). Qualitative analysis focusses on plaque composition based on the plaque density (attenuation). Hence, CCTA can identify different plaque components. These qualitative features include plaque composition (noncalcified or calcified) and high-risk plaque features (HRP) (22). HRP features identified by CCTA include positive remodelling (PR), low-attenuation plaque (LAP), napkin-ring sign and spotty calcification (21, 23-28). PR describes the increase in vessel diameter at the lesion site compared to a reference segment (24), often defined as a remodelling index of ≥ 1.1 (5, 9, 10, 24, 27, 29). LAP is a

noncalcified plaque with an attenuation of < 30 HU (9, 11, 25, 27, 28). The napkin-ring sign is defined as a combination of a low-attenuation core surrounded by a rim-like area of higher attenuation (9, 11, 23, 25). Lastly, spotty calcification is an intra-lesion calcific plaque < 3 mm in diameter (9, 10, 24, 27-29). A meta-analysis by Nerlekar et al. assessing the relationship between HRP features on prognosis has clearly demonstrated that all HRP features were strongly associated with MACE, including napkin-ring sign (HR, 5.06; 95% CI, 3.23–7.94; $P < 0.001$), low-attenuation plaque (HR, 2.95; 95% CI, 2.03–4.29; $P < 0.001$), positive remodelling (HR, 2.58; 95% CI, 1.84–3.61; $P < 0.001$), and spotty calcification (HR, 2.25; 95% CI, 1.26–4.04; $P = 0.006$). The presence of ≥2 HRP features had highest risk of MACE (HR, 9.17; 95% CI, 4.10–20.50; $P < 0.001$) (30). Imaging examples of HRP progression are depicted in Figs. 3 and 4.

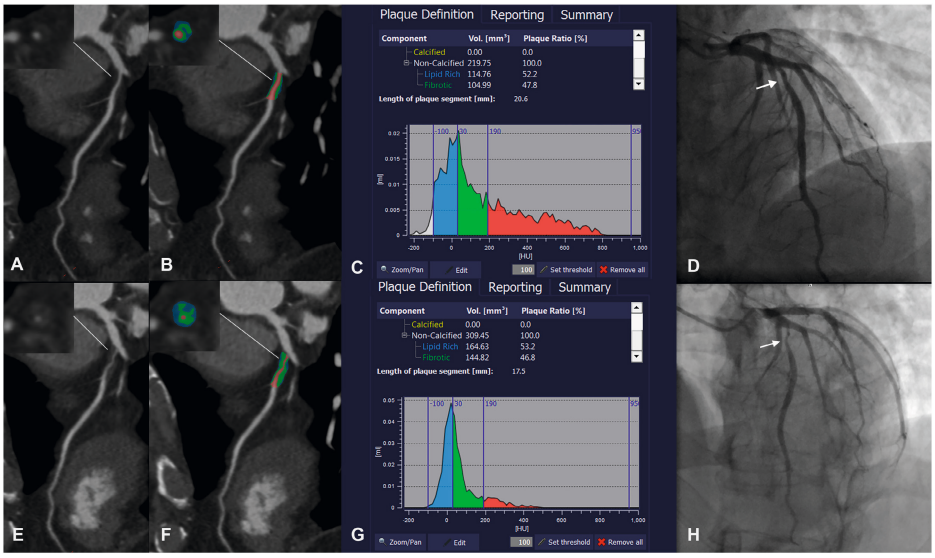

Fig 3. Example of a patient with LAP progression, a HRP feature. Panel A demonstrates a non-calcified plaque at baseline CCTA in the proximal LAD with moderate stenosis which is also visualized by baseline ICA in panel D. The colour coded image in panel B demonstrates the presence of LAP components labelled in blue. Further visualization of plaque components can be done using a histogram depicted in panel C. LAP component volume was 114.76 mm^3. At 12 month follow-up significant lesion progression with severe stenosis is observed (panel F - H). Note the increase of the LAP component volume to 164.63 mm^3 (9).

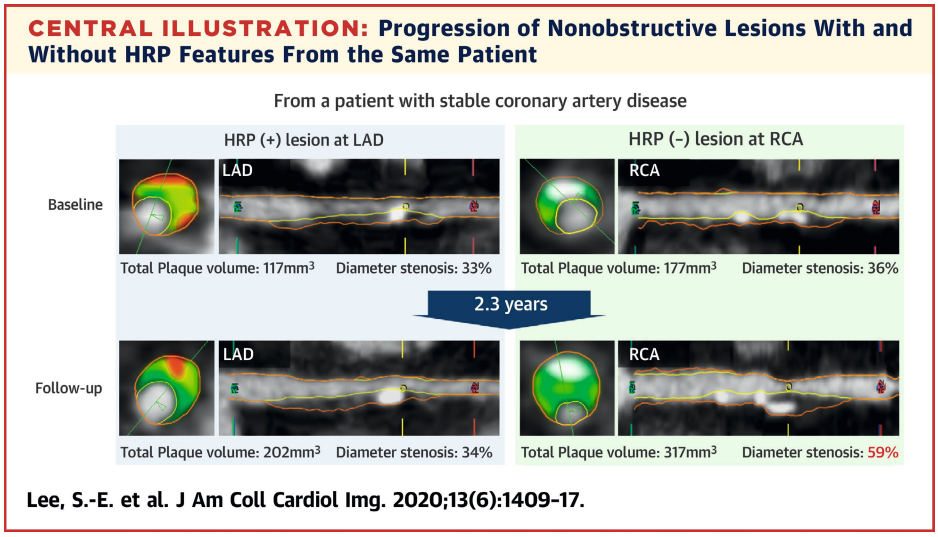

Fig 4. Example of a patient with plaque progression in a plaque with and without HRP features. A plaque in the right coronary artery (RCA) without HRP features progressed to an obstructive lesion at follow-up. Contrary, a plaque with HRP features in the LAD from the same patient remained nonobstructive at follow-up (10).

4. CCTA derived plaque features for predicting plaque progression.

Several studies have assessed the relationship between CCTA-derived quantitative and qualitative plaque features as predictors for plaque progression. (8-10, 29). In the past, serial IVUS has demonstrated the prognostic importance of plaque progression by showing an association with clinical outcomes (31). Table 1 lists details of studies utilizing serial CCTA to assess the relationship between CCTA-derived quantitative and qualitative plaque features as predictors for plaque progression and/or MACE.

In a large study by Han et al., predictors of rapid plaque progression were assessed. Rapid plaque progression was defined as an increase of baseline PAV of more than 1% per year on follow-up CCTA. A machine learning framework was used to assess several qualitative and quantitative CCTA-based plaque features. Quantitative features were the most important to predict plaque progression followed by qualitative features and last clinical/laboratory features. Specifically, the PAV at baseline was the most important predictor (information gain value: 0.193, regression coefficient (β): 0.529; $p < 0.01$). (29). Lee et al. assessed the progression from non-obstructive lesions to obstructive lesions compared to the presence of high-risk plaque features. Both total PAV and percentage diameter stenosis (%DS) at baseline were significant risk factors for the development of obstructive lesions (HR, 1.04 [95%CI, 1.02-1.07], and HR, 1.07 [95%CI, 1.04-1.10], respectively; all p <

0.05). Interestingly, the presence of high-risk plaque features was not a significant risk factor (p = 0.433). In lesions without HRP features, baseline total PAV (HR, 1.035 [95%CI, 1.002-1.067]; p = 0.031) and baseline %DS (HR, 1.081 [95%CI, 1.049-1.115]; p < 0.001) were independent predictors for development of obstructive lesions. However, in lesions with HRP features, only baseline total PAV independently predicted progression to obstructive lesions (HR: 1.102 [95%CI: 1.035-1.174]; p = 0.003) (10). Weber et al. also demonstrated the importance of quantitative plaque features as a significant correlation between baseline TPV and TPV progression (spearman's rho = 0.33; p < 0.01). The progression in TPV was mainly determined by a progression of calcified plaque volume (7.6 mm^3 [interquartile ranges 0.2 and 33.6] vs. 16.6 mm^3 [interquartile ranges 1.8 and 62.1]; p < 0.01). Also, patients with obstructive CAD at follow-up had a significantly higher TPV at baseline (384.9 mm^3 [interquartile ranges 182.8 and 538.1] vs. 45.1 mm^3 [interquartile ranges 10.3 and 102.9]; p < 0.01) (8). Yu et al. reported predictors for plaque progression assessed at serial CCTA in patients with solely non-culprit intermediate stenoses. LAP at baseline was an independent predictor of lesion volume progression at follow-up (OR, 16.74 [95%CI, 5.02-55.84]; p < 0.001) (9). Lee et al. demonstrated that adding HRP features to a per-lesion predictive model for developing obstructive lesions containing plaque volume and clinical risk factors increased the C-statistic from 0.830 [95% CI: 0.828-0.833] to 0.895 [95% CI: 0.893-0.897]; p = 0.003. Also, the per lesion HRP feature model was significantly better than the per-patient HRP feature model (C-statistic: 0.825 [95% CI, 0.823-0.827] vs. 0.895 [95% CI, 0.893-0.897], p < 0.001) (32).

Table 1. Studies utilizing serial CCTA to assess the relationship between CCTA derived quantitative and qualitative plaque features as predictors for plaque progression and/or MACE

Study	Year	Number of patients analyzed	Design	CT technique	Image analysis	Interscan interval	Population	Endpoint(s)	Most important predictor(s)
Han et al. (29)	2020	1,083	Prospective	≥64 slice	Semiautomated	Median: 3.3 years (IQR: 2.6-4.8)	Patients with 2 CCTA scans with ≥ 2-year interval.	Rapid plaque progression	PAV at baseline (information gain value: 0.193, regression coefficient (β): 0.529; p<0.01)
Weber et al. (8)	2020	350	Retrospective	16-slice CT, 64-slice single source & 64-slice dual source	Semiautomated & automated	Median: 42 months (IQR: 23-69)	Patients with suspected obstructive CAD based on clinical presentation.	TPV progression	TPV at baseline (spearman's rho = 0.33; p<0.01) Calcified plaque volume (baseline: 7.6 mm^3 [IQR: 0.2 and 33.6] vs. follow-up: 16.6 mm^3 [IQR: 1.8 and 62.1]; p<0.01)
								Obstructive CAD	TPV at baseline (384.9 mm3 [IQR: 182.8 and 538.1] vs. 45.1 mm3 [IQR: 10.3 and 102.9]; p<0.01
Yu et al. (9)	2018	140	Prospective	128-slice single source multi-detector CT	Manual, semiautomated & automated	Mean: 14.6 ± 2.2 months	Patients with stable angina or atypical chest pain with one unrevascularized intermediate coronary stenosis considered a non-culprit lesion.	Lesion volume progression	LAP at baseline (multivariate analysis: OR 16.74 (5.02-55.84); p<0.001)
								MACE	Higher prevalence of baseline LAP (40.00% vs. 12.80%; p = 0.015). Lesion volume progression (Kaplan-Meier curve: 56.25% vs. 4.84%; log-rank p<0.001
Lee et al. (10)	2020	1,297	Prospective	≥64 slice	Semiautomated	Mean: 3.8 ± 1.6 years	Patients with 2 CCTA scans with ≥ 2-year interval.	Plaque progression	PAV and %DS at baseline (HR (95% CI): 1.04 (1.02 - 1.07), and HR (95% CI): 1.07 (1.04 - 1.10), respectively; all p < 0.05) Lesions without HRP at baseline; total PAV (HR (95%CI): 1.035 (1.002-1.067); p=0.031) and baseline %DS (HR (95%CI): 1.081 (1.049-1.115); p<0.001) Lesions with HRP features; baseline total PAV (HR (95%CI) 1.102 (1.035-1.174); p=0.003)

Study	Year	Number of patients analyzed	Design	CT technique	Image analysis	Interscan interval	Population	Endpoint(s)	Most important predictor(s)
Psaltis et al. (4)	2016	64	Retrospective	320-row multidetector CT	Manual & semiautomated	Median: 25.2 months	Patients with chest pain, dyspnea in stable setting and no ACS.	Plaque progression or development	Higher baseline EFV (β co-efficient 0.014, 95% CI: 0.003–0.026; p = 0.014)
You et al. (33)	2016	87	Retrospective	64-slice CT & 128-slice dual-source CT	Manual & semiautomated	Mean: 25.5 ± 15.7 months	Patients with at least one baseline CCTA artery plaque.	Increase of lipid-rich plaque volume	Baseline indexed EFV (multivariate analysis: OR: 1.029 [95% CI: 1.005–1.053]; p = 0.016)
Nakanishi et al. (11)	2014	517	Prospective	64-slice CT	Manual & automated	Mean: 12 ± 5 months.	Non-obese patients undergoing serial multidetector CCTA for the evaluation of CAD.	Increased prevalence of obstructive plaques and plaques with PR and LAP	Increase in EAT volume (p<0.001, p<0.001, p=0.001, respectively)
Motoyama et al. (34)	2015	423	Retrospective	320-slice CT, 64-slice CT & 16-slice CT	Manual	Median: 1 year	Patients undergoing consecutive CCTA for suspected or known CAD.	MACE	Plaque progression (Kaplan-Meier curve: 14.3% vs. 0.3%, log-rank p<0.0001) Both HRP features at baseline and plaque progression at follow-up (Kaplan-Meier curve: 27%, log-rank p<0.0001) Non-HRP lesions developing in HRP lesions with a significant stenosis at follow-up (3 out of a total of 9 ACS events (15.4%))
Rosendaelet al. (35)	2020	1166	Prospective	≥64 slice	Semiautomated	At least 2 years	Patients with 2 CCTA scans with ≥ 2-year interval.	MACE	>1.0% ΔPAV increase per year: 27.2% vs. <1.0% ΔPAV increase per year: 9.5% at 10 years (Kaplan-Meier curve, log-rank p<0.001) <1.0% ΔPAV increase per year + low baseline PAV: 6.5% vs. >1.0% ΔPAV increase per year + high baseline PAV: 30.2% (Kaplan-Meier curve, log-rank p<0.001)

Study	Year	Number of patients analyzed	Design	CT technique	Image analysis	Interscan interval	Population	Endpoint(s)	Most important predictor(s)
Lee et al. (32)	2020	1297	Prospective	≥64 slice	Semiautomated	Mean: 3.8 ± 1.6 years	Patients with 2 CCTA scans with ≥ 2-year interval.	Obstructive CAD	Per lesion analysis: Adding HRP features to a predictive model containing plaque volume and clinical risk factors increased the C-statistic to 0.895 [95% CI: 0.893-0.897]; p=0.003
Gu et al. (36)	2020	757	Retrospective	64-slice dual-source CT	Manual	Mean: 2.0 years	Patients with non-obstructive CAD, who underwent a 2nd CCTA requested by the treating physician or had new/worsening symptoms.	MACE	Three vessel plaque progression (HR: 2.37, p=0.026) Severe proximal plaque progression (HR: 3.65, p=0.003)

Table 1. TPV: Total plaque volume. LAP: Low attenuation plaque. PAV: Percent atheroma volume. %DS: Percentage diameter stenosis. EFV: Epicardial fat volume. MACE: Major adverse cardiac events. CAD: Coronary artery disease. HRP: High risk plaque. CT: Computed tomography. CCTA: Coronary computed tomography angiography. PR: Positive remodelling. EAT: Epicardial adipose tissue. IQR: Interquartile range. ACS: Acute coronary syndrome. OR: Odds ratio. HR: Hazard ratio. CI: Confidence interval.

4.1. Epicardial adipose tissue.

Numerous studies investigated the relationship between EAT and coronary artery plaque progression (4, 11, 33). EAT is a metabolically active organ that shares the same embryologic origin as intra-abdominal fat, which is associated with CAD. Under pathological circumstances, EAT has been shown to be a rich source of inflammatory adipokines. Given that inflammation is a fundamental component of the atherosclerotic process, it is postulated that EAT may influence the development and progression of coronary artery disease by contributing to the local inflammatory burden within and around atherosclerotic plaque (4). Psaltis et al. assessed the relationship between epicardial fat volume (EFV) and coronary artery plaque progression; higher baseline EFV was associated with the progression or development of coronary artery plaque (β coefficient 0.014 [95%CI, 0.003–0.026]; p = 0.014). Interestingly, change in EFV over time was not (p = 0.860) (4). You et al. also found that baseline indexed epicardial fat volume was an independent predictor of rapid increase in lipid-rich plaque volume (OR, 1.029 [95% CI, 1.005–1.053]; p = 0.016). Nevertheless, annual changes in indexed epicardial fat volume were not associated with parallel changes in lipid-rich, fibrous or calcified coronary plaque volume (p = 0.286, p = 0.500, p = 0.096; respectively) (33). However, both studies contained patients that were overweight at baseline (BMI (kg/m^2) ± SD: 29.3 ± 5.8 for Psaltis et al and 25.1 ± 3.3 for You et al). On the contrary, Nakanishi et al. solely focused on non-obese patients and demonstrated that increase of EAT volume (>10 mL) during follow-up was associated with an increased prevalence of obstructive plaques (p < 0.001) and plaques with high-risk features, such as PR (p < 0.001) and LAP (p = 0.001), in non-obese patients with CAD (11). Figure 5 depicts an example of EAT analysis.

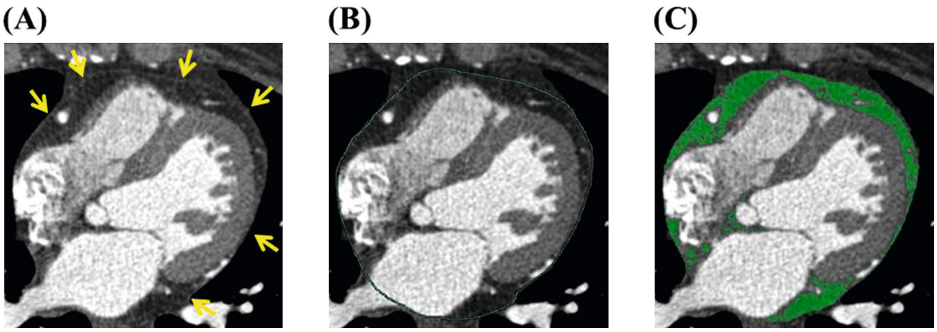

Fig 5. An example representing the measurement of EAT volume. The yellow arrows in panel A represent the pericardium in a cross-sectional slice. Segmentation of the EAT is achieved by tracing the pericardium in the axial view represented by the green line (Panel B). Subsequently, the adipose tissue can be identified by using threshold attenuation values of 30 to 250 HU which is represented by the green area in panel C (11).

4.2. CCTA derived plaque features for predicting MACE.

High-risk features of plaque such as PR, LAP and spotty calcification are found to be linked to plaque rupture and MACE (34). Multiple studies have investigated the relationship between CCTA-derived features of plaque and MACE on serial CCTA (9, 11, 34). Yu et al. (9) found that patients with MACE showed a statistically significant higher prevalence of LAP at baseline compared to patients in the MACE-absent subgroup (40.0% vs. 12.8%; p = 0.015). Prevalence of spotty calcification, napkin-ring sign and PR was not statistically different between the MACE and MACE-absent subgroups (13.33% vs. 6.40%, p = 0.291; 46.67% vs. 28.00%, p = 0.147; 73.33% vs. 60.00%, p = 0.406; respectively). Interestingly, also no significant difference existed between the two groups with regard to quantitative plaque features such as TPV, lesion length and diameter stenosis (44.6 mm^3 vs. 46.3 mm^3, p = 0.479; 10.5 mm vs. 13.0 mm, p = 0.166; 55.0% vs. 62.0%, p = 0.077, respectively for the MACE and MACE-absent subgroups). Yet, the lesion volume progression subgroup showed a higher incidence of MACE compared to the non-lesion progression subgroup (56.25% vs. 4.84%; log-rank p < 0.001). Notably, the MACE subgroup was small (15/140) (9). Motoyama et al. described that patients with plaque progression had a significantly higher incidence of MACE (14.3% vs. 0.3%, log-rank p<0.0001). Also, when classified in groups according to the presence of HRP features, the patients with both HRP at baseline CCTA and plaque progression at follow-up showed the highest frequency of MACE (27%, log-rank p < 0.0001). Conversely, in patients with HRP lesions at baseline which did not progress during follow-up, MACE did not occur. Interestingly, non-HRP lesions also led to MACE and the ones that progressed over time on a volumetric basis and evolved from non-HRP to HRP were more likely to result in MACE (3 out of a total of 9 events (15.4%)) (34). Rosendael et al. demonstrated that at 10 years, patients with an increase of >1.0% PAV/year had a higher risk of MACE compared to patients with an increase of <1.0% PAV/year (27.2% vs. 9.5%; log-rank p < 0.001). Patients were further stratified by the median baseline PAV. Patients with an increase <1.0% PAV/year and low baseline PAV experienced the lowest rates of MACE at 10 years, whilst those above the median baseline PAV and >1.0% increase in PAV/year experienced the most events (6.5% vs. 30.2%, p < 0.001) (35). Gu et al. identified patients with non-obstructive CAD who underwent a second CCTA. Those who developed any plaques coexisting in the left anterior descending, the left circumflex, and the right coronary artery (three-vessel plaque progression) between the two scans had an increased chance of MACE (HR, 2.37, p = 0.026). Furthermore, patients having a nonobstructive proximal lesion in the left anterior descending, left circumflex, or the right coronary artery, which developed in a ≥70% stenosis (severe proximal plaque progression) between the two scans, also had an increased chance of MACE (HR, 3.65, p = 0.003) (36)

5. Therapeutic measures to decrease plaque progression.

Several studies utilized serial CCTA to assess the effect of different medical therapies -mostly statins- on plaque progression (17, 19, 37, 38). Zeb et al. demonstrated that statin use causes a significant decrease of both LAP and noncalcified plaque volumes (–12.2 ± 19.2 vs. 5.9 mm^3 ± 23.1, $p < 0.0001$ and –47.7 ± 71.9 vs. 13.8 mm^3 ± 76.6, $p < 0.001$, respectively, for statin and non-statin users) and a non-statistically significant increase in the amount of calcified plaque volume in statin users compared to non-statin users (37). Smit et al. also demonstrated that statin use was associated with a significant reduction of noncalcified plaque progression (1.0±16.0 vs. 6.4±13.9 mm^3; P=0.049) compared to non-statin users. Statin users in turn showed an increase in calcified plaque progression (9.0±12.2 vs. 3.3±8.6 mm^3; P = 0.001) (19). A study by Lee et al. utilizing the large PARADIGM registry also demonstrated that over time statin therapy increased plaque calcification and reduced HRP features as lesions in statin-taking patients experienced higher annualized progression of calcified PAV (1.27 ± 1.54 mm^3 per year vs. 0.98 ± 1.27 mm^3 per year, respectively; $p < 0.001$) but slower progression of noncalcified PAV than lesions in statin-naive patients (0.49 ± 2.39 mm^3 per year vs. 1.06 ± 2.42 mm^3 per year, respectively; $p < 0.001$) (17). At baseline CCTA, statin-taking patients exhibited a higher prevalence of HRP, PR and spotty calcification (13.7% vs. 10.0%; 56.0% vs. 47.6%; and 10.2% vs. 6.8%, respectively; all $p < 0.05$), with no differences in LAP (8.5% vs. 8.4%, respectively; $p = 0.95$). The annualized incidence of HRP, PR, spotty calcification and LAP were lower (0.9% per year vs. 1.6% per year; 5.2% per year vs. 7.2% per year; 0.2% per year vs. 0.5% per year; and 0.8% per year vs. 1.0% per year, respectively; $p < 0.001$ for all) for statin- versus non-statin-taking patients respectively (17). It must be noted that differences in baseline characteristics between the statin- and non-statin-taking groups may have impacted results.

Li et al. demonstrated that not solely statin use but also statin dosage plays a key role in aiding plaque regression as patients receiving intensive statin therapy demonstrated significantly higher annualized regression of LAP volume, TPV and % plaque volume compared to patients receiving moderate statin therapy. Interestingly, a higher baseline LAP volume was also associated with higher TPV regression (P<0.001). Thus, patients with greater baseline LAP volume were more likely to benefit from statin therapy (38). Figure 6 depicts an imaging example of assessment of therapy efficacy on plaque presence using serial CCTA.

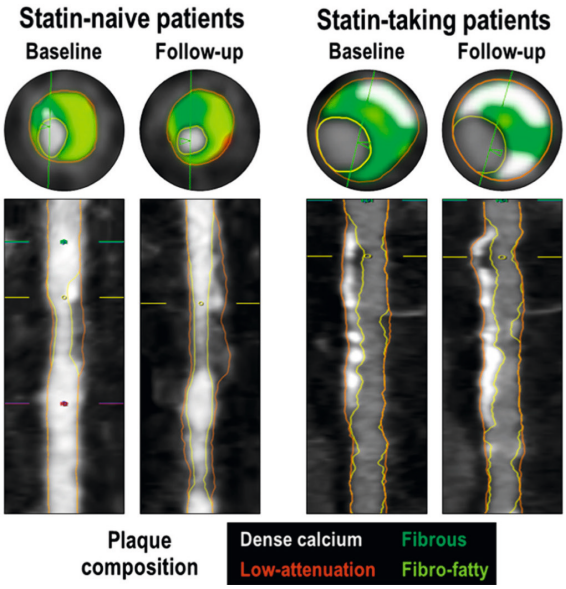

Fig 6. CCTA images of lesions at baseline and follow-up among statin-naïve patients and statin-taking patients. Statin taking patients expressed slower progression of noncalcified PAV compared to statin-naïve patients. Noncalcified PAV is the summation of fibrous, fibro-fatty and low attenuation PAV (17).

6. Benefits and challenges of serial CCTA.

A critical challenge in serial CCTA is the wide range of commercially available CT scanners and the rapid technological developments. Several studies used different scanner types with different specifications and performance at baseline and at follow-up (8, 10, 29, 33, 34). Symons et al. performed a systemic comparison of scanner variability in serial CCTA, in which plaque volume was measured with the same or a different CCTA scanner within 30 days. Plaque volume variability was ±18.4% (coefficient of variation) when the same scanner was used at baseline and follow-up, whilst the plaque volume variability was ±29.9% when different scanners were used (39). This highlights the importance of standardized CCTA protocols in future prospective studies.

No professional society guidelines dictate the methods for the routine usage of serial CCTA for evaluating progression of CAD. Therefore, it remains unclear which choice of endpoint measurement is the most appropriate (40). The usage of different endpoints could impede study comparison. Furthermore, the ideal inter-scan interval remains unclear. However, one may conclude that a relatively short inter-scan interval may inhibit the detection of newly formed plaques. On the contrary, a relatively long inter-scan interval may contribute to different CCTA protocols being used. As is observed from numerous studies cited in this review, one may propose that an inter-scan interval of at least 1-2 years would seem reasonable.

Development and implementation of radiation dose reduction tools for coronary CCTA have rapidly been expanded as high radiation exposure is known to increase the risk of cancer. As noted in the SCCT guidelines on radiation dose and dose-optimization strategies in cardiovascular CT, several scanner settings such as tube current and tube potential should be kept to a minimum to limit radiation exposure whilst also maintaining adequate image quality (41).

Currently, all studies utilizing serial CCTA for plaque progression are using visual analysis of anatomical landmarks and vessel branches for alignment between baseline and follow-up CCTA. Hence, automatic co-registration would be feasible to match corresponding points on the coronary tree in the baseline and follow-up scan. This has recently been demonstrated by Cao et al. but remains to be tested in a clinical setting (42).

Despite its challenges, serial CCTA has emerged as an important non-invasive imaging technique to track the effectiveness of medication on coronary plaque progression. In a review by Taron et al., the authors showed that serial CCTA could successfully demonstrate the efficacy of anti-atherosclerotic treatments (40) and Dahal et al. have demonstrated the importance of serial CCTA in tracking coronary atheroma progression in studies using new pharmacotherapies (43). Furthermore, when combining therapies and cardiovascular outcomes, serial CCTA can give an insight in the mechanistic correlations of coronary atherogenesis (44). Current benefits and challenges of serial CCTA are reported in Table 2.

Table 2. Benefits and challenges of serial CCTA

Benefits	**Challenges**
Assessment of changes in plaque burden and plaque morphology.	Establishing low radiation protocols to prevent unnecessary exposure during successive CCTA's.
Predicting (rapid) plaque progression and/or MACE.	Currently no consensus on endpoint measurements.
Semiautomated measurements allows objective sequential measurements.	Usage of different CT-scanners at baseline and follow-up.
Measuring the effect of different medical therapies on plaque progression.	The ideal interscan interval remains unclear.
Giving an insight in mechanistic correlations of coronary atherogenesis	Automatic co-registration to match corresponding points on the coronary tree in the baseline and follow-up scan instead of using visual analysis of anatomical landmarks.
	Implementation of machine learning for plaque analysis.

Table 2. MACE: Major adverse cardiac events. CCTA: Coronary computed tomography angiography. CT: Computed tomography.

7. Conclusions.

Serial CCTA has rapidly emerged as the non-invasive modality to track atherosclerotic plaque changes and to assess the impact of different treatment strategies on CAD. Multiple studies utilizing serial CCTA have demonstrated that baseline quantitative plaque features as well as quantitative plaque changes -contrary to qualitative plaque features- are the most important in predicting plaque progression and MACE over time. However, it must be noted that although statistically quantitative plaque features remain the most important predictors of cardiovascular prognosis, qualitative features also have a substantial contribution. Furthermore, use of serial CCTA has been proven to be useful in the assessment of (statin) therapy efficacy on plaque progression and has revealed that statins slowed the overall progression of coronary atherosclerosis volume with increased plaque calcification and reduction of HRP features.

For optimal interpretation of serial CCTA, the following suggestions can be taken into consideration. First, the use of standardized acquisition protocols for both baseline and follow-up CT scans seems preferable, as well as adaptive HU threshold algorithms for the evaluation of plaque composition. Second, to date, no expert consensus has been available on the ideal inter-scan interval between baseline and follow-up CT scan. However, based on current studies, this interval could potentially be set at 1-2 years. Third, it seems favourable to quantify plaque as automated as possible. It should, however, be stressed that for now serial CCTA solely remains an important research tool for identifying surrogate endpoints predictive of MACE and is unlikely to feature as part of the clinical workup of patients. Ultimately, serial CCTA is a promising technique for the evaluation of cardiovascular prognosis yet technical details remain to be refined.

References.

1. Roth GA, Johnson C, Abajobir A, Abd-Allah F, Abera SF, Abyu G, et al. Global, Regional, and National Burden of Cardiovascular Diseases for 10 Causes, 1990 to 2015. J Am Coll Cardiol. 2017;70(1):1-25.
2. Camargo GC, Rothstein T, Derenne ME, Sabioni L, Lima JAC, Lima RSL, et al. Factors Associated With Coronary Artery Disease Progression Assessed By Serial Coronary Computed Tomography Angiography. Arq Bras Cardiol. 2017;108(5):396-404.
3. Virmani R, Burke AP, Farb A, Kolodgie FD. Pathology of the vulnerable plaque. J Am Coll Cardiol. 2006;47(8 Suppl):C13-8.
4. Psaltis PJ, Talman AH, Munnur K, Cameron JD, Ko BSH, Meredith IT, et al. Relationship between epicardial fat and quantitative coronary artery plaque progression: insights from computer tomography coronary angiography. International Journal of Cardiovascular Imaging. 2016;32(2):317-28.
5. Hoffmann U, Moselewski F, Nieman K, Jang IK, Ferencik M, Rahman AM, et al. Noninvasive assessment of plaque morphology and composition in culprit and stable lesions in acute coronary syndrome and stable lesions in stable angina by multidetector computed tomography. J Am Coll Cardiol. 2006;47(8):1655-62.
6. Fischer C, Hulten E, Belur P, Smith R, Voros S, Villines TC. Coronary CT angiography versus intravascular ultrasound for estimation of coronary stenosis and atherosclerotic plaque burden: a meta-analysis. J Cardiovasc Comput Tomogr. 2013;7(4):256-66.
7. Knuuti J, Ballo H, Juarez-Orozco LE, Saraste A, Kolh P, Rutjes AWS, et al. The performance of non-invasive tests to rule-in and rule-out significant coronary artery stenosis in patients with stable angina: a meta-analysis focused on post-test disease probability. Eur Heart J. 2018;39(35):3322-30.
8. Weber C, Deseive S, Brim G, Stocker TJ, Broersen A, Kitslaar P, et al. Coronary plaque volume and predictors for fast plaque progression assessed by serial coronary CT angiography-A single-center observational study. Eur J Radiol. 2020;123:108805.
9. Yu M, Li W, Lu Z, Wei M, Yan J, Zhang J. Quantitative baseline CT plaque characterization of unrevascularized non-culprit intermediate coronary stenosis predicts lesion volume progression and long-term prognosis: A serial CT follow-up study. Int J Cardiol. 2018;264:181-6.
10. Lee SE, Sung JM, Andreini D, Al-Mallah MH, Budoff MJ, Cademartiri F, et al. Differences in Progression to Obstructive Lesions per High-Risk Plaque Features and Plaque Volumes With CCTA. JACC Cardiovasc Imaging. 2019.
11. Nakanishi K, Fukuda S, Tanaka A, Otsuka K, Jissho S, Taguchi H, et al. Persistent epicardial adipose tissue accumulation is associated with coronary plaque vulnerability and future acute coronary syndrome in non-obese subjects with coronary artery disease. Atherosclerosis. 2014;237(1):353-60.
12. Narula J, Chandrashekhar Y, Ahmadi A, Abbara S, Berman DS, Blankstein R, et al. SCCT 2021 Expert Consensus Document on Coronary Computed Tomographic Angiography: A Report of the Society of Cardiovascular Computed Tomography. Journal of Cardiovascular Computed Tomography. 2021;15(3):192-217.
13. Papadopoulou SL, Garcia-Garcia HM, Rossi A, Girasis C, Dharampal AS, Kitslaar PH, et al. Reproducibility of computed tomography angiography data analysis using semiautomated plaque quantification software: implications for the design of longitudinal studies. Int J Cardiovasc Imaging. 2013;29(5):1095-104.
14. de Graaf MA, Broersen A, Kitslaar PH, Roos CJ, Dijkstra J, Lelieveldt BP, et al. Automatic quantification and characterization of coronary atherosclerosis with computed tomography coronary angiography: cross-correlation with intravascular ultrasound virtual histology. Int J Cardiovasc Imaging. 2013;29(5):1177-90.
15. Dalager MG, Bottcher M, Andersen G, Thygesen J, Pedersen EM, Dejbjerg L, et al. Impact of luminal density on plaque classification by CT coronary angiography. Int J Cardiovasc Imaging. 2011;27(4):593-600.
16. de Knegt MC, Haugen M, Jensen AK, Linde JJ, Kuhl JT, Hove JD, et al. Coronary plaque composition assessed by cardiac computed tomography using adaptive Hounsfield unit thresholds. Clin Imaging. 2019;57:7-14.
17. Lee SE, Chang HJ, Sung JM, Park HB, Heo R, Rizvi A, et al. Effects of Statins on Coronary Atherosclerotic Plaques: The PARADIGM Study. JACC Cardiovasc Imaging. 2018;11(10):1475-84.
18. Lee SE, Sung JM, Andreini D, Budoff MJ, Cademartiri F, Chinnaiyan K, et al. Differential association between the progression of coronary

artery calcium score and coronary plaque volume progression according to statins: the Progression of AtheRosclerotic PlAque DetermIned by Computed TomoGraphic Angiography Imaging (PARADIGM) study. Eur Heart J Cardiovasc Imaging. 2019;20(11):1307-14.
19. Smit JM, van Rosendael AR, El Mahdiui M, Neglia D, Knuuti J, Saraste A, et al. Impact of Clinical Characteristics and Statins on Coronary Plaque Progression by Serial Computed Tomography Angiography. Circ-Cardiovasc Imaging. 2020;13(3):9.
20. van Rosendael AR, Lin FY, Ma X, van den Hoogen IJ, Gianni U, Al Hussein O, et al. Percent atheroma volume: Optimal variable to report whole-heart atherosclerotic plaque burden with coronary CTA, the PARADIGM study. J Cardiovasc Comput Tomogr. 2020.
21. Deseive S, Straub R, Kupke M, Nadjiri J, Broersen A, Kitslaar PH, et al. Automated Quantification of Coronary Plaque Volume From CT Angiography Improves CV Risk Prediction at Long-Term Follow-Up. JACC: Cardiovascular Imaging. 2018;11(2):280-2.
22. Hadamitzky M, Taubert S, Deseive S, Byrne RA, Martinoff S, Schomig A, et al. Prognostic value of coronary computed tomography angiography during 5 years of follow-up in patients with suspected coronary artery disease. Eur Heart J. 2013;34(42):3277-85.
23. Maurovich-Horvat P, Schlett CL, Alkadhi H, Nakano M, Otsuka F, Stolzmann P, et al. The Napkin-Ring Sign Indicates Advanced Atherosclerotic Lesions in Coronary CT Angiography. JACC: Cardiovascular Imaging. 2012;5(12):1243-52.
24. Motoyama S, Kondo T, Sarai M, Sugiura A, Harigaya H, Sato T, et al. Multislice Computed Tomographic Characteristics of Coronary Lesions in Acute Coronary Syndromes. Journal of the American College of Cardiology. 2007;50(4):319-26.
25. Otsuka K, Fukuda S, Tanaka A, Nakanishi K, Taguchi H, Yoshikawa J, et al. Napkin-Ring Sign on Coronary CT Angiography for the Prediction of Acute Coronary Syndrome. JACC: Cardiovascular Imaging. 2013;6(4):448-57.
26. Hoffmann U, Moselewski F, Nieman K, Jang I-K, Ferencik M, Rahman AM, et al. Noninvasive Assessment of Plaque Morphology and Composition in Culprit and Stable Lesions in Acute Coronary Syndrome and Stable Lesions in Stable Angina by Multidetector Computed Tomography. Journal of the American College of Cardiology. 2006;47(8):1655-62.
27. Puchner SB, Liu T, Mayrhofer T, Truong QA, Lee H, Fleg JL, et al. High-Risk Plaque Detected on Coronary CT Angiography Predicts Acute Coronary Syndromes Independent of Significant Stenosis in Acute Chest Pain. Journal of the American College of Cardiology. 2014;64(7):684-92.
28. Motoyama S, Sarai M, Harigaya H, Anno H, Inoue K, Hara T, et al. Computed Tomographic Angiography Characteristics of Atherosclerotic Plaques Subsequently Resulting in Acute Coronary Syndrome. Journal of the American College of Cardiology. 2009;54(1):49-57.
29. Han D, Kolli KK, Al'Aref SJ, Baskaran L, van Rosendael AR, Gransar H, et al. Machine Learning Framework to Identify Individuals at Risk of Rapid Progression of Coronary Atherosclerosis: From the PARADIGM Registry. J Am Heart Assoc. 2020;9(5):e013958.
30. Nerlekar N, Ha FJ, Cheshire C, Rashid H, Cameron JD, Wong DT, et al. Computed Tomographic Coronary Angiography–Derived Plaque Characteristics Predict Major Adverse Cardiovascular Events. Circulation: Cardiovascular Imaging. 2018;11(1):e006973.
31. Nicholls SJ, Hsu A, Wolski K, Hu B, Bayturan O, Lavoie A, et al. Intravascular ultrasound-derived measures of coronary atherosclerotic plaque burden and clinical outcome. J Am Coll Cardiol. 2010;55(21):2399-407.
32. Lee SE, Sung JM, Andreini D, Al-Mallah MH, Budoff MJ, Cademartiri F, et al. Per-lesion versus per-patient analysis of coronary artery disease in predicting the development of obstructive lesions: the Progression of AtheRosclerotic PlAque DetermIned by Computed TmoGraphic Angiography Imaging (PARADIGM) study. Int J Cardiovasc Imaging. 2020;36(12):2357-64.
33. You S, Sun JS, Park SY, Baek Y, Kang DK. Relationship between indexed epicardial fat volume and coronary plaque volume assessed by cardiac multidetector CT. Medicine (Baltimore). 2016;95(27):8.
34. Motoyama S, Ito H, Sarai M, Kondo T, Kawai H, Nagahara Y, et al. Plaque Characterization by Coronary Computed Tomography Angiography and the Likelihood of Acute Coronary Events in Mid-Term Follow-Up. J Am Coll Cardiol. 2015;66(4):337-46.
35. van Rosendael AR, Lin FY, van den Hoogen IJ, Ma X, Gianni U, Al Hussein Alawamlh O, et al. Progression of whole-heart Atherosclerosis by coronary CT and major adverse cardiovascular events. J Cardiovasc Comput Tomogr. 2021.

36. Gu H, Lu B, Gao Y, Hou Z, Yang S, Yuan X, et al. Prognostic Value of Atherosclerosis Progression for Prediction of Cardiovascular Events in Patients with Nonobstructive Coronary Artery Disease. Acad Radiol. 2020.
37. Zeb I, Li D, Nasir K, Malpeso J, Batool A, Flores F, et al. Effect of statin treatment on coronary plaque progression - a serial coronary CT angiography study. Atherosclerosis. 2013;231(2):198-204.
38. Li Z, Hou Z, Yin W, Liu K, Gao Y, Xu H, et al. Effects of statin therapy on progression of mild noncalcified coronary plaque assessed by serial coronary computed tomography angiography: A multicenter prospective study. Am Heart J. 2016;180:29-38.
39. Symons R, Morris JZ, Wu CO, Pourmorteza A, Ahlman MA, Lima JA, et al. Coronary CT Angiography: Variability of CT Scanners and Readers in Measurement of Plaque Volume. Radiology. 2016;281(3):737-48.
40. Taron J, Lee S, Aluru J, Hoffmann U, Lu MT. A review of serial coronary computed tomography angiography (CTA) to assess plaque progression and therapeutic effect of anti-atherosclerotic drugs. Int J Cardiovasc Imaging. 2020.
41. Halliburton SS, Abbara S, Chen MY, Gentry R, Mahesh M, Raff GL, et al. SCCT guidelines on radiation dose and dose-optimization strategies in cardiovascular CT. Journal of Cardiovascular Computed Tomography. 2011;5(4):198-224.
42. Cao Q, Broersen A, Kitslaar PH, Yuan M, Lelieveldt BPF, Dijkstra J. Automatic coronary artery plaque thickness comparison between baseline and follow-up CCTA images. Med Phys. 2020;47(3):1083-93.
43. Dahal S, Budoff MJ. Implications of serial coronary computed tomography angiography in the evaluation of coronary plaque progression. Current Opinion in Lipidology. 2019;30(6):446-51.
44. Lakshmanan S, Rezvanizadeh V, Budoff MJ. Comprehensive plaque assessment with serial coronary CT angiography: translation to bedside. Int J Cardiovasc Imaging. 2020.

3 Automatic Quantification of Local Plaque Thickness Differences as Assessed by Serial Coronary Computed Tomography Angiography Using Scan-Quality-Based Vessel-Specific Thresholds

Finn Y. van Driest
Alexander Broersen
Rob J. van der Geest
J. Wouter. Jukema
Arthur J. H. A. Scholte
Jouke Dijkstra

Abstract

Introduction: The use of serial coronary computed tomography angiography (CCTA) allows for the early assessment of coronary plaque progression, a crucial factor in averting major adverse cardiac events (MACE). Traditionally, serial CCTA is assessed using anatomical landmarks to match baseline and follow-up scans. Recently, a tool has been developed by Cao et al. that allows for the automatic quantification of local plaque thickness differences in serial CCTA utilizing plaque contour delineation.

The aim of this study was to determine thresholds of plaque thickness differences that define whether there is plaque progression and/or regression. These thresholds depend on the contrast-to-noise ratio (CNR).

Methods: Plaque thickness differences between two scans acquired at the same moment in time should always be zero. The negative and positive differences in plaque contour delineation in these scans were used along with the CNR in order to create calibration graphs on which a linear regression analysis was performed. This analysis was conducted on a cohort of 50 patients referred for a CCTA due to chest complaints. A total of 300 coronary vessels were analyzed. First, plaque contours were semi-automatically determined for all major epicardial coronary vessels. Second, manual drawings of seven regions of interest (ROI) per scan were used to quantify the scan quality based on the CNR for each vessel.

Results: A linear regression analysis was performed on the CNR and negative and positive plaque contour delineation differences. Accounting for the standard error of the estimate, the linear regression analysis revealed that above 1.009-0.002*CNR there is an increase in plaque thickness (progression) and below -1.638+0.012*CNR there is a decrease in plaque thickness (regression).

Conclusion: This study demonstrates the feasibility of developing vessel-specific, quality-based thresholds for visualizing local plaque thickness differences evaluated by serial CCTA. These thresholds have the potential to facilitate the early detection of atherosclerosis progression.

1. Introduction

Coronary artery disease (CAD) is still the leading cause of mortality worldwide [1]. Early detection of CAD is imperative and holds the potential to prevent major adverse cardiac events (MACEs) [2]. There are many techniques for diagnosing CAD, one of which is coronary computed tomography angiography (CCTA). This non-invasive imaging modality allows for both quantitative and qualitative assessments of coronary plaque. The use of serial CCTA, in which baseline and follow-up CCTA scans are compared, allows for the assessment of coronary plaque progression and/or regression [3]. The feasibility of using serial CCTA as a tool for assessing plaque changes has been demonstrated by several studies [4–6]. However, the coregistration of coronary vessels and the subsequent assessment of plaque changes between baseline and follow-up scans are still conducted manually using anatomical landmarks, as depicted in Fig. 1.

In the context of serial CCTA analysis, it is crucial that the assessment is done from a similar longitudinal viewing angle. Afterwards, coronary plaque differences are calculated based on the two-dimensional (2D) transversal view, and experts visually assess and grade the changes. However, the manual selection of viewing angles and landmarks for alignment is time consuming and potentially introduces bias [7]. Moreover, determining whether the difference in the amount of plaque thickness at a certain angle is caused by genuine changes or by a different viewing angle in the multiplanar reconstructions poses a challenge. Recently, Cao et al. developed a novel method for the automatic alignment of baseline and follow-up scans. This method enables direct visualization of plaque changes by calculating plaque thickness differences between baseline and follow-up scans from automatically delineated lumen and vessel wall contours. This tool was validated on artificial datasets. Thresholds of 0.5 mm for plaque progression and - 0.5 mm for plaque regression were found to differentiate between minor deviations and actual plaque changes [7].

The accuracy of the automatic delineation of coronary vessel and lumen contours is dependent on the scan quality, which, in turn, depends on several factors such as the image noise, movement artefacts, and numerous scan parameters [8]. Consequently, thresholds are necessary to differentiate actual changes in plaque thickness from changes caused by inaccuracies in vessel and lumen wall delineation. The scan quality on CCTA can be quantified using the contrast-to-noise ratio (CNR), as this can be indicative of the quality (i.e., detectability) of the contrast in the vessel of interest [9, 10]. This study aimed to use the CNR to develop vessel specific thresholds which can be used in combination with the aforementioned tool for plaque assessment on serial CCTA.

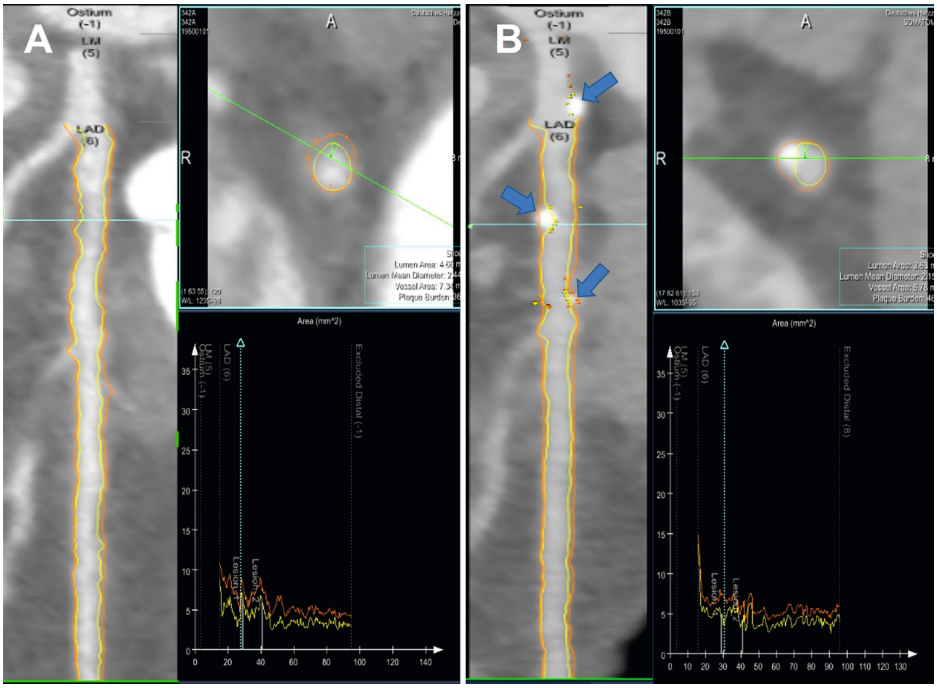

Fig. 1 Example, adapted from Weber et al. [5], of a patient who has undergone serial coronary computed tomography angiography (CCTA); the baseline scan is shown in panel A and the follow-up scan is shown in panel B. Plaque delineation is marked by the orange and yellow lines representing the vessel and lumen, respectively. A total of three newly formed calcified plaques are seen in the follow-up scan, as marked by the blue arrows. In this case, the branching of the circumflex (*Cx*) artery may be used as an anatomical landmark for co-registration by visual analysis. *LAD* left anterior descending artery, *LM* left main artery, *mm* millimeters

2. Materials and Methods

2.1 Patients

Fifty randomly selected patients from the Leiden University Medical Center, the Netherlands, who had chest pain complaints and were referred for a CCTA were included in the current study. Two different phase reconstructions from the same scan from each patient were chosen; the two reconstructions were in the range of either 70–80% or 30–80% for the entire cohort. In principle, this meant that plaque thickness differences should have been absent, as both phases were made almost simultaneously. The compared reconstructed phases were always within the same RR interval, which constitutes the time between two successive R waves of the QRS signal on the electrocardiogram (ECG). The compared phase pairs were always within the same gated window; either 70–80% or 30–80%, and always constituted a 75% phase and a randomly reconstructed other phase. All data were clinically acquired and retrospectively analyzed. The institutional review board of the Leiden University Medical Center, the Netherlands,

approved this retrospective evaluation of clinically collected data and waived the need for written informed consent. This study was performed in accordance with the Helsinki Declaration of 1964 and its later amendments.

2.2 Data acquisition

CCTA was performed using a 320-row volumetric scanner (Aquilion ONE and Aquilion ONE Genesis Edition, Canon Medical Systems, Otawara, Japan). Heart rate and blood pressure were monitored 1 h before CCTA. Metoprolol (from 25 mg up to 150 mg) was administered orally to patients exceeding a heart rate of 60 beats per minute (bpm) provided that no contraindications were present. Additional metoprolol was injected intravenously if the heart rate remained above 60 bpm. Nitroglycerin (0.4 mg) was administered sublingually 4 min prior to CCTA. The scan parameters were as follows: a detector collimation of 320 x 0.5 mm, a 275-ms gantry rotation time, and a temporal resolution of 137 ms for the Aquilion ONE Genesis Edition; a detector collimation of 320 x 0.5 mm, a 350-ms gantry rotation time, and a temporal resolution of 175 ms for the Aquilion ONE. The peak tube voltage was 100–135 kV with a tube current of 140–580 mA for both scanners. 70–80% of the RR interval was scanned using prospective ECG triggering. When the heart rate was above 65 bpm, 30–80% of the RR interval was scanned. The first 50–90 ml of contrast agent (Iomeron 400, Bracco, Milan, Italy) was administered in the antecubital vein. Thereafter, 20 ml of a 1:1 mixture of contrast and saline and finally 25 ml of saline were administered. CCTA was performed at the next beat when the threshold of 300 Hounsfield units (HU) was reached in the descending aorta. The protocol settings were the same for the Aquilion ONE and Aquilion ONE Genesis Edition; a tube voltage of 100 kV was generally used. A 120-kV tube voltage was used for patients who had a weight exceeding 130 kg and/or were bearing an implantable cardioverter-defibrillator (ICD). Tube current ranged between 300 and 900 mA depending on patient size. Field of view (FOV) was also dependent on patient size and ranged between 200 and 280 mm. Image reconstruction was done using iterative reconstruction by means of adaptive iterative dose reduction-3D (AIDR-3D) enhanced for the Aquilion ONE Genesis Edition and AIDR-3D for the Aquilion ONE using the FC03 reconstruction kernel for both scanners. Iterative reconstruction strength was set at mild, standard, or strong depending on the image noise. Image size was set at 512 x 512. The slice thickness of the reconstruction was 0.25 mm for all but two of the reconstructed phases, which had a slice thickness of 1.0 mm.

It is important to note that the protocol and image reconstruction settings remained consistent for all compared reconstructed phases.

2.3 Data processing

Dicom images were transferred to an offline workstation for analysis. Dedicated software (QAngio CT Research Edition v3.1.5.1, Medis Medical Imaging, Leiden, the Netherlands) was employed to conduct automatic tracing of the coronary arteries and the semi-automatic detection of the lumen and vessel wall contours. The contours were

corrected manually if needed, whilst the reader was blinded to the results of the other phase. Coronary artery tree extraction and vessel selection are depicted in Fig. 2.

A software program developed in house by Cao et al. [7] was employed to extract the threedimensional (3D) lumen and vessel wall surface models of the three main arteries in each of the two scans. The software co-registers both 3D models and encodes the local plaque thickness differences between the two scans on the surface of a model. Subsequently, ParaView (version 5.9.0) was utilized for the 3D visualization of the generated models.

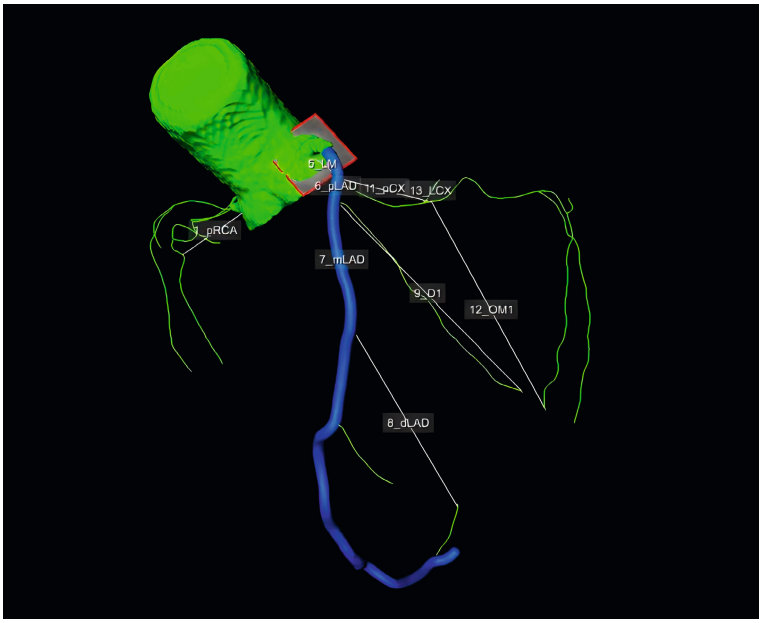

Fig. 2 The complete coronary tree is extracted from the CCTA. In this example, the left anterior descending artery (*LAD*) is marked in blue for performing plaque delineation. *LM* left main artery, *pLAD* proximal left anterior descending artery, *dLAD* distal left anterior descending artery, *pRCA* proximal right coronary artery, *pCX* proximal circumflex artery, *LCX* left circumflex artery, *D1* first diagonal artery, *OM1* first obtuse marginal artery, *mLAD* mid left anterior descending artery, *CCTA* coronary computed tomography angiography

2.4 Scan quality

In order to quantify image quality, the CNR was calculated separately for the left anterior descending artery (LAD), the right coronary artery (RCA), and the circumflex artery (Cx). We opted to use CNR as a metric to quantify image quality as this has been proven to affect the accuracy of CCTA. Furthermore, it has been demonstrated that a reduced CNR results in a reduced sharpness of vessel visualization. The latter negatively influences plaque visualization and thus also software-aided plaque delineation [11, 12]. Contrary to the signal-to-noise ratio (SNR), CNR serves as a quantitative metric for low-contrast

lesion detection: the higher the CNR between lesion and background, the more likely the detection of the lesion [13]. Although the SNR and CNR formulas are similar, SNR lacks specificity, as it does not consider the mean intensity of the surrounding epicardial tissue [14]. Therefore, CNR presents superior significance in contrast-enhanced scans like CCTA, as it is a measure of image quality based on a contrast [15]. A total of seven regions of interest (ROIs) per patient were defined for the measurement of the intensity values and the subsequent calculation of the CNR. The first ROI was placed in the ascending aorta, superior and in close proximity to the origin of the RCA, to define image noise. Thereafter, three ROIs were placed in the most proximal part of each coronary vessel. The final three ROIs were placed in the epicardial tissue surrounding each vessel, adhering to the same slice position and in spatial proximity to the ROI in the corresponding vessel. ROI placement was performed meticulously to exclude calcifications, plaques, vessel walls, and any potential image artifacts. Figure 3 depicts an example of a patient with ROIs placed in the aorta, LAD, and surrounding epicardial tissue.

The CNR was subsequently calculated for each vessel using the following formula:

$$CNR = \frac{\mu_{vessel} - \mu_{epicardial\ tissue}}{\sigma_{aorta}}$$

In which: μ_{vessel} represents the mean HU intensity of the specific coronary vessel, $\mu_{epicardial\ tissue}$ represents the mean HU intensity of the epicardial tissue in spatial proximity to the specific coronary vessel and σ_{aorta} represents the standard deviation of the HU intensity in the ascending aorta.

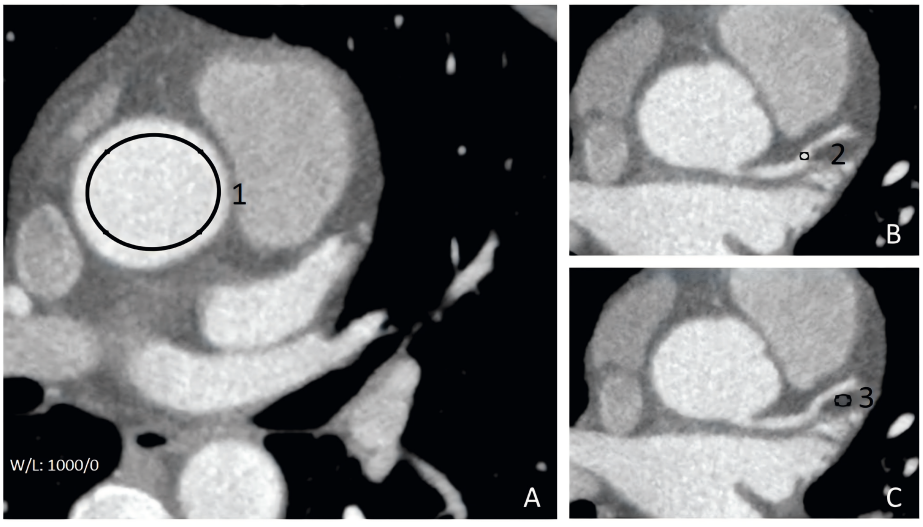

Fig. 3 Regions of interest are manually drawn in the aorta (A), proximal LAD (B), and the corresponding epicardial tissue surrounding the LAD (C). This means of operation is the same for the Cx and the RCA. *LAD* left anterior descending artery, *Cx* circumflex artery, *RCA* right coronary artery

2.5 Negative and positive thresholds

Coronary lumen and vessel wall contours are detected in the multi-planar reformatted images of the artery. Based on the detected lumen and vessel wall contours, the plaque thickness at a certain location in an artery can be calculated. This is done by calculating the distance between the points at which the lumen contour and the vessel contour intersect with the line through the lumen center. The change in plaque thickness is determined as the difference in plaque thickness at the corresponding location between scans [7]. It is important to note that the accuracy of contours and thus plaque delineation is dependent on the scan quality [16]. Therefore, thresholds are needed to filter out insignificant changes in plaque thickness differences resulting from variations in contour quality. Figure 4 depicts a clinical example of a case with plaque progression in the LAD that shows the importance of using thresholds for plaque thickness change visualization.

In order to establish vessel-specific thresholds, calibration graphs were created between the lowest measured CNR of a vessel in both phases and the largest negative and largest positive differences in plaque thickness measurements between two-phase scans. For each patient, two different reconstructed phases from the same scan were compared. As plaque differences between two reconstructed phases from the same scan and from the same patient should always be zero, it is possible to compare both phases in a two-way manner. Hence, for each patient, two values of the plaque thickness difference were obtained, yielding a total of 100 values. Subsequently, any plaque thickness delineation differences between two-phase scan sets had to be attributable to different factors such as scan quality. The software tool from Cao et al. [7] was utilized for automatically calculating the negative and positive plaque thickness differences. Subsequently, the largest negative and largest positive thickness differences were plotted against the vessel-specific CNR. Linear regression facilitates the determination of the linear relationship between a dependent and independent variable, in this case plaque thickness difference and CNR, respectively. Formulas were derived through linear regression analysis conducted on the aforementioned charts using SPSS software (version 25, SPSS IBM Corp., Armonk, New York). The standard error of the estimate which is used in linear regression analysis was multiplied by a value of one instead of the customary two. This was done pragmatically in order to ensure that the model was capable of detecting relatively small plaque changes with regard to the average coronary lumen diameter, which is between 3 and 4 mm [17]. A detailed step-by-step flowchart depicting the aforementioned process is presented in Fig. 5.

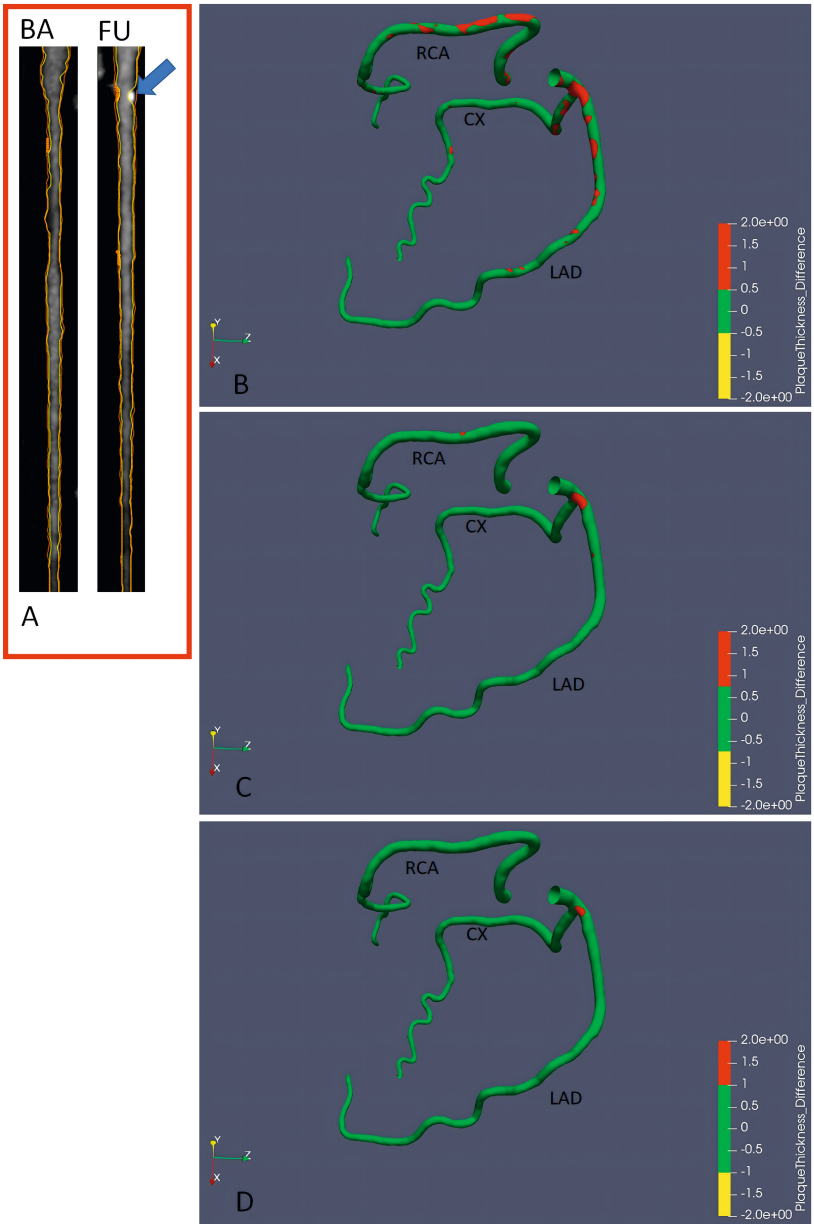

Fig. 4 A newly formed plaque is observed in the proximal LAD, as marked by the blue arrow (A). No other vessels have plaque (changes). Multiple areas are identified as having plaque progression using cutoff values of - 0.5 and 0.5 (B). Larger cutoff values of - 0.75 and 0.75 still do not allow plaque progression to be discerned in the RCA and the middle part of the LAD, as marked by the red areas (C). Finally, cutoff values of - 1.0 and 1.0 seem to correlate well with the visual observations in panel A (D). This demonstrates the importance of using cutoff values, yet the adaptive values must still be calculated using the CNR as a marker of scan quality. Plaque thickness differences are given in mm. *BA* baseline, *FU* follow-up, *RCA* right coronary artery, *LAD* left anterior descending artery, *Cx* circumflex artery, *CNR* contrast-to-noise ratio

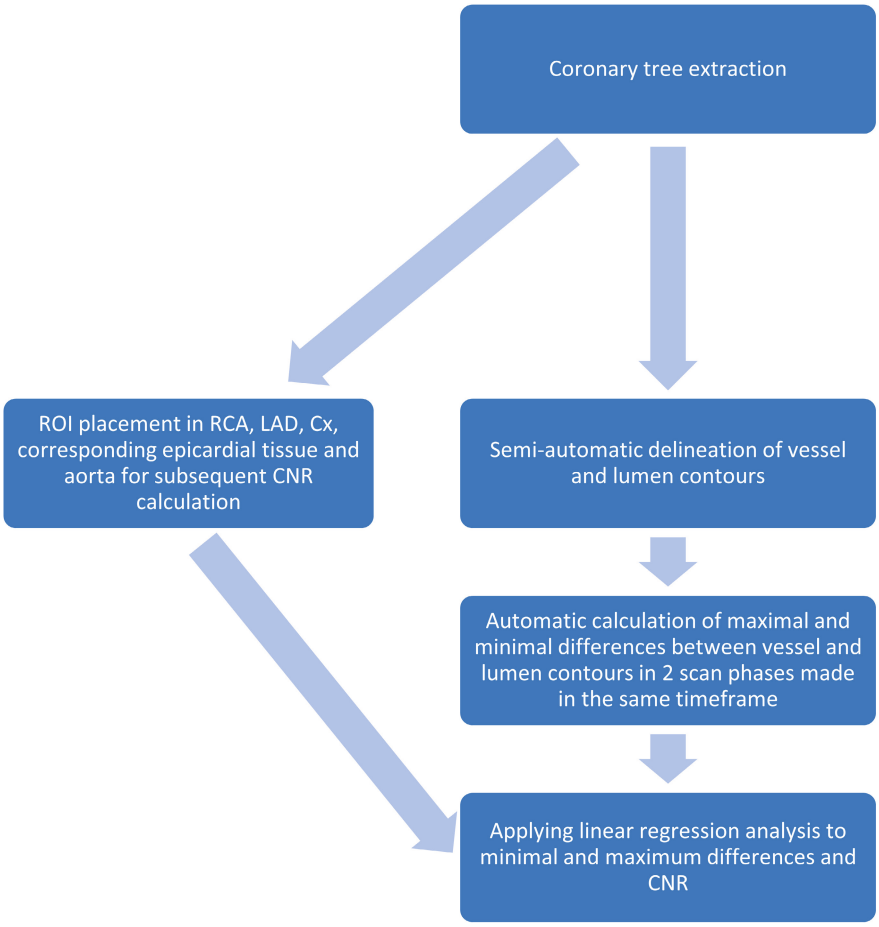

Fig. 5 Flowchart depicting the process of creating formulas for thresholds of plaque differences using scan quality. *ROI* region of interest, *CNR* contrast-to-noise ratio, *RCA* right coronary artery, *LAD* left anterior descending artery, *Cx* circumflex artery

2.6 Inter-observer measurements

A random set of 15 scans were utilized for interobserver measurements, resulting in the analysis of 45 coronary vessels. Observer AB (with 13 years of experience in cardiovascular image analysis) also drew a total of seven ROIs per patient for CNR measurements. Thereafter, the calculated CNR values were compared to those obtained by observer FY (with 3 years of experience in cardiovascular image analysis). Subsequently, correlations were tested using Pearson's correlation coefficient.

3. Results

A total of 300 coronary vessels were used for the current analysis. The average CNR value was 13.4 ± 3.6. The average positive and negative differences in measured plaque thickness were 0.7 ± 0.3 and - 0.9 ± 0.6 mm, respectively. A more detailed description of the values per vessel is depicted in Table 1.

Table 1 Detailed description of the values found per vessel. All values are the mean ± standard deviation. *CNR* contrast-to-noise-ratio, *LAD* left anterior descending artery, *RCA* right coronary artery, *Cx* circumflex artery, *Mm* millimeters

	Mean CNR	Mean positive difference	Mean negative difference
LAD	13.3±3.6	0.6±0.4mm	-0.8±0.6mm
RCA	13.7±3.6	0.7±0.4mm	-1.0±0.6mm
CX	13.3±3.5	0.5±0.2mm	-0.8±0.6mm

A trend was observed for the relationship between the higher and lower CNR values and the subsequent positive and negative plaque thickness differences, as depicted in Figs. 6 and 7.

A linear regression analysis was performed for all the positive and negative differences in plaque thickness along with the CNR calculated per vessel. Along with the standard errors of the estimate—which were 0.349 and - 0.61, respectively, for the positive and negative differences—this analysis yielded the following formulas:

$$Positive\ difference = ((0.660 - (0.002 * CNR)) + 0.349$$

$$Negative\ difference = ((- 1.028 + (0.012 * CNR)) - 0.61$$

Positive and negative plaque thickness differences are expressed in mm.

The inter-observer correlation for CNR values was excellent, with a correlation coefficient of 0.872 ($p < 0.001$). Figure 8 demonstrates the correlation between CNR measurements done by observers FY and AB.

The application of the aforementioned formulas along with the corresponding thresholds is shown in the two examples depicted in Figs. 9 and 10. It is important to emphasize that a distinct threshold was applied for each vessel, which was determined from the lowest CNR observed in that vessel across both the baseline and the follow-up scans.

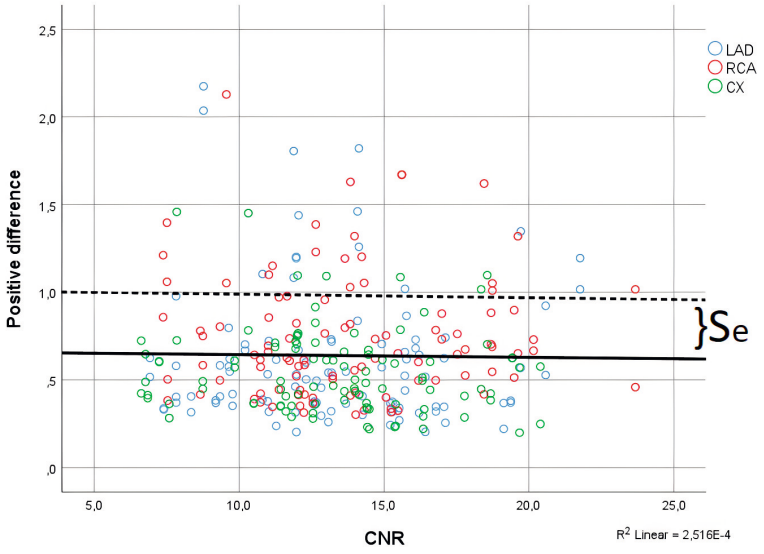

Fig. 6 Positive differences in plaque thickness are plotted against the respective CNR of the specific vessel. The dotted line represents the relationship between CNR and positive difference including the standard error of the estimate. A trend is observed in which higher CNR values (related to higher scan quality) and lower CNR values (related to lower scan quality) correspond to lower and higher positive differences in plaque thickness, respectively. Positive differences are given in mm. *Se* standard error of the estimate, *LAD* left anterior descending artery, *RCA* right coronary artery, *Cx* circumflex artery, *CNR* contrast-to-noise ratio

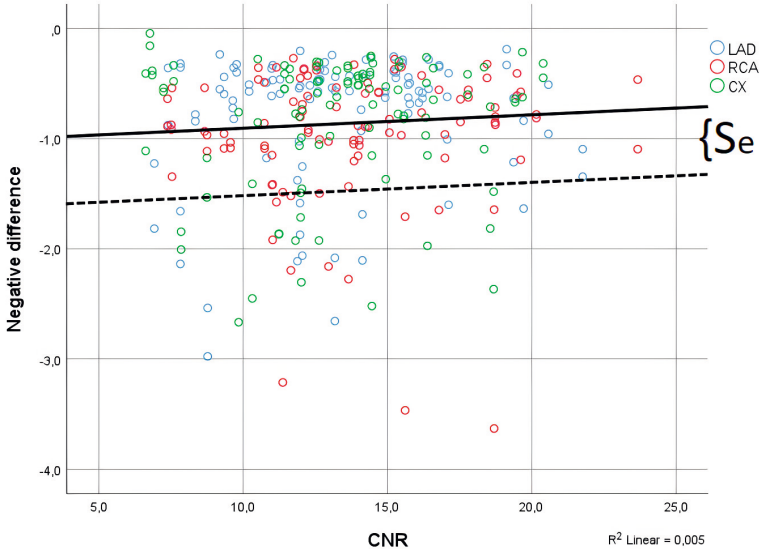

Fig. 7 Negative differences in plaque thickness are plotted against the respective CNR of the specific vessel. The dotted line represents the relationship between CNR and negative difference including the standard error of the estimate. A trend is observed in which higher CNR values (related to higher scan quality) and lower CNR values (related to lower scan quality) correspond to higher and lower negative differences in plaque thickness, respectively. Negative differences are given in mm. *Se* standard error of the estimate, *LAD* left anterior descending artery, *RCA* right coronary artery, *Cx* circumflex artery, *CNR* contrast-to-noise ratio

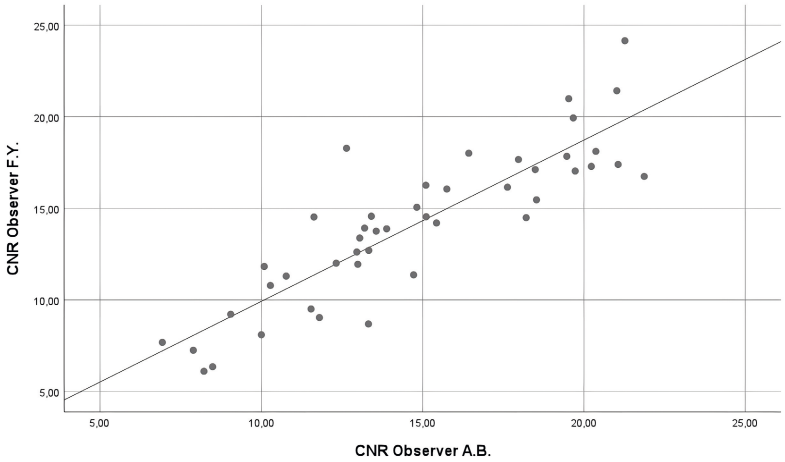

Fig. 8 Correlation between CNR measurements done by observers FY and AB. CNR contrast-to-noise ratio

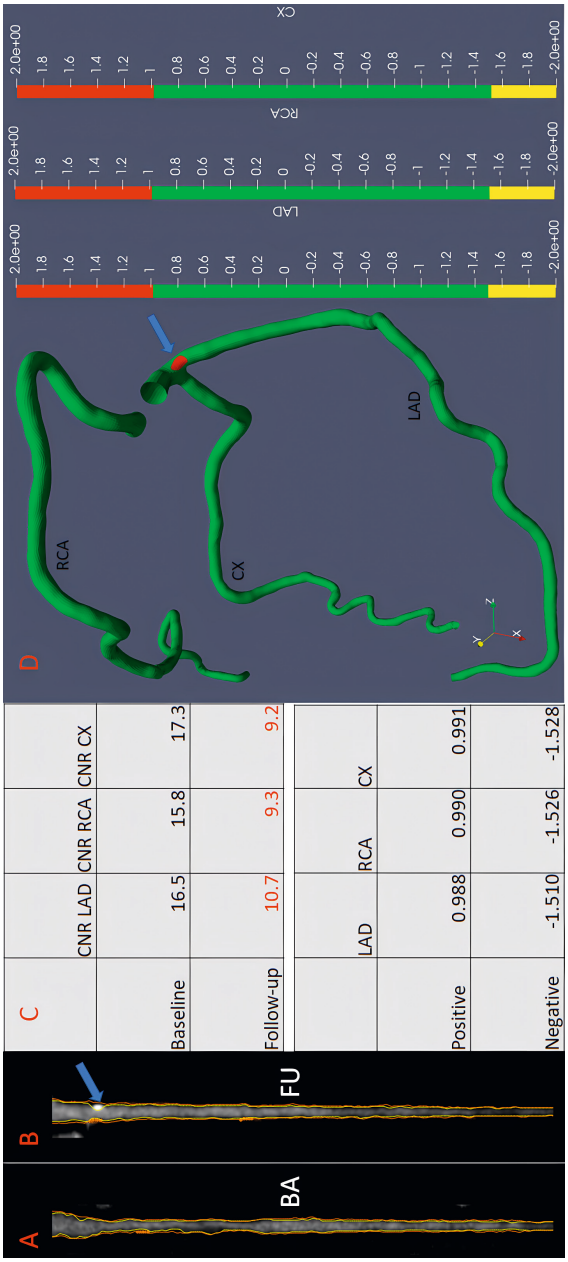

Fig. 9 Patient with a newly formed calcified plaque only in the proximal LAD after 7 years follow-up, as marked by the blue arrow (A and B). The CNR was calculated separately for the LAD, RCA, and Cx. CNR values of 10.7, 9.3, and 9.2 were found for those vessels, respectively (C). Using the aforementioned CNR values, thresholds (positive and negative) were calculated for each vessel separately. Subsequent visualization of the coronary tree with those thresholds clearly demonstrates the plaque change in the proximal LAD, as marked by the red area and blue arrow (D). Plaque thickness differences are given in mm. *BA* baseline, *FU* follow-up, *RCA* right coronary artery, *LAD* left anterior descending artery, *Cx* circumflex artery, *CNR* contrast-to-noise ratio

Fig. 10 Patient with newly formed plaques in the LAD, Cx, and RCA, as marked by the blue arrows, after 6 years of follow-up (A). The CNR was calculated separately for the LAD, RCA, and Cx. CNR values of 9.0, 12.8, and 13.6 were found for those vessels, respectively (B). Using the aforementioned CNR values, thresholds (positive and negative) were calculated for each vessel separately. Subsequent visualization of the coronary tree with those thresholds clearly demonstrates the plaque changes in the LAD, Cx, and RCA, as marked by the red areas and blue arrows (C). Note that the newly formed plaque in the proximal RCA is not visualized as it is on the opposite side of the vessel. This is also the case with the Cx: a major part of the newly formed plaque is on the opposite side of the vessel. Plaque thickness differences are given in mm. *BA* baseline, *FU* follow-up, *RCA* right coronary artery, *LAD* left anterior descending artery, *Cx* circumflex artery, *CNR* contrast-to-noise ratio

4. Discussion

In this study, we have proposed a method for the objective assessment of plaque dynamics using patient-specific thresholds on CCTA. These thresholds were obtained by using calibration graphs with two-phase scan sets in which negative and positive plaque thickness differences were plotted against the subsequent scan quality calculated as the CNR. The results demonstrate that the use of these vessel-specific thresholds allows for the direct visualization and quantification of plaque thickness differences, and they show good visual agreement with the plaque localization. It is important to stress that although there is no gold standard for plaque change validation in the current study, an artificial validation of the proposed method was done by Cao et al. Their study demonstrated excellent correspondence between calculated plaque differences and artificially created plaque changes in coronary arteries [7].

Calibration graphs and a subsequently performed linear regression yielded a very slight trend regarding the CNR and negative and positive plaque thickness differences. Further analysis of these formulas reveals that changes in CNR only mildly affect the subsequent threshold. Positive and negative plaque thickness thresholds of 0.982 mm and - 1.472 mm are found, respectively, if we utilize the average CNR value of 13.4. Previous studies by Fayad et al. indicate that the average vessel wall thickness ranges from 0.75 ± 0.17 mm for healthy segments to an average thickness range of 4.38 ± 0.71 mm for large plaques causing stenosis of C 40% [18]. The positive and negative plaque thickness thresholds found in our study using the average CNR would be clinically applicable as they fall in between the range of values for healthy and atherosclerotic segments found by Fayad et al. The inter-observer correlation for CNR values was excellent. Hence, differences in ROI placement caused by inter-observer variability will only have a very minor impact on the final formulas. Furthermore, Papadopoulou et al. demonstrated that inter-observer agreement for the detection of atherosclerotic segments using plaque delineation was strong (Cohen's kappa coefficient K = 1.0) [19]. This is especially important, as the detection of serial plaque changes is dependent on the plaque delineation in subsequent baseline and follow-up scans.

A great advantage of the proposed method for the assessment of serial plaque changes, as opposed to the current method based on the calculation of the plaque's volume, is that changes can be visualized locally. Furthermore, our method of visualizing plaque differences is not affected by the size of the vessel, which is an advantage compared to the current method [20–22]. Visualizing the location(s) of plaque changes in the subsequent coronary vessel(s) may be especially beneficial for patients undergoing coronary catheterization as this can guide clinicians to the location(s) of interest.

4.1 Limitations

This study has several limitations which are innate to its novel nature and retrospective design. A major limitation is the absence of a gold standard for the assessment of plaque changes aside from visual assessment. For the analyzed patient population, no intravascular imaging like intravascular ultrasound (IVUS) was available to serve as a high-resolution ground truth. As thresholds are used in the output 3D model, there is a possibility of "missing" plaque changes that are below the threshold, and unfortunately there is no method to objectify this possibility. Contrastingly, there is also a chance of "exaggerating" plaque changes if the lumen or vessel wall is incorrectly delineated. The use of one times the standard error instead of the more conventionally used two times its value will statistically also lead to more false-positive plaque changes, as the confidence interval is then set at around 68%, in contrast to the "regular" 95%. On the other hand, having relatively low negative and high positive thresholds as compared to the average coronary lumen size would lead to more false negatives [17]. Ultimately, we used one standard error from a pragmatic perspective, as this would ensure the detection of relatively small plaque changes. Furthermore, despite not having a gold standard for plaque change validation, plaque changes that are potentially wrongfully detected may be dismissed, as visual assessment remains a form of ground truth. The CNR was calculated at the proximal part of the vessel. However, CNR values can change upon moving more distally in the subsequent vessel, as was demonstrated by Yokota at el. Fortunately, the differences between proximal and distal locations were found to be small [23]. Yet, the possibility that plaque thickness delineation is affected by the location in the vessel cannot be excluded. Also, the CNR itself is very sensitive to the background location in the epicardium, which leads to biased inter-observer measurements. The correlation coefficient found for inter-observer correlations regarding CNR measurements was very strong. The vast majority of the reconstructed phases had a slice thickness of 0.25 mm, yet two phases were reconstructed using a 1.0-mm slice thickness. A study by Alshipli and Kabir has demonstrated that the effect of slice thickness on image noise is extremely minor [24]. Furthermore, it is worth noting that 98% of our cohort utilized a 0.25-mm slice thickness; they greatly outnumber the 2% that was reconstructed based on a 1.0-mm slice thickness. Hence, a potential bias caused by these slice thickness differences would be highly unlikely.

Finally, it must be noted that although the demonstrated method may visualize plaque differences locally, it is often more effective to determine the total plaque burden with regard to the management of patients with CAD. This is due to the fact that atherosclerosis is a dynamic process that changes constantly. Hence, placing emphasis on the entire atherosclerosis process and global imaging of the heart represent a better approach than focusing on a single plaque [25]. Also, a recent development has been the use of positron emission tomography (PET) using 18F-NaF, which has the ability to detect the active microcalcification that is believed to represent unstable plaques. This is contrary to

computed tomography (CT) scans, which detect macrocalcifications, as these represent stable areas where the atherosclerotic disease is quiescent [26].

As the goal of this study was to develop vessel-specific thresholds for the direct visualization of plaque thickness differences, more testing and further investigation are needed.

5. Conclusion

The development of patient-specific plaque thickness thresholds seems feasible and allows for the direct visualization of plaque thickness differences in serial CTA, as demonstrated by these preliminary results. However, currently this study must be interpreted as a proof of concept for determining and using threshold values for clinical data. In the future this methodology may be used for the assessment of plaque changes on serial clinical CCTA scans, preferably combined with serial IVUS acquisition or a thorough cardiac phantom study.

References

1. World Health O. The atlas of heart disease and stroke / Judith Mackay and George Mensah ; with Shanthi Mendis and Kurt Greenland. Geneva: World Health Organization; 2004.
2. Bom MJ, van der Heijden DJ, Kedhi E, van der Heyden J, Meuwissen M, Knaapen P, et al. Early Detection and Treatment of the Vulnerable Coronary Plaque: Can We Prevent Acute Coronary Syndromes? Circ Cardiovasc Imaging. 2017;10(5).
3. Hoffmann U, Moselewski F, Nieman K, Jang IK, Ferencik M, Rahman AM, et al. Noninvasive assessment of plaque morphology and composition in culprit and stable lesions in acute coronary syndrome and stable lesions in stable angina by multidetector computed tomography. J Am Coll Cardiol. 2006;47(8):1655-62.
4. Yu M, Li W, Lu Z, Wei M, Yan J, Zhang J. Quantitative baseline CT plaque characterization of unrevascularized non-culprit intermediate coronary stenosis predicts lesion volume progression and long-term prognosis: A serial CT follow-up study. Int J Cardiol. 2018;264:181-6.
5. Weber C, Deseive S, Brim G, Stocker TJ, Broersen A, Kitslaar P, et al. Coronary plaque volume and predictors for fast plaque progression assessed by serial coronary CT angiography-A single-center observational study. Eur J Radiol. 2020;123:108805.
6. Lee SE, Sung JM, Andreini D, Al-Mallah MH, Budoff MJ, Cademartiri F, et al. Differences in Progression to Obstructive Lesions per High-Risk Plaque Features and Plaque Volumes With CCTA. JACC Cardiovasc Imaging. 2020;13(6):1409-17.
7. Cao Q, Broersen A, Kitslaar PH, Yuan M, Lelieveldt BPF, Dijkstra J. Automatic coronary artery plaque thickness comparison between baseline and follow-up CCTA images. Med Phys. 2020;47(3):1083-93.
8. Ghekiere O, Salgado R, Buls N, Leiner T, Mancini I, Vanhoenacker P, et al. Image quality in coronary CT angiography: challenges and technical solutions. Br J Radiol. 2017;90(1072):20160567.
9. Welvaert M, Rosseel Y. On the definition of signal-to-noise ratio and contrast-to-noise ratio for FMRI data. PLoS One. 2013;8(11):e77089.
10. Konstantinidis A. 2.02 - Physical Parameters of Image Quality. In: Brahme A, editor. Comprehensive Biomedical Physics. Oxford: Elsevier; 2014. p. 49-63.
11. Hubbard L, Malkasian S, Zhao Y, Abbona P, Molloi S. Contrast-to-Noise Ratio Optimization in Coronary Computed Tomography Angiography: Validation in a Swine Model. Acad Radiol. 2019;26(6):e115-e25.
12. Cademartiri F, Mollet NR, Lemos PA, Saia F, Midiri M, de Feyter PJ, et al. Higher intracoronary attenuation improves diagnostic accuracy in MDCT coronary angiography. AJR Am J Roentgenol. 2006;187(4):W430-3.
13. Signal, Noise, Signal-to-Noise, and Contrast-to-Noise Ratios. In: Hendrick RE, editor. Breast MRI: Fundamentals and Technical Aspects. New York, NY: Springer New York; 2008. p. 93-111.
14. Feger S, Rief M, Zimmermann E, Martus P, Schuijf JD, Blobel J, et al. The Impact of Different Levels of Adaptive Iterative Dose Reduction 3D on Image Quality of 320-Row Coronary CT Angiography: A Clinical Trial. PLoS One. 2015;10(5):e0125943.
15. Alsleem HA, Almohiy HM. The Feasibility of Contrast-to-Noise Ratio on Measurements to Evaluate CT Image Quality in Terms of Low-Contrast Detailed Detectability. Med Sci (Basel). 2020;8(3).
16. Ghanem AM, Hamimi AH, Matta JR, Carass A, Elgarf RM, Gharib AM, et al. Automatic Coronary Wall and Atherosclerotic Plaque Segmentation from 3D Coronary CT Angiography. Sci Rep. 2019;9(1):47.
17. Dodge JT, Jr., Brown BG, Bolson EL, Dodge HT. Lumen diameter of normal human coronary arteries. Influence of age, sex, anatomic variation, and left ventricular hypertrophy or dilation. Circulation. 1992;86(1):232-46.
18. Fayad ZA, Fuster V, Fallon JT, Jayasundera T, Worthley SG, Helft G, et al. Noninvasive in vivo human coronary artery lumen and wall imaging using black-blood magnetic resonance imaging. Circulation. 2000;102(5):506-10.
19. Papadopoulou S-L, Neefjes LA, Schaap M, Li H-L, Capuano E, van der Giessen AG, et al. Detection and quantification of coronary atherosclerotic plaque by 64-slice multidetector CT: A systematic head-to-head comparison with intravascular ultrasound. Atherosclerosis. 2011;219(1):163-70.
20. Nakanishi R, Alani A, Matsumoto S, Li D, Fahmy M, Abraham J, et al. Changes in Coronary Plaque Volume: Comparison of Serial Measurements on Intravascular Ultrasound and Coronary Computed Tomographic Angiography. Tex Heart Inst J. 2018;45(2):84-91.
21. Inoue K, Motoyama S, Sarai M, Sato T, Harigaya H, Hara T, et al. Serial Coronary CT Angiography–Verified Changes in Plaque Characteristics

as an End Point: Evaluation of Effect of Statin Intervention. JACC: Cardiovascular Imaging. 2010;3(7):691-8.
22. Foldyna B, Lo J, Mayrhofer T, Grinspoon SK, Hoffmann U, Lu MT. Individual coronary plaque changes on serial CT angiography: Within-patient heterogeneity, natural history, and statin effects in HIV. Journal of Cardiovascular Computed Tomography. 2020;14(2):144-8.
23. Yokota Y, Takeda C, Kidoh M, Oda S, Aoki R, Ito K, et al. Effects of Deep Learning Reconstruction Technique in High-Resolution Non-contrast Magnetic Resonance Coronary Angiography at a 3-Tesla Machine. Canadian Association of Radiologists Journal. 2020;72(1):120-7.
24. Alshipli M, Kabir NA. Effect of slice thickness on image noise and diagnostic content of single-source-dual energy computed tomography. Journal of Physics: Conference Series. 2017;851(1):012005.
25. Høilund-Carlsen PF, Piri R, Gerke O, Edenbrandt L, Alavi A. Assessment of Total-Body Atherosclerosis by PET/Computed Tomography. PET Clinics. 2021;16(1):119-28.
26. Bassir A, Raynor WY, Park PSU, Werner TJ, Alavi A, Revheim M-E. Molecular imaging in atherosclerosis. Clinical and Translational Imaging. 2022;10(3):259-72.

Part 2

Myocardial CT perfusion and quantification

4 Quantification of myocardial ischemia and subtended myocardial mass at adenosine stress cardiac computed tomography. A feasibility study

F. Y. van Driest
R. J. van der Geest
A. Broersen
J. Dijkstra
M. el Mahdiui
J. W. Jukema
A. J. H. A. Scholte

Abstract

Purpose: Combination of coronary computed tomography angiography (CCTA) and adenosine stress CT myocardial perfusion (CTP) allows for coronary artery lesion assessment as well as myocardial ischemia. However, myocardial ischemia on CTP is nowadays assessed semi-quantitatively by visual analysis. The aim of this study was to fully quantify myocardial ischemia and the subtended myocardial mass on CTP.

Methods: We included 33 patients referred for a combined CCTA and adenosine stress CTP protocol, with good or excellent imaging quality on CTP. The coronary artery tree was automatically extracted from the CCTA and the relevant coronary artery lesions with a significant stenosis (≥ 50%) were manually defined using dedicated software. Secondly, epicardial and endocardial contours along with CT perfusion deficits were *semi-automatically* defined in short-axis reformatted images using MASS software. A Voronoi-based segmentation algorithm was used to quantify the subtended myocardial mass, distal from each relevant coronary artery lesion. Perfusion defect and subtended myocardial mass were spatially registered to the CTA. Finally, the subtended myocardial mass per lesion, total subtended myocardial mass and perfusion defect mass (per lesion) were measured.

Results: Voronoi-based segmentation was successful in all cases. We assessed a total of 64 relevant coronary artery lesions. Average values for left ventricular mass, total subtended mass and perfusion defect mass were 118, 69 and 7 g respectively. In 19/33 patients (58%) the total perfusion defect mass could be distributed over the relevant coronary artery lesion(s).

Conclusion: Quantification of myocardial ischemia and subtended myocardial mass seem feasible at adenosine stress CTP and allows to quantitatively correlate coronary artery lesions to corresponding areas of myocardial hypoperfusion at CCTA and adenosine stress CTP.

1. Introduction

In patients with coronary artery disease (CAD) an imaging protocol combining coronary computed tomography angiography (CCTA) and adenosine stress CT myocardial perfusion (CTP) allows for anatomical and functional assessment of coronary artery lesions as well as myocardial ischemia (1) (2). The decision to revascularize patients depends both on the lesion severity and location as well as the extent of the relative hypoperfused (ischemic) myocardium, relative to the subtended myocardial mass distal of the coronary stenosis (1). However, adenosine stress CTP is nowadays assessed semi-quantitatively by visual analysis on a routine basis in many centres.

The Voronoi algorithm is a mathematical algorithm that enables users to divide a two-dimensional area or three-dimensional space by predetermined points based on the shortest distance to those points. This algorithm can be used to divide tissue supplied by different blood vessels according to which blood vessel is closest to the tissue. By using a Voronoi-based segmentation algorithm on myocardial tissue it seems possible to quantify the subtended myocardial mass for each lesion in the coronary tree (3). By also quantifying the hypoperfused myocardium itself we aim to identify the distribution of myocardial ischemia over the coronary artery lesion(s). To the best of our knowledge this has never been done in a fully quantitative manner for adenosine stress CTP. Therefore, we hypothesize that full quantification of adenosine stress myocardial ischemia and subtended myocardial mass using this Voronoi-based segmentation algorithm is feasible and may ease detection of hemodynamically significant lesions.

2. Materials and methods

2.1 Patients

33 patients with chest pain complaints, referred for a combined CCTA and adenosine stress CTP protocol were included in the current study. As manual drawing of perfusion defects is dependent on scan quality of adenosine stress CTP, only patients with good or excellent imaging quality of these scans were selected from our CTP database containing 241 patients. Patients with normal CTP images or fixed perfusion defects were excluded because reversible ischemia is or may be absent in these cases, respectively (4). Clinically acquired data were retrospectively analysed. The institutional review board of the Leiden University Medical Center, The Netherlands, approved this retrospective evaluation of clinically collected data and waived the need for written informed consent.

2.2 Data acquisition and analysis

CCTA and static adenosine stress CTP were performed using a 320-row volumetric scanner (Aquilion ONE, Canon Medical Systems and Aquilion ONE Genesis Edition, Canon Medical Systems, Otawara, Japan). Consumption of caffeine products 24 h before examination

was discouraged. One hour before CCTA heart rate and blood pressure were monitored. If a patient's heart rate exceeded 60 beats per minutes (bpm) and no contraindications were present metoprolol, 25 mg up until 150 mg, was administrated orally. If the heart rate remained above 60 bpm additional metoprolol was injected intravenously.

Prior to CCTA nitroglycerin (0.4 mg) was administered sublingually. Scan parameters for CCTA were as follows: peak tube voltage 100-135 kV with a tube current of 140-580mA. A detector collimation of 320 x 0.5 mm, a 275 ms gantry rotation time and temporal resolution of 137 ms for the Aquilion ONE Genesis Edition and a detector collimation of 320 x 0.5 mm, 350 ms gantry rotation time and temporal resolution of 175 ms for the Aquilion ONE. Prospectively electrocardiogram (ECG) triggering was used to scan 70% to 80% of the RR interval. When heart rate was above 65 bpm 30% to 80% of the RR-interval was scanned. First 50 to 90 ml of contrast agent (Iomeron 400, Bracco, Milan, Italy) was administered in the antecubital vein. Hereafter, a 20 mL of a 1:1 mixture of contrast and saline and finally 25 mL of saline was administered. CCTA was performed the next beat when the threshold of 300 Hounsfield units (HU) was reached in the descending aorta.

In patients with suspicion of significant stenosis (≥ 50%) at CCTA, adenosine stress CTP was performed at least 20 min after CCTA. Blood pressure and electrocardiogram were monitored during 4 min of continuous adenosine infusion (0,14 mg/kg/min) after which a contrast agent was administered. After reaching a target threshold of 300 HU in the descending aorta CTP images were acquired the next heartbeat scanning 80%-99% of the RR interval. Contrast agent, injection protocol and tube settings were all similar to the CCTA acquisition.

2.3 Data processing

Images were transferred to a workstation and the main branches of the coronary artery tree were automatically extracted from the CCTA. Assessment of the CCTA was done by trained cardiologists with at least 10 years of experience. A luminal stenosis of ≥ 50% was considered significant. Proximal and distal part of the relevant lesion were manually defined using dedicated software (QAngio CT Research Edition v3.1.5.1 Medis Medical Imaging, Leiden, The Netherlands) (Fig. 1). If one vessel, or its side branches had multiple relevant coronary artery lesions we defined only the most proximal one. The most proximal part of the lesion was used as the starting point for calculating the subtended mass.

Further processing of the images was performed using in-house developed MASS software (Leiden University Medical Centre). The CCTA and adenosine stress CTP image data were manually reformatted into a short-axis orientation covering the complete left ventricle with an inter-slice spacing of 4 mm. Subsequently, left ventricular epicardial and endocardial contours were semi-automatically defined in both the CCTA and the adenosine stress CTP images. Using a narrow window width and level setting (W300/

L150) and a slice thickness of 4 mm, perfusion defects were manually drawn in the short axis slices derived from the CTP scan (Fig. 2). Registration was performed to spatially align the CCTA and CTP images and results of image segmentation were exported as 3D objects in VTK format for further analysis and visualization. The software uses the epicardial and endocardial contours from the CCTA for automatically calculating the left ventricular mass.

To assess reproducibility two observers (F.D. and I.H) were blinded to the original contours and a sample of ten cases was randomly selected in which left ventricular epicardial and endocardial contours were again semi-automatically defined and subtended mass was recalculated using the Voronoi-based algorithm. Also, perfusion defects were manually re-drawn and re-measured in grams. Correlations were subsequently tested between new and prior results concerning left ventricular mass, total subtended mass and perfusion defect mass with Pearson's correlation coefficient using SPSS software (version 25, SPSS IBM Corp, Armonk, New York).

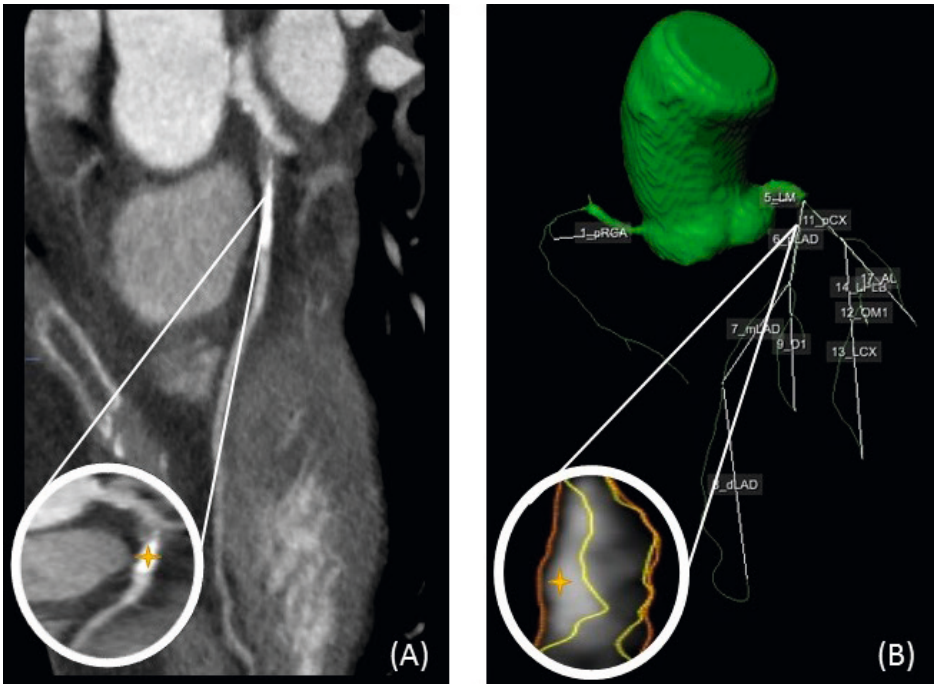

Fig 1. Resting CCTA is used for automatically extracting the main branches of the coronary artery tree (B). A lesion is shown in the proximal left anterior descending (LAD) and marked by the yellow star (A). Subsequently, we can define the proximal LAD stenosis marked by the yellow star (B).

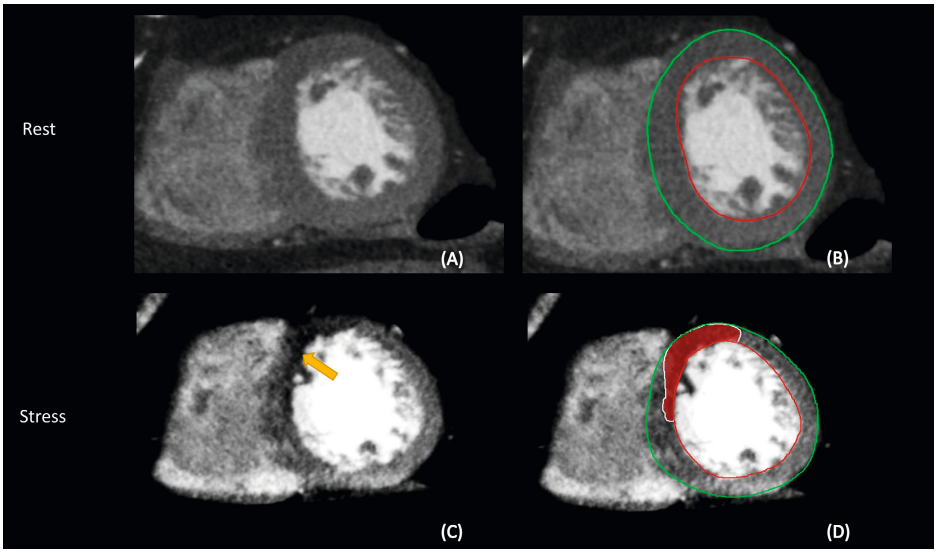

Fig 2. Left ventricular epicardial and endocardial contours were semi-automatically defined in short-axis reformatted images in both the resting CCTA (A, B) and the adenosine stress CTP (C, D). A perfusion defect is marked by the yellow arrow (C). The perfusion defect is manually drawn in the short axis reformatted images from the adenosine stress CTP (D).

2.4 Voronoi-based segmentation

A segmentation algorithm based on the Voronoi method was used on the CCTA in order to find the nearest location of the extracted coronary artery tree for every voxel within the left ventricular myocardium (3). From this data the subtended myocardial mass could be computed, i.e. the left ventricular mass distal from a relevant coronary artery lesion (Fig. 3). Also, the perfusion defect was measured and visualised separately (Fig. 3). An example of a patient with multivessel disease is depicted in Fig. 4. Executing the algorithm for Voronoi based segmentation took approximately 1 min per lesion.

Finally, we quantified the subtended myocardial mass and perfusion defect mass per lesion using bullseye plots with MASS software. This process is depicted in Fig 5. Figure 5A demonstrates the subtended myocardial mass-pictured in red- for one lesion calculated by using our Voronoi-based algorithm. Figure 5B represents the manually drawn perfusion defect. Subsequently, Figure. 5C represent the perfusion defect per lesion by calculating the intersection of figure A and B. For all measurements we used the endo- and epicardial contours from the resting CCTA. Subsequently, we calculated the total subtended mass. See formula:

$$Total\ subtended\ mass = Subtended\ mass\ lesion\ a + subtended\ mass\ lesion\ b$$

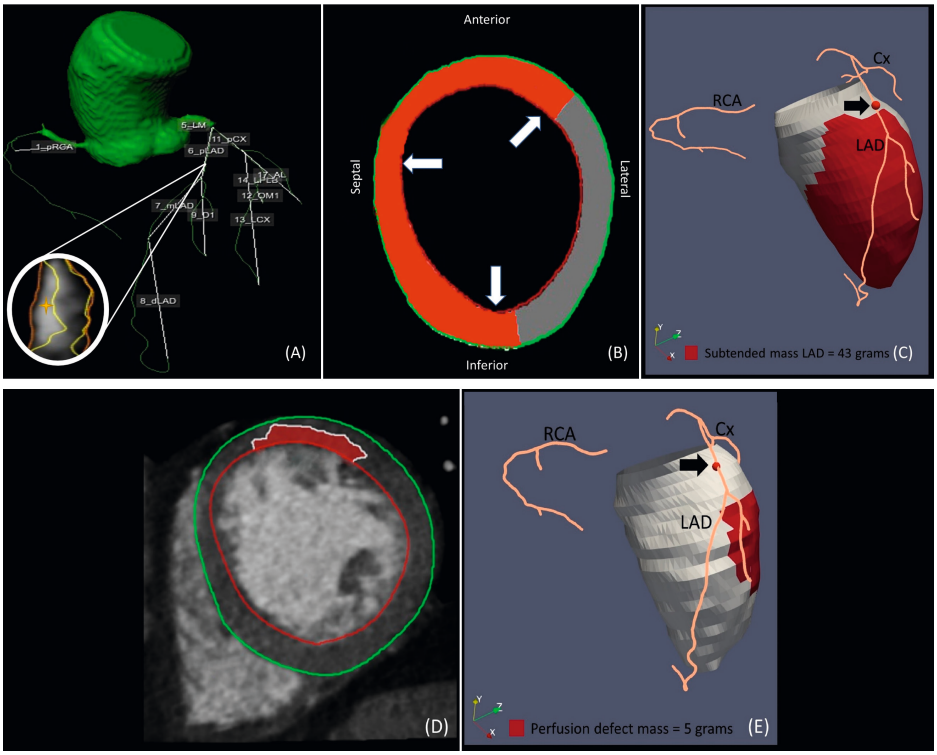

Fig 3. Segmented coronary artery tree and identified relevant coronary artery lesion in the proximal LAD (A) are used for computing the subtended myocardial mass in red in the short-axis view using our Voronoi-based algorithm (B). This can be further visualized in 3D in which the red dot (marked by the black arrow) corresponds to the relevant coronary artery lesion and the red area corresponds to the subtended myocardium which is calculated by our Voronoi-based segmentation as 43 grams (C). The manually drawn perfusion defect (D) is also visualized and quantified (E).

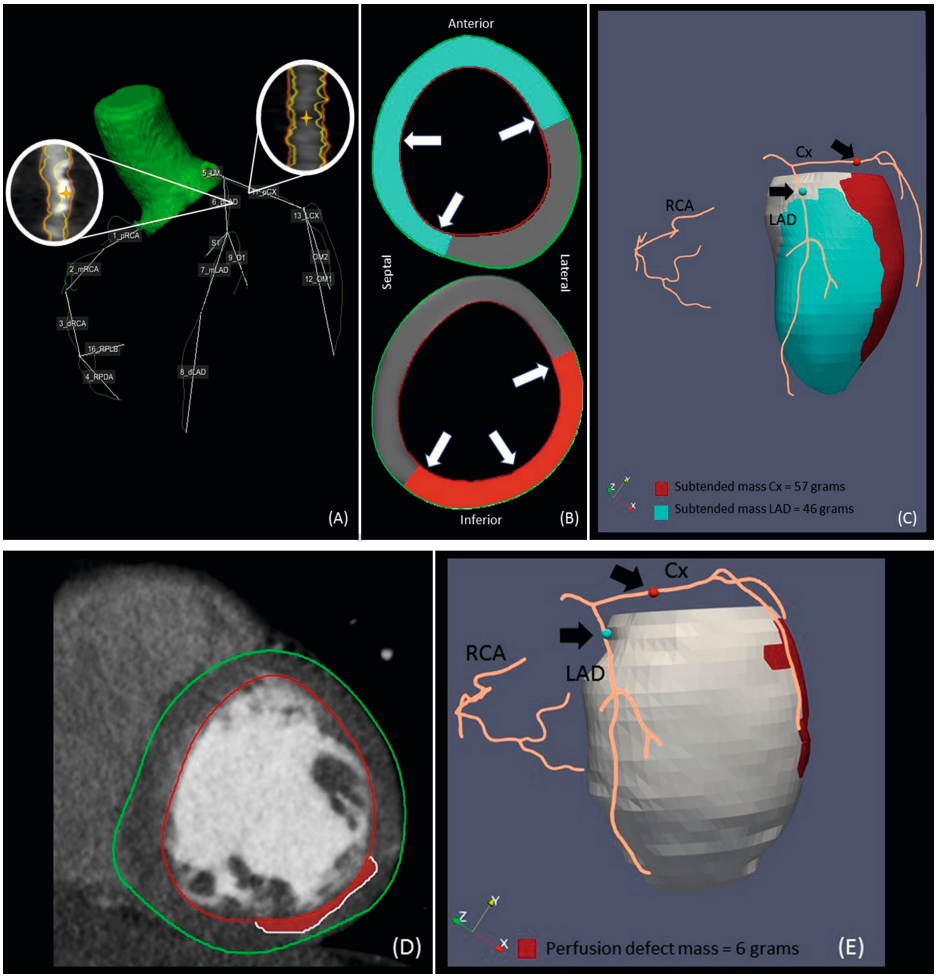

Fig 4. Coronary artery tree and defined relevant lesions in the proximal LAD and circumflex (Cx) (A) are used for computing the subtended myocardial mass in the short-axis view using our Voronoi based algorithm with in cyan the LAD lesion and the Cx lesion in red (B). This can be further visualized in 3D in which the red and cyan dots (marked by the black arrows) correspond to the relevant coronary artery lesions and the red and cyan area correspond to the subtended myocardium for that lesion. We calculated the subtended mass for the Cx lesion and LAD lesion as 57 and 46 grams respectively (C). The manually drawn perfusion defect (D) is also visualised and measured (E).

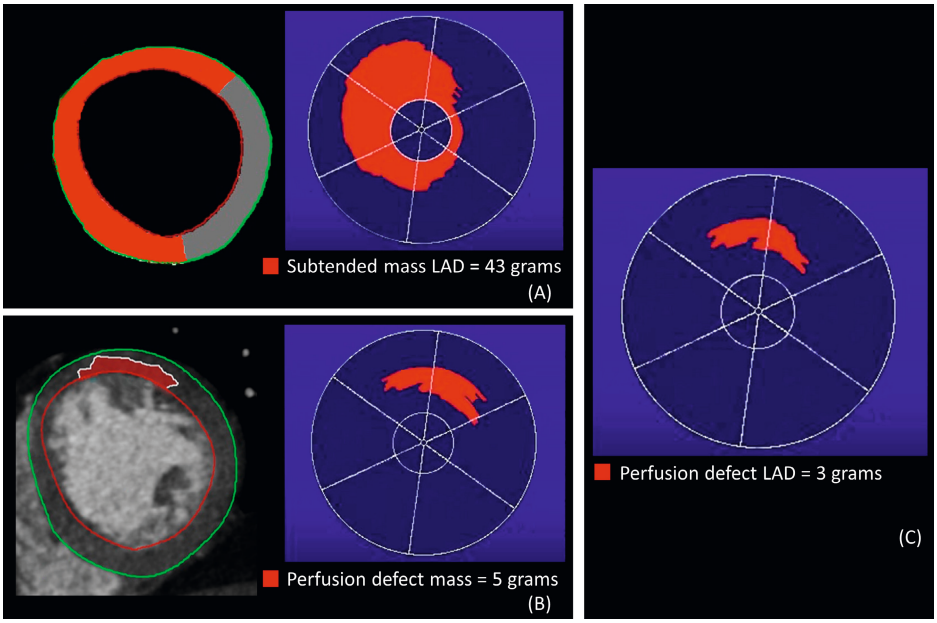

Fig 5. The subtended myocardial mass for one lesion pictured in red is measured in grams (A). The same is done for the perfusion defect (B). Perfusion defect per lesion is measured by calculating the intersection of A and B (C).

3. Results

CCTA and adenosine stress CTP images from 33 patients (20 men, mean age, 67.8 ± 8.2 years) were used for analysis. Table 1 lists patient characteristics. We were able to successfully apply the Voronoi-based segmentation algorithm on all cases to quantify the subtended myocardial mass (per lesion) and perfusion defect mass (per lesion). Left ventricular mass was automatically calculated from the epicardial and endocardial contours with an average value of 118 g. We assessed a total of 64 relevant coronary artery lesions. Average values for total subtended mass, subtended mass per lesion, perfusion defect mass and perfusion defect mass per lesion were 69, 36, 7 and 3 g respectively. In 19/33 patients (58%) the total perfusion defect mass could be distributed over the relevant coronary artery lesion(s). Results were highly reproducible as demonstrated by respectively intra- and inter-observer correlation coefficients for left ventricular mass ($r = 0{,}970$ and $r = 0{,}866$), total subtended mass ($r = 0{,}996$ and $r = 0.990$) and perfusion defect mass ($r = 0{,}844$ and $r = 0{,}822$) ($p < 0.01$ for all). Details concerning the relevant coronary artery lesion(s), left ventricular mass, subtended mass (per lesion) and perfusion defect (per lesion) are shown in Table 2. The relevant coronary artery lesion(s) define the most proximal lesion of the subsequent vessel with a visual diameter stenosis of ≥ 50%. Left ventricular mass encompasses the mass of the left ventricle automatically calculated using epicardial and endocardial contours. The subtended mass per lesion is the

subtended mass calculated by using our Voronoi-based algorithm for a specific lesion. Subsequently total subtended mass can be calculated by adding up the values per lesion. Perfusion defect mass is derived from manual drawing of the perfusion defect. Lastly, the perfusion defect per lesion encompasses the intersection of the perfusion defect and its lesion specific subtended mass. The sum of these lesion specific values encompasses the total mass of the perfusion defect which intersects with the subtended mass of those lesions. The percentage in the last column represents how much of the total (manually drawn) perfusion defect represents the total perfusion defect mass found per lesion.

Patient characteristics

	N=33
Male/Female	20 (61%) / 13 (39%)
Age (years)	67.8 ± 8.2
Hypertension	4 (12%)
Hyperlipidaemia	17 (52%)
Diabetes mellitus	7 (21%)
Family history of CAD	16 (48%)
Smoking	11 (9%)
Single-vessel disease[1]	16 (49%)
Double-vessel disease[2]	10 (30%)
Triple-vessel disease[3]	7 (21%)

Table 1. CAD: Coronary artery disease. 1: Defined as luminal diameter stenosis of ≥50% on CCTA in one major epicardial coronary vessel. 2: Defined as luminal diameter stenosis of ≥50% on CCTA in two major epicardial coronary vessels. 3: Defined as luminal diameter stenosis of ≥50% on CCTA in three major epicardial coronary vessels.

Case	Relevant coronary artery lesion(s)	Left ventricular mass (grams)	Subtended mass per lesion (grams)	Perfusion defect mass (grams)	Perfusion defect mass per lesion (grams)
1	mLAD≥70% dRCA≥50%	98	mLAD 22 dRCA 29 Total 51	11	mLAD 10 dRCA 1 Total 11 (100%)
2	mLAD≥70% D1≥70% dRCA≥ 50%	118	mLAD 15 D1 20 dRCA 49 Total 84	3	mLAD 2 D1 0 dRCA 1 Total 3 (100%)
3	LM≥50% dRCA≥50%	162	LM 94 dRCA 63 Total 157	12	LM 8 dRCA 4 Total 12 (100%)
4	pLAD≥50% Cx≥50%	127	pLAD 46 Cx 57 Total 103	6	pLAD 0 Cx 6 Total 6 (100%)

Case	Relevant coronary artery lesion(s)	Left ventricular mass (grams)	Subtended mass per lesion (grams)	Perfusion defect mass (grams)	Perfusion defect mass per lesion (grams)
5	dRCA≥50% pLAD≥50% AL≥50%	136	pLAD 42 dRCA 21 AL 30 Total 93	9	pLAD 5 dRCA 2 AL 2 Total 9 (100%)
6	pLAD≥50%	220	pLAD 105 Total 105	13	pLAD 13 Total 13 (100%)
7	mLAD≥50%	115	mLAD 63 Total 63	5	mLAD 5 Total 5 (100%)
8	pLAD≥50% Cx≥50%	73	pLAD 38 Cx 17 Total 55	6	pLAD 6 Cx 0 Total 6 (100%)
9	LM≥50%	67	LM 46 Total 46	5	LM 5 Total 5 (100%)
10	pLAD≥50%	90	pLAD 42 Total 42	5	pLAD 5 Total 5 (100%)
11	pLAD≥50% pRCA≥50% Cx≥50%	90	pLAD 33 pRCA 29 Cx 27 Total 89	10	pLAD 2 pRCA 8 Cx 0 Total 10 (100%)
12	mLAD≥50%	87	mLAD 35 Total 35	10	mLAD 10 Total 10 (100%)
13	mLAD≥70% Cx≥50%	255	mLAD 111 Cx 25 Total 136	8	mLAD 8 Cx 0 Total 8 (100%)
14	dLAD≥50% D1≥70% MO≥50% AL≥50%	98	dLAD 7 D1 30 MO 18 AL 10 Total 65	2	dLAD 0 D1 1 MO 0 AL 1 Total 2 (100%)
15	pLAD≥50% mRCA≥50% Cx≥50%	64	pLAD 45 mRCA 13 Cx 9 Total 67	3	pLAD 1 mRCA 2 Cx 0 Total 3 (100%)
16	pLAD≥50% pRCA≥50% Cx≥50%	101	pLAD 40 pRCA 28 Cx 28 Total 96	4	pLAD 2 pRCA 2 Cx 0 Total 4 (100%)
17	pLAD≥50% IM≥70%	102	pLAD 46 IM 34 Total 80	3	pLAD 2 IM 1 Total 3 (100%)
18	pLAD≥50% pRCA≥50%	89	pLAD 62 pRCA 24 Total 86	7	pLAD 4 pRCA 3 Total 7 (100%)
19	pLAD≥50% dRCA≥50% Cx≥50%	104	pLAD 39 dRCA 21 Cx 24 Total 84	7	pLAD 4 dRCA 3 Cx 0 Total 7 (100%)

Case	Relevant coronary artery lesion(s)	Left ventricular mass (grams)	Subtended mass per lesion (grams)	Perfusion defect mass (grams)	Perfusion defect mass per lesion (grams)
20	pLAD≥50% Cx≥50%	106	pLAD 48 Cx 35 Total 83	11	pLAD 10 Cx 0 Total 10 (91%)
21	pLAD≥50%	134	pLAD 45 Total 45	8	pLAD 7 Total 7 (88%)
22	pLAD≥50% pRCA≥70% Cx≥50%	94	pLAD 28 pRCA 0 Cx 51 Total 79	7	pLAD 6 pRCA 0 Cx 0 Total 6 (86%)
23	mLAD≥50% pRCA≥50% Cx≥50%	124	mLAD 36 pRCA 14 Cx 31 Total 81	7	mLAD 6 pRCA 0 Cx 0 Total 6 (86%)
24	pLAD≥70% mRCA≥70% MO≥50%	100	pLAD 38 mRCA 0 MO 25 Total 63	12	pLAD 9 mRCA 0 MO 1 Total 10 (83%)
25	pLAD≥50%	132	pLAD 64 Total 64	8	pLAD 6 Total 6 (75%)
26	mLAD≥50%	139	mLAD 37 Total 37	7	mLAD 5 Total 5 (71%)
27	pLAD≥70%	96	pLAD 43 Total 43	5	pLAD 3 Total 3 (60%)
28	mRCA≥50%	145	mRCA 51 Total 51	5	mRCA 3 Total 3 (60%)
29	mLAD≥50%	110	mLAD 39 Total 39	9	mLAD 5 Total 5 (56%)
30	dLAD≥50% D2≥50%	163	dLAD 43 D2 25 Total 68	4	dLAD 1 D2 1 Total 2 (50%)
31	dLAD≥70%	130	dLAD 22 Total 22	3	dLAD 1 Total 1 (33%)
32	mLAD≥50% pRCA≥50%	133	mLAD 47 pRCA 0 Total 47	4	mLAD 1 pRCA 0 Total 1 (25%)
33	pLAD≥50%	77	pLAD 30 Total 30	5	pLAD 1 Total 1 (20%)

Table 2. LM: left main artery, pLAD: proximal left anterior descending artery, mLAD: mid left anterior descending artery, D1: First diagonal branch, pRCA: Proximal right coronary artery, dRCA: Distal right coronary artery, Cx: Circumflex coronary artery, MO: Margus Obtusus branch. AL: Antero lateral branch. IM: Intermediate branch.

4. Discussion

In this study we propose a method to fully quantify myocardial perfusion defect mass and subtended myocardial mass at adenosine stress CTP related to the significant coronary artery stenosis at CCTA. Results demonstrate that indeed it seems possible to fully quantify perfusion defects and subtended myocardial mass using a Voronoi-based algorithm allowing for quantitative correlation of coronary artery lesions to corresponding areas of myocardial hypoperfusion.

Several studies have demonstrated that adding a myocardial perfusion stress test to CCTA improves the diagnostic accuracy for finding hemodynamically significant coronary artery stenoses as compared to a single modality approach. For instance, Magalhaes et al. demonstrated that In a vessel-based analysis, the addition of CTP led to an improvement in the diagnostic accuracy of the combined analysis when compared to coronary CCTA alone (0.79 [95% CI, 0.77–0.82] vs. 0.73 [95% CI, 0.70–0.76], respectively; $P < 0.0001$ for difference). Also, Ko et al. demonstrated that adding CTP to CCTA improved diagnostic accuracy over CCTA alone as the area under the receiver operating curve increased significantly from 0.798 to 0.893 (p = 0,004) on a per vessel-based analysis (5, 6). Adenosine stress CTP has been shown to be at least as accurate or even superior in the detection of ischemia as compared to single photon emission computed tomography (SPECT) and magnetic resonance imaging (MRI) perfusion. George et al. performed a head to head comparison between CTP and SPECT myocardial perfusion for detecting significant stenoses of 50% or more. It was demonstrated that in the per-vessel analysis, the area under the receiver operating curve of CT perfusion imaging (0.74; 95% CI: 0.71, 0.78) was higher than that of SPECT myocardial perfusion (0.69; 95% CI: 0.66, 0.72) for the diagnosis of a stenosis of at least 50% when considering all vessels ($P = 0.008$) Otton et al. used a perfusion phantom for a direct comparison of the sensitivity of CTP and MRI perfusion in which it was found that the sensitivities of each perfusion modality when directly compared were similar. However, no statistical evidence was given to back this claim. (7, 8). Though nowadays myocardial ischemia on adenosine stress CTP is still assessed semi-quantitatively by visual analysis, quantification of the perfusion defect mass in relation to subtended myocardial mass distal from a significant coronary artery stenosis would be desirable which may help identifying the hemodynamically relevant lesion. As such, Giordano et al. assessed the use of volume of the hypoperfused region calculated from myocardial blood flow at CTP for finding the hemodynamically significant stenosis. They specifically calculated the hypoperfused volume in the myocardial area distal from the stenosis. It was proven that use of the calculated volume had a slightly better accuracy in detecting the hemodynamically significant stenosis as compared to CTP derived myocardial blood flow alone (79% versus 75% respectively) (9). The Voronoi-based algorithm for calculating subtended mass used on CCTA seems reliable in predicting ischemia on SPECT as is demonstrated in a study by Kurata et al. in which there was a moderate correlation between the summed stress score of SPECT and CCTA based

subtended mass as calculated with a Voronoi-based algorithm (r = 0.531 p = 0.001) (10). The same has been done for MRI perfusion by Fukuyama et al. which showed an even better correlation between Voronoi-based calculation of subtended mass and areas of relative hypoperfusion (r = 0.73 p <0.001) (11). Although we were able to apply a Voronoi-based segmentation algorithm on all cases and quantify subtended myocardial mass (per lesion) and perfusion defect mass (per lesion), results from Table 2 show that there was not always agreement between the sum of the myocardial perfusion defect mass per lesion and the total measured myocardial perfusion defect mass. This disagreement can be due to several factors. First of all, only lesions with a visual diameter stenosis of ≥ 50% at CCTA were deemed relevant. However, multiple studies have demonstrated that not only diameter stenosis but also other plaque features contribute to a lesion being hemodynamically significant or not. For instance, Nakazato et al. examined the performance of percent aggregate plaque volume, which represents cumulative plaque volume as a function of total vessel volume by CCTA for identification of ischemic lesions. It was demonstrated that percent aggregate plaque volume provided incremental prediction for lesion ischemia over diameter stenosis (AUC 0.88 [95% CI: 0.78 to 0.99] vs. 0.68 [95% CI: 0.54 to 0.83], respectively; p = 0.02). Also, Yin et al. demonstrated that maximum area stenosis was superior over maximum diameter stenosis in the detection of ischemic lesions (AUC 0.77 versus 0.71 respectively) (12, 13). Also, in a study by van Rosendael et al. assessing the relationship between lumen area stenosis and myocardial ischemia on CTP it was found that 9% of all vessels showed ischemia even though lumen area stenosis was below 50% (14). Subsequently, our defined relevant coronary artery lesion at CCTA will not always correspond to the hemodynamically significant lesion causing the perfusion defect. Secondly, we used only the rest myocardial perfusion scan (CCTA) as reference. Therefore, slight discrepancies in contour size, reference points and thus perfusion defect localization may happen. This may lead to a slight mismatch between total perfusion defect mass and perfusion defect mass per lesion. Finally, for manually drawing perfusion defects visual analysis is still needed and may be susceptible to interpretation errors (15).

Von Spiczak et al. introduced a 3D fusion model for combining adenosine stress CTP and CCTA for correlating the ischemic region to the culprit coronary lesion as defined on invasive coronary angiography (ICA). Yet this method remains semi-quantitative and thus only allows for visual assessment of morphology and function (16). Our method is different as a fully quantitative approach was used allowing not just for intuitive assessment by 3D reconstruction but also for numerical assessment.

Furthermore, a previous study has reported that perfusion territories of coronary arteries vary among individuals. In a per-segment analysis done by Ortiz-Perez et al. 23% of the hyper enhanced regions on cardiac MRI were discordant with the empirically assigned coronary distribution as defined by the standard 17-segment model (17). Use of Voronoi-based segmentation can overcome this problem as its accuracy has been reported in an

animal study using swine hearts in which this method was found to be more accurate than the standard 17-segment model in predicting coronary territories (18, 19).

Results from a study by Dadgar et al. assessing the weight of human hearts demonstrated that weight of the left ventricle varies between 100 and 180 g, which is comparable to our results (20). Tanabe et al. demonstrated that subtended myocardial volume in combination with subtended CT myocardial blood flow derived from CT myocardial perfusion is a better predictor of obstructive CAD than CT myocardial blood flow alone. A Voronoi-based segmentation algorithm was also used for calculating subtended myocardial volume yielding an average of 42.7 mL for obstructive CAD. Our average subtended mass per lesion (36 g) is only slightly lower when taking into account average density of myocardial tissue of 1,055 g/mL to convert mass to volume (21, 22). This could be due to the fact that contrary to Tanabe no ICA was used for verifying the hemodynamical significance of the relevant coronary artery lesion(s).

4.1 Limitations

This study has several limitations which are innate to its retrospective design and novel nature. Selecting patients with only good or excellent imaging quality on adenosine stress CTP may have introduced selection bias. Consequently, the relatively small number of female patients may have introduced further bias as evidence suggests that females may experience higher myocardial perfusion flow values compared to males (23).Since the goal of this study was to provide insights into a new proof of principle more testing and further investigation is needed to implement this concept in a larger patient cohort.

5. Conclusion

Fully quantifying myocardial perfusion defects and subtended myocardial mass allows to quantitatively correlate coronary artery lesions to corresponding areas of myocardial hypoperfusion at CCTA and adenosine stress CTP. This novel technique may prove especially useful for patients with multivessel disease undergoing invasive coronary angiography as correlation of the perfusion defect and coronary artery lesions gives more insight in myocardial ischemia localization.

References

1. Neumann FJ, Sousa-Uva M, Ahlsson A, Alfonso F, Banning AP, Benedetto U, et al. 2018 ESC/EACTS Guidelines on myocardial revascularization. Eur Heart J. 2019;40(2):87-165.
2. Vavere AL, Simon GG, George RT, Rochitte CE, Arai AE, Miller JM, et al. Diagnostic performance of combined noninvasive coronary angiography and myocardial perfusion imaging using 320 row detector computed tomography: design and implementation of the CORE320 multicenter, multinational diagnostic study. J Cardiovasc Comput Tomogr. 2011;5(6):370-81.
3. Guibas L, Stolfi JJAtog. Primitives for the manipulation of general subdivisions and the computation of Voronoi. 1985;4(2):74-123.
4. Mehra VC, Valdiviezo C, Arbab-Zadeh A, Ko BS, Seneviratne SK, Cerci R, et al. A stepwise approach to the visual interpretation of CT-based myocardial perfusion. J Cardiovasc Comput Tomogr. 2011;5(6):357-69.
5. Magalhaes TA, Kishi S, George RT, Arbab-Zadeh A, Vavere AL, Cox C, et al. Combined coronary angiography and myocardial perfusion by computed tomography in the identification of flow-limiting stenosis - The CORE320 study: An integrated analysis of CT coronary angiography and myocardial perfusion. J Cardiovasc Comput Tomogr. 2015;9(5):438-45.
6. Ko SM, Choi JW, Hwang HK, Song MG, Shin JK, Chee HK. Diagnostic performance of combined noninvasive anatomic and functional assessment with dual-source CT and adenosine-induced stress dual-energy CT for detection of significant coronary stenosis. AJR Am J Roentgenol. 2012;198(3):512-20.
7. George RT, Mehra VC, Chen MY, Kitagawa K, Arbab-Zadeh A, Miller JM, et al. Myocardial CT Perfusion Imaging and SPECT for the Diagnosis of Coronary Artery Disease: A Head-to-Head Comparison from the CORE320 Multicenter Diagnostic Performance Study. Radiology. 2015;274(2):626.
8. Otton J, Morton G, Schuster A, Bigalke B, Marano R, Olivotti L, et al. A direct comparison of the sensitivity of CT and MR cardiac perfusion using a myocardial perfusion phantom. J Cardiovasc Comput Tomogr. 2013;7(2):117-24.
9. Giordano M, Poot DH, Coenen A, van Walsum T, Tezza M, Nieman K, et al. Classification of hemodynamically significant stenoses from dynamic CT perfusion and CTA myocardial territories. Med Phys. 2017;44(4):1347-58.
10. Kurata A, Kono A, Sakamoto T, Kido T, Mochizuki T, Higashino H, et al. Quantification of the myocardial area at risk using coronary CT angiography and Voronoi algorithm-based myocardial segmentation. Eur Radiol. 2015;25(1):49-57.
11. Fukuyama N, Kido T, Kurata A, Tanabe Y, Kido T, Yokoi T, et al. Myocardial Segmentation of Area at Risk Based on Coronary Computed Tomography Angiography and Voronoi Diagram in Comparison with Magnetic Resonance Perfusion Imaging. Open Journal of Radiology. 2017;07(01):9-22.
12. Nakazato R, Shalev A, Doh JH, Koo BK, Gransar H, Gomez MJ, et al. Aggregate plaque volume by coronary computed tomography angiography is superior and incremental to luminal narrowing for diagnosis of ischemic lesions of intermediate stenosis severity. J Am Coll Cardiol. 2013;62(5):460-7.
13. Yin P, Dou G, Yang X, Wang X, Shan D, He B, et al. Noninvasive Quantitative Plaque Analysis Identifies Hemodynamically Significant Coronary Arteries Disease. J Thorac Imaging. 2020.
14. van Rosendael AR, Kroft LJ, Broersen A, Dijkstra J, van den Hoogen IJ, van Zwet EW, et al. Relation between quantitative coronary CTA and myocardial ischemia by adenosine stress myocardial CT perfusion. J Nucl Cardiol. 2017;24(4):1253-62.
15. Patel AR, Bamberg F, Branch K, Carrascosa P, Chen M, Cury RC, et al. Society of cardiovascular computed tomography expert consensus document on myocardial computed tomography perfusion imaging. J Cardiovasc Comput Tomogr. 2020;14(1):87-100.
16. von Spiczak J, Manka R, Mannil M, Oebel S, Hamada S, Higashigaito K, et al. 3D fusion of coronary CT angiography and CT myocardial perfusion imaging: Intuitive assessment of morphology and function. J Cardiovasc Comput Tomogr. 2017;11(6):437-43.
17. Ortiz-Perez JT, Rodriguez J, Meyers SN, Lee DC, Davidson C, Wu E. Correspondence between the 17-segment model and coronary arterial anatomy using contrast-enhanced cardiac magnetic resonance imaging. JACC Cardiovasc Imaging. 2008;1(3):282-93.
18. Ide S, Sumitsuji S, Yamaguchi O, Sakata Y. Cardiac computed tomography-derived myocardial mass at risk using the Voronoi-

based segmentation algorithm: A histological validation study. J Cardiovasc Comput Tomogr. 2017;11(3):179-82.
19. Chung MS, Yang DH, Kim YH, Kang SJ, Jung J, Kim N, et al. Myocardial segmentation based on coronary anatomy using coronary computed tomography angiography: Development and validation in a pig model. Eur Radiol. 2017;27(10):4044-53.
20. Dadgar SK, Tyagi SP. Importance of heart weight, weights of cardiac ventricles and left ventricle plus septum/right ventricle ratio in assessing cardiac hypertrophy. Jpn Heart J. 1979;20(1):63-73.
21. Tanabe Y, Kido T, Kurata A, Uetani T, Kuwahara N, Morikawa T, et al. Combined assessment of subtended myocardial volume and myocardial blood flow for diagnosis of obstructive coronary artery disease using cardiac computed tomography: A feasibility study. J Cardiol. 2020.
22. Gheorghe AG, Fuchs A, Jacobsen C, Kofoed KF, Mogelvang R, Lynnerup N, et al. Cardiac left ventricular myocardial tissue density, evaluated by computed tomography and autopsy. BMC Med Imaging. 2019;19(1):29.
23. Nickander J, Themudo R, Sigfridsson A, Xue H, Kellman P, Ugander M. Females have higher myocardial perfusion, blood volume and extracellular volume compared to males - an adenosine stress cardiovascular magnetic resonance study. Sci Rep. 2020;10(1):10380.

5 Correlation between quantification of myocardial area at risk and ischemic burden at cardiac computed tomography

F.Y. van Driest
C.M. Bijns
R.J. van der Geest
A. Broersen
J. Dijkstra
J.W. Jukema
A.J.H.A. Scholte

Abstract

Purpose: This study aims to investigate the correlation between myocardial area at risk at coronary computed tomography angiography (CCTA) and the ischemic burden derived from myocardial computed tomography perfusion (CTP) by using the 17-segment model.

Methods: Forty-two patients with chest pain complaints who underwent a combined CCTA and CTP protocol were identified. Patients with reversible ischemia at CTP and at least one stenosis of ≥ 50% at CCTA were selected. Myocardial area at risk was calculated using a Voronoi-based segmentation algorithm at CCTA and was defined as the sum of all territories related to a ≥ 50% stenosis as a percentage of the total left ventricular (LV) mass. The latter was calculated using LV contours which were automatically drawn using a machine learning algorithm. Subsequently, the ischemic burden was defined as the number of segments demonstrating relative hypoperfusion as a percentage of the total amount of segments (=17). Finally, correlations were tested between the myocardial area at risk and the ischemic burden using Pearson's correlation coefficient.

Results: A total of 77 coronary lesions were assessed. Average myocardial area at risk and ischemic burden for all lesions was 59% and 23%, respectively. Correlations for ≥ 50% and ≥ 70% stenosis based myocardial area at risk compared to ischemic burden were moderate ($r = 0.564$; $p < 0.01$) and good ($r = 0.708$; $p < 0.01$), respectively.

Conclusion: The relation between myocardial area at risk as calculated by using a Voronoi-based algorithm at CCTA and ischemic burden as assessed by CTP is dependent on stenosis severity.

Abbreviations

AUC: Area under the curve
CAD: Coronary artery disease
CCTA: Coronary computed tomography angiography
CTP: Computed tomography perfusion
CX: Circumflex artery
ECG: Electrocardiogram
FFR: Fractional flow reserve
LAD: Left anterior descending artery
LV: Left ventricle
MBF: Myocardial blood flow
MRI: Magnetic resonance imaging
RCA: Right coronary artery
SPECT: Single photon emission computed tomography
VTK: Visualization toolkit

1. Introduction

Coronary computed tomography angiography (CCTA) is widely used to diagnose coronary artery disease (CAD) and determine stenosis severity (1). However, the assessment of ischemic myocardium is also of prognostic importance and plays a vital role in the decision to revascularize patients which depends on the extent of the relative hypoperfused (ischemic) myocardium, relative to the subtended myocardial mass distal of the coronary stenosis (2). A key advantage of combining CCTA and adenosine stress CT myocardial perfusion (CTP) is that it allows for both the assessment of coronary artery stenosis as well as myocardial ischemia (2). Also, CTP has a substantially shorter exam time as compared to cardiac magnetic resonance (CMR) and myocardial perfusion imaging (MPI). Furthermore, CTP may be especially beneficial in patients with contraindications for CMR (3, 4). However, it must be noted that a major disadvantage of CTP is the relatively high radiation dose exposure. Still, this is gradually improving thanks to technological advancement (4).

The Voronoi decomposition encompasses a mathematical algorithm that divides a three-dimensional space or two-dimensional area between predetermined points based on the shortest distance to those points. This algorithm can be used to partition the myocardium according to which blood vessel is closest (5, 6). By using a Voronoi decomposition algorithm on myocardial tissue one can take into account the many variations that exist in coronary anatomy. This is a major advantage of the aforementioned method over the standard 17 segment model in which the segments correspond to a fixed location and do not change according to differences in coronary anatomy (7). The importance of using a different approach for the assessment of the coronary distribution was demonstrated in a study by OrtizPerez et al. in which in patients who underwent CMR 23% of the hyper enhanced segments were discordant with the empirically assigned coronary distribution according to the standard 17segment model. A Voronoi based segmentation algorithm can overcome this problem as its output is dependent on patient specific coronary anatomy (6, 8).

Artificial intelligence (AI) is rapidly evolving in the work field of cardiovascular imaging and can greatly lessen the time needed for image processing, Machine learning which is a subclass of AI allows for the creation of a model based on historical data. As such, machine learning has been widely used for automatic left ventricle (LV) segmentation greatly speeding up the process of LV contour placement (9, 10),

The aim of this study was to assess whether the subtended myocardial mass as calculated by using the Voronoi-based segmentation method correlated to myocardial ischemia at CTP. As such, CCTA may not only be used to assess the degree of a coronary stenosis, but also for the quantification of the subtended myocardial mass which may predict the ischemic burden without the need for a stress test.

2. Materials and Methods

2.1 Patients

248 patients referred for a combined CCTA and CTP protocol due to chest pain complaints were identified. Patients with normal CTP images or fixed perfusion defects (N = 178), absence of at least one ≥ 50% coronary stenosis (N = 11), inferior CTP scan quality (N = 16) and prior coronary revascularization (N = 1) were excluded (11). We selected a total of 42 patients for the current analysis. A detailed flowchart of the patient selection is depicted in Fig. 1. CTP scan quality classified as either "poor" or " fair" was deemed inferior. All data were retrospectively analyzed. The local ethics committee of the Leiden University Medical Center approved this retrospective analysis of clinical data and the need for informed consent was waived.

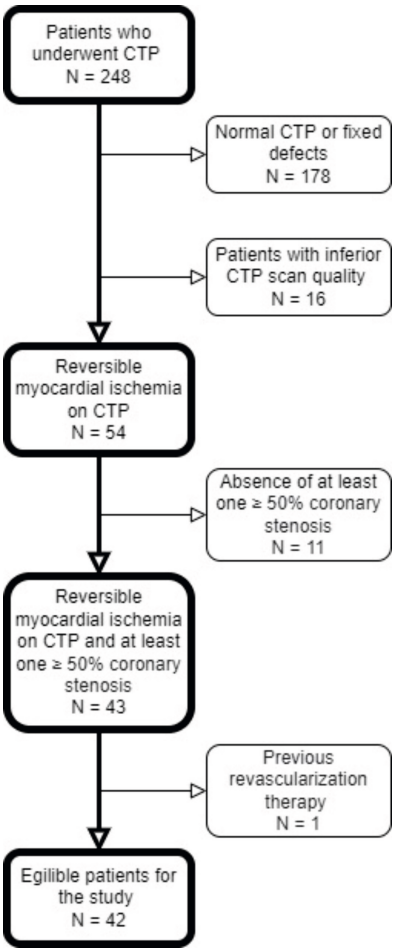

Figure 1. Flowchart depicting the selection proces of patients. CTP scans with "poor" or "fair" scan quality were deemed inferior.

2.2 Data acquisition

Using a 320-row volumetric scanner (Aquilion ONE, Canon Medical Systems and Aquilion ONE Genesis Edition, Canon Medical Systems, Otawara, Japan) CCTA and static adenosine stress CTP were acquired on the same day. Patients were advised not to consume caffeine products 24 h before examination. One hour prior to CCTA blood pressure and heart rate were monitored. Patients with a heart rate exceeding 60 beats per minutes (bpm) were given metoprolol, 25 mg up to 150 mg orally, unless contraindications were present. Additionally, metoprolol could be injected intravenously if the heart rate remained above 60 bpm.

Sublingual administration of nitroglycerin (0.4 mg) was done prior to CCTA. Scanner settings for CCTA were as follows: A detector collimation of 320 x 0.5 mm, a 275 ms gantry rotation time and temporal resolution of 137 ms for the Aquilion ONE Genesis Edition and a detector collimation of 320 x 0.5 mm, 350 ms gantry rotation time and temporal resolution of 175 ms for the Aquilion ONE. Tube current was 140-580mA and a peak tube voltage 100-135kV. The antecubital vein was used for administration of 50-90 mL of contrast agent (Iomeron 400, Bracco, Milan, Italy) followed by a 1:1 mixture of 20 mL contrast and saline and finally 25 mL of saline. Tube current, peak tube voltage and the amount of administered contrast agent varied due to variations in patient size (12). Using prospective electrocardiogram (ECG) triggering 70%-80% of the RR interval was scanned. In patients with a heart rate exceeding 65 bpm 30%-80% of the RR-interval was scanned. When a threshold of 300 Hounsfield units (HU) was reached in the descending aorta CCTA was performed the next beat.

CTP was only performed if there was suspicion of a significant stenosis (≥ 50%) at CCTA. To achieve adequate myocardial contrast wash-out the minimum scan-interval was 20 min between CCTA and CTP. ECG and blood pressure were continuously monitored following continuous adenosine infusion (0.14mg/kg/min) after which a contrast agent was administered. CTP images were acquired when a threshold of 300 HU was reached in the descending aorta scanning 80%-99% of the RR interval. Tube settings, injection protocol and contrast agent were all similar to the CCTA acquisition.

2.3 Image analysis

Images were transferred to a workstation and analyzed using dedicated post-processing software (Vitrea FX 7.12; Vital Images, Minnetonka, Minnesota). All CCTA and CTP images were analysed by trained cardiologists with at least 10 years of experience. In accordance with SCCT guidelines, stenosis severity per segment was semi quantitatively assessed using visual analysis as: 50%-69% (moderate), 70%-99% (severe), and 100% (occluded) (13). In case multiple stenoses were observed in the same segment and vessel, the most proximal stenosis was labelled as the culprit stenosis.

CTP images were analysed by reconstructing cardiac phases for every 2% of the scanned interval. Subsequently, analysis was performed on the phase with the best scan quality using short-axis reformatted images and a slice thickness of 4 mm using a narrow window width and level setting (W300/L150) and utilizing the standard 17 segment myocardial model for scoring (14). If one or more segments demonstrated signs of relative hypoperfusion the CTP was considered abnormal (11). The number of segments with relative hypoperfusion relative to the total of 17 segments was defined as the ischemic burden and calculated using the following formula:

$$Ischemic\ burden = \frac{number\ of\ segments\ with\ relative\ hypoperfusion}{17} * 100$$

2.4 Image processing

Before executing the Voronoi-based segmentation algorithm the complete coronary artery tree was automatically extracted from the CCTA (Fig. 2A) and the relevant lesions were manually defined using dedicated software (Fig. 2B) (QAngio CT Research Edition v3.1.5.1 Medis Medical Imaging, Leiden, The Netherlands). Hereafter, the CCTA images were automatically reformatted into a short-axis orientation covering the complete left ventricle with an inter-slice spacing of 4 mm. Subsequently, left ventricular epicardial and endocardial contours were automatically drawn in the CCTA (Fig. 3). Both tasks were done semi automatically using in house developed MASS software (Leiden University Medical Center) by using a machine learning model, manual corrections were made if needed. This model was trained using a different dataset of 50 randomly selected CCTA's in which reformatting of the short axis and drawing of the LV epicardial and endocardial contours was done manually. Subsequently we used dedicated open-source software (TensorFlow v2.6 software available from www.tensorflow.org) to train a neural network. Executing the machine learning model took approximately 1 min and 20 s per CCTA.

To assess the feasibility of the machine learning model as compared to manual measurements one observer (F.Y. with 3 years of experience in cardiovascular imaging analysis) randomly selected a sample of 10 cases in which manual reformatting of the short axis and manual drawing of the left ventricular epicardial and endocardial contours was performed. Correlations were subsequently tested between manual and automatic measurements concerning the left ventricular mass which is derived from the epicardial and endocardial contours. Statistical analysis of these correlations was done using Pearson's correlation coefficient using SPSS software (version 25, SPSS IBM Corp, Armonk, New York).

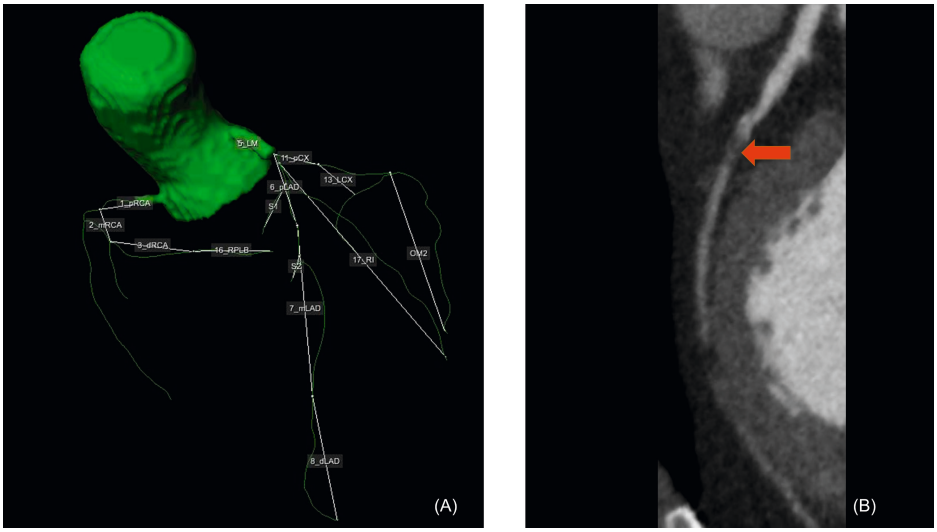

Figure 2. The complete coronary tree was automatically extracted from the CCTA (Panel A.). The proximal part of the lesion in the proximal LAD as marked by the red arrow (Panel B) is used as the starting point for calculating the subtended mass.

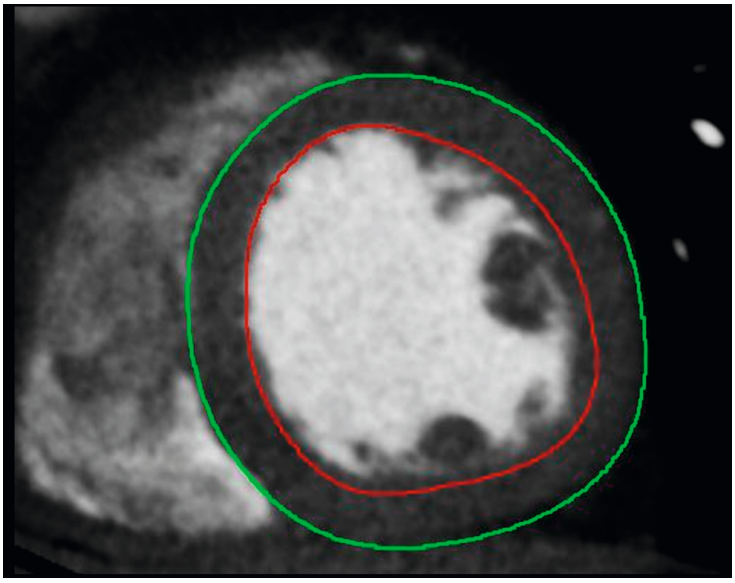

Figure 3. Epicardial contours (green line) and endocardial contours (red line) were automatically drawn using a machine learning model.

2.4 Voronoi-based segmentation

In order to calculate the subtended mass a Voronoi-based segmentation algorithm was used on the CCTA by using in-house developed MASS software (Leiden University Medical Center). By using this algorithm it is possible to find the nearest location of the extracted coronary artery tree for every voxel within the left ventricular myocardium (5, 6). Subsequently, results of the image segmentation were exported as 3D objects in the visualization toolkit (VTK) format for further analysis and visualization (Fig. 4). Executing the Voronoi-based segmentation algorithm took approximately 1 min per lesion.

Finally, the subtended mass was calculated for both ≥ 50% and ≥ 70% stenosis as a percentage of the total LV mass and defined as the myocardial area at risk using the following formula:

$$myocardial\,area\,at\,risk = \frac{Subtended\,mass}{LV\,mass} * 100$$

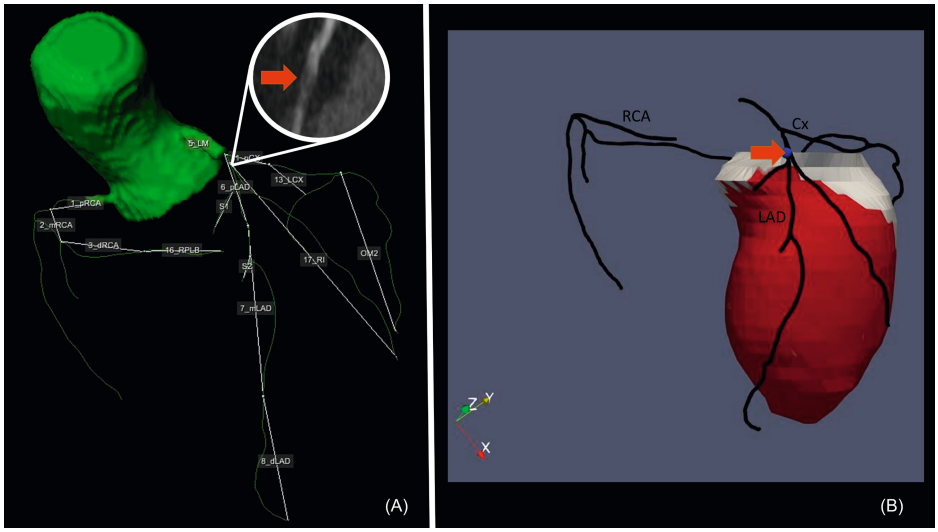

Figure 4. Using the previously defined lesion in the proximal LAD (Panel A) and executing the Voronoi-based algorithm the subtended mass can be computed and visualized in 3D (Panel B).

2.5 Statistical analysis

Correlations between the ischemic burden and myocardial area at risk as well as correlations between manual and machine learning based LV contours were calculated using Pearson's correlation coefficient. All analysis were performed using SPSS software (version 25, SPSS IBM Corp, Armonk, New York).

3. Results

CCTA and CTP images from forty-two patients (25 men, mean age, 68.2 ± 7.7) were used for the current analysis. Patient characteristics are listed in Table 1. Voronoi-based segmentation and semi-automatic drawing of the LV epi- and endocardial contours using a machine learning algorithm was successful in all cases. A total of 77 coronary lesions with a luminal stenosis of ≥ 50% were assessed. Average myocardial area at risk for stenosis ≥ 50% and ≥ 70% were 59% and 37%, respectively. Average ischemic burden for stenosis ≥50% and ≥70% were 23% and 24%, respectively. There was a moderate correlation of the ischemic burden versus myocardial area at risk for stenosis of ≥ 50% ($r = 0.564$; $p < 0.01$) (Fig. 5). A good correlation was found for the ischemic burden versus the area at risk for stenosis of ≥ 70% ($r = 0.708$; $p < 0.01$) (Fig. 6). A complete example is depicted in figure 7.

Comparison of the LV mass as calculated from manually drawn contours versus contours drawn with the machine learning model demonstrated a very good correlation ($r = 0.870$; $p < 0.01$).

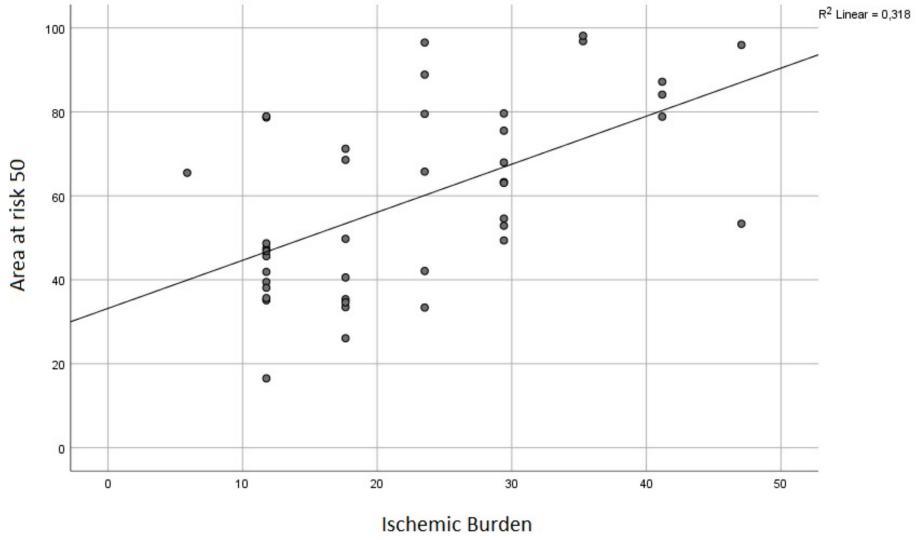

Figure 5. "Area at risk 50" represents the percentage of myocardial area at risk of the total LV as calculated by using the Voronoi-based segmentation algorithm for every ≥50% stenosis. "Ischemic burden" represents the percentage of segments with relative hypoperfusion of the total amount of segments (=17)

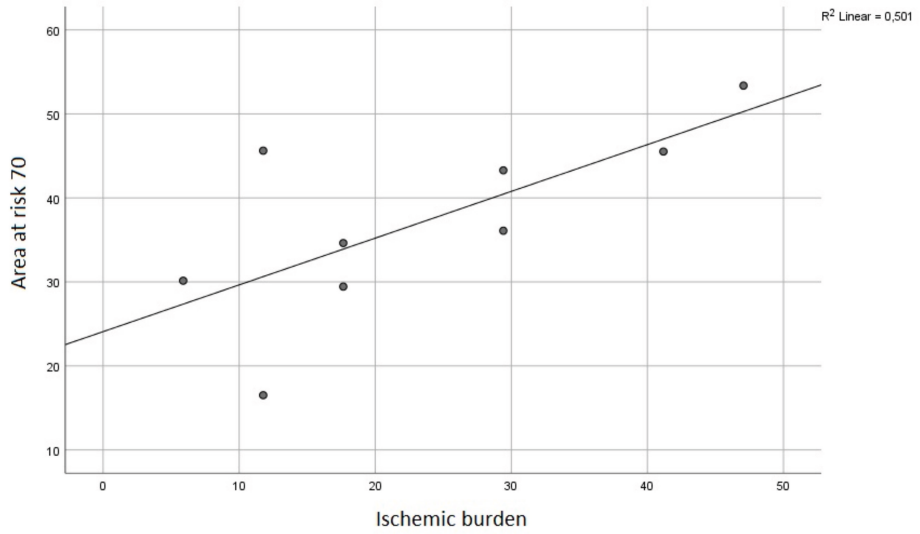

Figure 6. "Area at risk 70" represents the percentage of myocardial area at risk of the total LV as calculated by using the Voronoi-based segmentation algorithm for every ≥70% stenosis. "Ischemic burden" represents the percentage of segments with relative hypoperfusion of the total number of segments (=17)

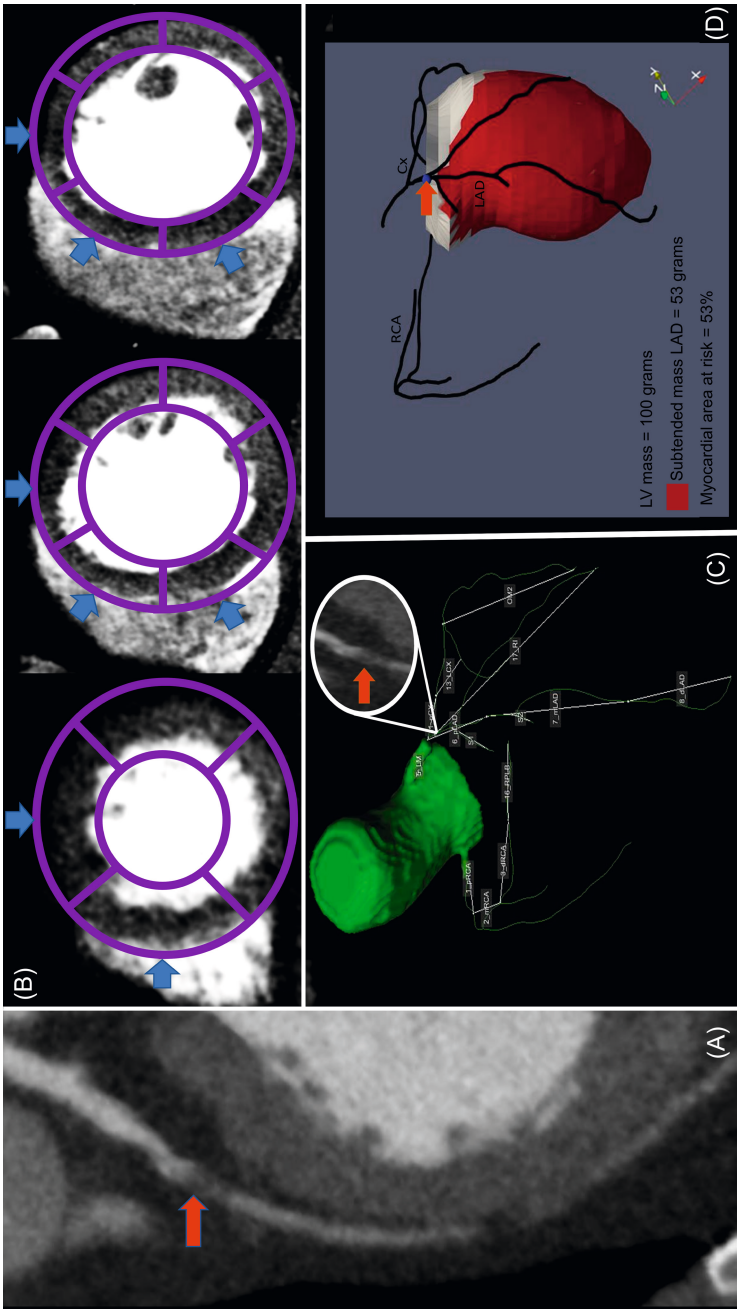

Figure 7. Example of a 58-year-old male with single vessel disease. A significant stenosis is present in the proximal LAD with contrast opacification distally (Panel A). Perfusion defects assessed by CTP can be seen in panel B. The ischemic burden can consequently be calculated as 8/17 *100 ≈ 47 %. The complete coronary tree with the relevant stenosis is shown in panel C. Using the previously mentioned stenosis the subtended mass is calculated by using the Voronoi-based segmentation algorithm. Subsequently, the myocardial area at risk is calculated as 53/100 * 100 = 53%.

Patient characteristics

	N=42
Male/Female	25 (60%) / 17 (40%)
Age (years)	68.2 ± 7.7
Hypertension	23 (55%)
Hyperlipidaemia	22 (52%)
Diabetes mellitus	9 (21%)
Family history of CAD	22 (52%)
Smoking	3 (7%)
Single-vessel disease[1]	24 (57%)
Double-vessel disease[2]	10 (24%)
Triple-vessel disease[3]	8 (19%)

Table 1. CAD: Coronary artery disease. 1: Defined as luminal diameter stenosis of ≥ 50% on CCTA in one major epicardial coronary vessel. 2: Defined as luminal diameter stenosis of ≥ 50% on CCTA in two major epicardial coronary vessels. 3: Defined as luminal diameter stenosis of ≥ 50% on CCTA in three major epicardial coronary vessels.

4. Discussion

This study assessed the relationship between myocardial area at risk at CCTA and ischemic burden as assessed at CTP. Our results demonstrate that calculating subtended mass using a Voronoi-based segmentation algorithm in combination with a machine learning algorithm for semi-automatically drawing LV epi- and endocardial contours at CCTA is feasible and its correlation to the ischemic burden as measured using a standard 17-segment model at CTP increases with increasing stenosis severity. Consequently, coronary CTA can be used not only to assess the degree of a coronary stenosis, but also for quantification of the subtended myocardial mass which may predict the ischemic burden without the need for a stress test. It should however be noted that the use of integrated diagnostics of CCTA and CTP is still better than CCTA alone as the first allows for both assessment of coronary stenosis as well as the presence of (reversible) ischemia. This is of great importance as not every coronary stenosis is hemodynamically significant (15).

Multiple studies have demonstrated that adding CTP to regular CCTA improves the detection of hemodynamically significant coronary lesions (16, 17). For instance, Pontone et al. demonstrated that addition of CTP to CCTA improved the detection of functional significant coronary lesions. In a vessel-based model addition of CTP to CCTA yielded an improvement of specificity (94%; $p < 0.001$), positive predictive value (86%; $p < 0.001$), and accuracy (93%; $p = 0.002$). Similarly, in a patient-based model, improvements in specificity (83%; $p < 0.001$), positive predictive value (86%; $p = 0.02$), and accuracy (91%; $p = 0.004$) were also observed when stress CTP was combined with CCTA (16).

Aside from the degree of coronary stenosis there have been several studies assessing the relationship between the anatomical location of a coronary stenosis and the presence of myocardial ischemia. For instance, in a study by Tanabe et al. the combined diagnostic performance of coronary artery stenosis-subtended myocardial volume and myocardial blood flow (MBF) on CTP for detecting obstructive coronary artery disease was assessed. It was found that the AUC of the combined use of the subtended CTP myocardial blood flow and subtended mass was significantly higher than that of myocardial blood flow alone in the detection of hemodynamically significant stenoses (0.89 vs. 0.75, 0.77; $p<0.05$) (18).

Ide et al. demonstrated the feasibility and validity of Voronoi-based tissue segmentation. It was found that CCTA based subtended myocardial mass calculated using a Voronoi-based segmentation algorithm closely corresponded to actual subtended mass measured on ex-vivo-sine hearts ($r = 0.92$, $p = 0.02$ for the left anterior descending artery (LAD); $r = 0.96$, $p = 0.009$ for the circumflex artery (CX); $r = 0.96$, $p = 0.009$ for the right coronary artery (RCA)) (19).

Semi-automatic segmentation of the LV using a machine learning model for defining epi- and endocardial contours has been validated extensively. Several studies have reported high comparability to a manual segmentation of the LV versus a machine learning approach (20-23). It must also be noted that manually drawing epi- and endocardial contours is a time-intensive process of usually around 20-30 min(20). Semi-Automatic LV segmentation can speed up this process significantly as we have noted an execution time of approximately 1 min and 20 s.

Kurata et al. also assessed the relationship between calculated subtended mass at CCTA using a Voronoi-based segmentation algorithm and ischemic burden as assessed by single photon emission computed tomography (SPECT). A moderate correlation was found between the calculated subtended mass and ischemic burden ($r=0.531$; $p=0.001$) which is only slightly lower compared to our results ($r = 0.564$; $p < 0.01$) (24). Also, Fukuyama et al. performed a similar study by assessing the relationship between calculated subtended mass at CCTA using a Voronoi-based segmentation algorithm and ischemic burden as assessed by magnetic resonance imaging (MRI). A slightly better correlation was found when correlating subtended mass to ischemic burden ($r = 0.73$; $p < 0.001$) (25). This difference in correlation may be partially explained by the fact that cardiac MRI perfusion is still superior to cardiac CTP in the detection of (reversible) ischemia (26).

Interestingly, in our study lesions with a diameter stenosis of 70% or more demonstrated a better correlation between the myocardial area at risk and ischemic burden compared to lesions with a diameter stenosis of 50% ($r=0.708$ and $r=0.564$ respectively). A similar observation was found by Fukuyama et al. (25). This difference in correlation may be attributed to the fact that lesions with a greater diameter stenosis may cause more

(reversible) ischemia and hereby enlarge the ischemic burden. Van Rosendael et al. clearly demonstrated the relationship between quantitative CCTA lesion measurements and myocardial ischemia at CTP. It was confirmed that increasing stenosis percentage by quantitative CCTA is positively correlated to myocardial ischemia (15). Furthermore, a recent study by Bax et al. demonstrated that lesions in left sided coronary arteries with a larger diameter stenosis were often localized more distally in the subsequent vessel. Thus, explaining the better correlation for lesions with a diameter stenosis of 70% or more as these accompany for a lower subtended mass (27).

4.1 Limitations

This study has several limitations which are inherent to its retrospective design. Firstly, the amount of analyzed patients is small which may have influenced the strength of the statistical analysis. Hence, future studies with a larger number of patients will be required to clarify the significance of these findings in clinical practice. Selection bias may have been introduced as we only selected patients with reversible ischemia as diagnosed on CTP. Secondly, the subtended mass was calculated using the anatomical location of the relevant coronary lesion. This was independent of whether the lesion was hemodynamically significant or not. In case of multivessel disease the correlation between subtended mass and ischemic burden may have been biased as we solely selected the most proximal lesions for calculating the subtended mass. Of course, the most proximal lesions also encompass the largest subtended mass. Also, there was no validation of the ischemic burden to the corresponding anatomical territory that corresponds to the relevant coronary artery lesion used for calculating the myocardial area at risk (28). Thirdly, the Voronoi-based segmentation algorithm does not take into account the curved surface of the myocardium but derives the distance the between the coronary vessels and every myocardial voxel by using a straight line. As distances are relatively small we feel the impact of not using the myocardial curvature on the final output will be very minimal. Lastly, we must acknowledge that no inter- or intra-observer measurements were done on the CCTA or CTP analysis. However, prior studies have reported excellent and moderate inter- and intra-observer agreements for both imaging modalities. (6, 29).

5. Conclusions

Quantification of the myocardial area at risk calculated by using a Voronoi-based algorithm in combination with a machine learning based algorithm for LV segmentation at CCTA significantly correlates with the ischemic burden as assessed by the standard 17-segment model at CTP. This correlation improves with increasing stenosis degree. This relationship may be beneficial in risk assessment of patients with CAD and may aid in clinical-decision making.

References

1. Abdelrahman KM, Chen MY, Dey AK, Virmani R, Finn AV, Khamis RY, et al. Coronary Computed Tomography Angiography From Clinical Uses to Emerging Technologies: JACC State-of-the-Art Review. J Am Coll Cardiol. 2020;76(10):1226-43.
2. Vavere AL, Simon GG, George RT, Rochitte CE, Arai AE, Miller JM, et al. Diagnostic performance of combined noninvasive coronary angiography and myocardial perfusion imaging using 320 row detector computed tomography: design and implementation of the CORE320 multicenter, multinational diagnostic study. J Cardiovasc Comput Tomogr. 2011;5(6):370-81.
3. Techasith T, Cury RC. Stress Myocardial CT Perfusion: An Update and Future Perspective. JACC: Cardiovascular Imaging. 2011;4(8):905-16.
4. Punzo B, Cavaliere C, Maffei E, Bossone E, Saba L, Cademartiri F. Narrative review of cardiac computed tomography perfusion: insights into static rest perfusion. Cardiovasc Diagn Ther. 2020;10(6):1946-53.
5. Guibas L, Stolfi J. Primitives for the manipulation of general subdivisions and the computation of Voronoi. ACM Trans Graph. 1985;4(2):74–123.
6. van Driest FY, van der Geest RJ, Broersen A, Dijkstra J, El Mahdiui M, Jukema JW, et al. Quantification of myocardial ischemia and subtended myocardial mass at adenosine stress cardiac computed tomography: a feasibility study. Int J Cardiovasc Imaging. 2021.
7. Cerqueira MD, Weissman NJ, Dilsizian V, Jacobs AK, Kaul S, Laskey WK, et al. Standardized Myocardial Segmentation and Nomenclature for Tomographic Imaging of the Heart. Circulation. 2002;105(4):539-42.
8. Ortiz-Perez JT, Rodriguez J, Meyers SN, Lee DC, Davidson C, Wu E. Correspondence between the 17-segment model and coronary arterial anatomy using contrast-enhanced cardiac magnetic resonance imaging. JACC Cardiovasc Imaging. 2008;1(3):282-93.
9. van Assen M, Muscogiuri G, Caruso D, Lee SJ, Laghi A, De Cecco CN. Artificial intelligence in cardiac radiology. La radiologia medica. 2020;125(11):1186-99.
10. Coppola F, Faggioni L, Gabelloni M, De Vietro F, Mendola V, Cattabriga A, et al. Human, All Too Human? An All-Around Appraisal of the "Artificial Intelligence Revolution" in Medical Imaging. Frontiers in Psychology. 2021;12.
11. Mehra VC, Valdiviezo C, Arbab-Zadeh A, Ko BS, Seneviratne SK, Cerci R, et al. A stepwise approach to the visual interpretation of CT-based myocardial perfusion. J Cardiovasc Comput Tomogr. 2011;5(6):357-69.
12. Abbara S, Blanke P, Maroules CD, Cheezum M, Choi AD, Han BK, et al. SCCT guidelines for the performance and acquisition of coronary computed tomographic angiography: A report of the Society of Cardiovascular Computed Tomography Guidelines Committee: Endorsed by the North American Society for Cardiovascular Imaging (NASCI). Journal of Cardiovascular Computed Tomography. 2016;10(6):435-49.
13. Leipsic J, Abbara S, Achenbach S, Cury R, Earls JP, Mancini GJ, et al. SCCT guidelines for the interpretation and reporting of coronary CT angiography: a report of the Society of Cardiovascular Computed Tomography Guidelines Committee. J Cardiovasc Comput Tomogr. 2014;8(5):342-58.
14. Cerqueira MD, Weissman NJ, Dilsizian V, Jacobs AK, Kaul S, Laskey WK, et al. Standardized myocardial segmentation and nomenclature for tomographic imaging of the heart. A statement for healthcare professionals from the Cardiac Imaging Committee of the Council on Clinical Cardiology of the American Heart Association. Circulation. 2002;105(4):539-42.
15. van Rosendael AR, Kroft LJ, Broersen A, Dijkstra J, van den Hoogen IJ, van Zwet EW, et al. Relation between quantitative coronary CTA and myocardial ischemia by adenosine stress myocardial CT perfusion. Journal of Nuclear Cardiology. 2017;24(4):1253-62.
16. Pontone G, Andreini D, Guaricci AI, Baggiano A, Fazzari F, Guglielmo M, et al. Incremental Diagnostic Value of Stress Computed Tomography Myocardial Perfusion With Whole-Heart Coverage CT Scanner in Intermediate- to High-Risk Symptomatic Patients Suspected of Coronary Artery Disease. JACC Cardiovasc Imaging. 2019;12(2):338-49.
17. Nishiyama H, Tanabe Y, Kido T, Kurata A, Uetani T, Kido T, et al. Incremental diagnostic value of whole-heart dynamic computed tomography perfusion imaging for detecting obstructive coronary artery disease. J Cardiol. 2019;73(5):425-31.
18. Tanabe Y, Kido T, Kurata A, Uetani T, Kuwahara N, Morikawa T, et al. Combined assessment of subtended myocardial volume and myocardial blood flow for diagnosis of obstructive coronary artery disease using cardiac computed

tomography: A feasibility study. J Cardiol. 2020;76(3):259-65.
19. Ide S, Sumitsuji S, Yamaguchi O, Sakata Y. Cardiac computed tomography-derived myocardial mass at risk using the Voronoi-based segmentation algorithm: A histological validation study. J Cardiovasc Comput Tomogr. 2017;11(3):179-82.
20. Koo HJ, Lee JG, Ko JY, Lee G, Kang JW, Kim YH, et al. Automated Segmentation of Left Ventricular Myocardium on Cardiac Computed Tomography Using Deep Learning. Korean J Radiol. 2020;21(6):660-9.
21. Bruns S, Wolterink JM, Takx RAP, van Hamersvelt RW, Suchá D, Viergever MA, et al. Deep learning from dual-energy information for whole-heart segmentation in dual-energy and single-energy non-contrast-enhanced cardiac CT. Med Phys. 2020;47(10):5048-60.
22. Zreik M, Lessmann N, van Hamersvelt RW, Wolterink JM, Voskuil M, Viergever MA, et al. Deep learning analysis of the myocardium in coronary CT angiography for identification of patients with functionally significant coronary artery stenosis. Med Image Anal. 2018;44:72-85.
23. Jun Guo B, He X, Lei Y, Harms J, Wang T, Curran WJ, et al. Automated left ventricular myocardium segmentation using 3D deeply supervised attention U-net for coronary computed tomography angiography; CT myocardium segmentation. Med Phys. 2020;47(4):1775-85.
24. Kurata A, Kono A, Sakamoto T, Kido T, Mochizuki T, Higashino H, et al. Quantification of the myocardial area at risk using coronary CT angiography and Voronoi algorithm-based myocardial segmentation. Eur Radiol. 2015;25(1):49-57.
25. Fukuyama N, Kido T, Kurata A, Tanabe Y, Kido T, Yokoi T, et al. Myocardial Segmentation of Area at Risk Based on Coronary Computed Tomography Angiography and Voronoi Diagram in Comparison with Magnetic Resonance Perfusion Imaging. Open Journal of Radiology. 2017;07:9-22.
26. Dewey M, Siebes M, Kachelrieß M, Kofoed KF, Maurovich-Horvat P, Nikolaou K, et al. Clinical quantitative cardiac imaging for the assessment of myocardial ischaemia. Nature Reviews Cardiology. 2020;17(7):427-50.
27. Bax AM, Yoon YE, Gianni U, Ma X, Lu Y, Lee BC, et al. Plaque Character and Progression According to the Location of Coronary Atherosclerotic Plaque. The American Journal of Cardiology. 2021;158:15-22.
28. Boogers MJ, Schuijf JD, Kitslaar PH, van Werkhoven JM, de Graaf FR, Boersma E, et al. Automated quantification of stenosis severity on 64-slice CT: a comparison with quantitative coronary angiography. JACC Cardiovasc Imaging. 2010;3(7):699-709.
29. Williams MC, Golay SK, Hunter A, Weir-McCall JR, Mlynska L, Dweck MR, et al. Observer variability in the assessment of CT coronary angiography and coronary artery calcium score: substudy of the Scottish COmputed Tomography of the HEART (SCOT-HEART) trial. Open Heart. 2015;2(1):e000234.

6 Comparison of left ventricular mass and wall thickness between cardiac computed tomography angiography and cardiac magnetic resonance imaging using machine learning algorithms

Finn Y van Driest
Rob J van der Geest
Sharif K Omara
Alexander Broersen
Jouke Dijkstra
J Wouter Jukema
Arthur J H A Scholte

Abstract

Introduction: Cardiac magnetic resonance imaging (MRI) is the gold standard in the assessment of left ventricle (LV) mass and wall thickness. In recent years, cardiac computed tomography angiography (CCTA) has gained widespread usage as an imaging modality. Despite this, limited previous investigations have specifically addressed the potential of CCTA as an alternative modality for quantitative LV assessment.

The aim of this study was to compare CCTA derived LV mass and wall thickness with cardiac MRI utilizing machine learning algorithms.

Methods: Fifty-seven participants who underwent both CCTA and cardiac MRI were identified. LV mass and wall thickness was calculated using LV contours which were automatically placed using in-house developed machine learning models. Pearson's correlation coefficients were calculated along with Bland-Altman plots to assess the agreement between the LV mass and wall thickness per region on CCTA and cardiac MRI. Inter-observer correlations were tested using Pearson's correlation coefficient.

Results: Average LV mass and wall thickness for CCTA and cardiac MRI were 127 g ,128 g, 7 and 8mm respectively. Bland-Altman plots demonstrated mean differences and corresponding 95% limits of agreement of -1.26 (25.06;-27.58) and -0.57 (1.78;-2.92), for LV mass and average LV wall thickness, respectively. Mean differences and corresponding 95% limits of agreement for wall thickness per region were -0.75 (1.34;-2.83), -0.58 (2.14;-3.30) and -0.29 (3.21;-3.79) for the basal, mid, and apical regions, respectively. Inter-observer correlations were excellent.

Conclusion: Quantitative assessment of LV mass and wall thickness on CCTA using machine learning algorithms seems feasible and shows good agreement with cardiac MRI.

Abbreviations

AI: Artificial Intelligence
CCTA: Cardiac computed tomography angiography
DICOM: Digital Imaging and Communications in Medicine
ECG: Electrocardiogram
FOV: Field of view
HU: Hounsfield units
LV: Left ventricle
MRI: Magnetic resonance imaging
RV: Right ventricle
TE: Echo time
TR: Repetition time

1. Introduction

Increased left ventricle (LV) mass and wall thickness causing LV hypertrophy are both independent risk factors for cardiovascular mortality and morbidity irrespective of the aetiology (1). Cardiac magnetic resonance imaging (MRI) is still considered to be the gold standard for LV mass and wall thickness measurements (2). However, over the years cardiac computed tomography angiography (CCTA) has become a widely used imaging modality for the assessment of coronary arteries and its diagnostic accuracy has greatly increased in the last decade (3). Still, only a few prior studies have been performed about the use of CCTA for LV mass and wall thickness measurements and only a minor number have compared the measurements to MRI (4-10). Nasser Alnasser et al. have written an extensive review about the use of artificial intelligence (AI) in (cardiac) structure segmentation (11) however, to the best of our knowledge no prior study has incorporated the use of machine-learning-based LV segmentation into the comparison of CCTA and MRI derived LV mass and wall thickness measurements. Use of CCTA for LV mass and wall thickness measurements may be especially useful for patients with contraindications for cardiac MRI such as pacemakers, claustrophobia, or clinical conditions that prohibit long MRI examinations (9). Furthermore, CCTA has been proven to be more readily available, cheaper and faster as compared to MRI (12, 13)

Quantification of LV mass and wall thickness requires the definition of LV endo- and epicardial contours in multiple slices covering the complete LV. Manual segmentation of the LV myocardium is time consuming both for CCTA and cardiac MRI (14, 15). Recently, machine learning algorithms have been developed for both CCTA and cardiac MRI and allow for automatic LV segmentation substantially decreasing the time needed for LV quantification (14, 16, 17). The aim of this study was to compare LV mass and LV wall thickness derived from CCTA and cardiac MRI whilst using machine learning based LV segmentation.

2. Materials and methods

2.1 Patients

For this study 130 participants who underwent both CCTA and cardiac MRI between October 2009 and November 2021 were identified. Participants with a maximum period of more than 6 months between CCTA and cardiac MRI (n = 59), no short-axis cine magnetic resonance (MR) image stack (n = 9), severe motion artifacts on MRI (n = 1), CCTA without contrast (n = 3) and corrupt CCTA digital imaging and communications in medicine (DICOM) files (n = 1) were excluded. A total of 57 participants were selected for the current analysis. Among them, thirteen exhibited LV hypertrophy. Patient characteristics and indications for CCTA and cardiac MRI are described in Table 1. Figure 1 depicts a detailed flowchart of the patient selection. All data were analysed retrospectively. The local ethics

committee of the Leiden University Medical Centre approved this retrospective analysis of clinical data and waived the need for informed consent.

Table 1. Patient characteristics. CCTA: Cardiac computed tomography angiography. VT: Ventricular tachycardia. LV: Left ventricle

Patient characteristics	N = 57
Male / Female	43 (75%) / 14 (25%)
Age (years)	60 ± 12.2
Hypertension	24 (42%)
Hyperlipidaemia	12 (21%)
Diabetes mellitus	3 (5%)
Smoking	2 (4%)
LV hypertrophy*	13 (23%)
CCTA indication	
Chest pain	33 (58%)
Coronary anatomy for workup to VT ablation	22 (39%)
Aortic aneurysm	1 (2%)
Bicuspid aortic valve	1 (2%)
Cardiac MRI indication	
Cardiomyopathy	43 (75%)
Myocarditis	4 (7%)
Cardiac ischemia	3 (5%)
Sarcoidosis with cardiac involvement	3 (5%)
Aortic aneurysm	2 (4%)
Amyloidosis	1 (2%)
Bicuspid aortic valve	1 (2%)

*An end-diastolic LV wall thickness of more than 15mm as measured with 2D echocardiography or cardiac MRI anywhere in the left ventricle (32).

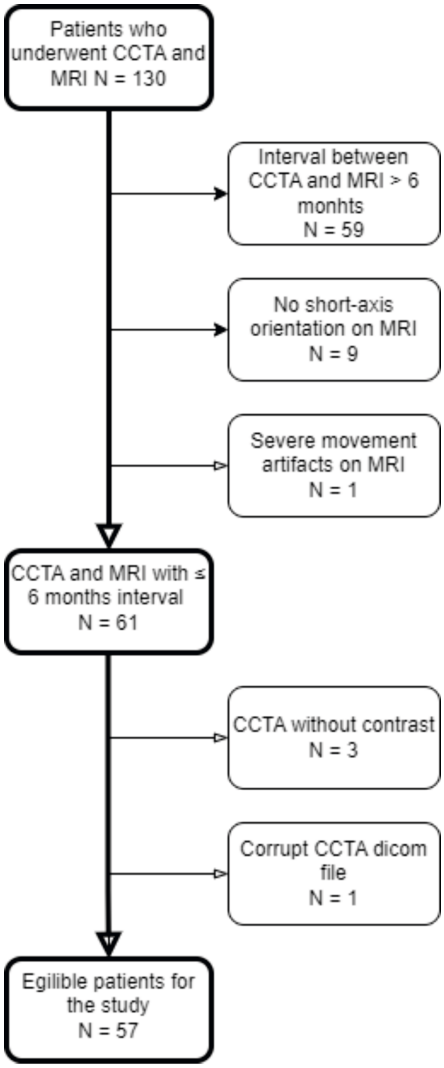

Figure 1. Flowchart demonstrating patient selection. Scans with an inter-scan interval of more than 6 months between MRI and CCTA were excluded. CCTA, cardiac computed tomography angiography. DICOM, digital imaging and communications in medicine. MRI, magnetic resonance imaging.

2.2 CCTA Data acquisition

CCTA was performed using a 320-row volumetric scanner (Aquilion ONE , Canon Medical Systems, Aquilion ONE PRISM Edition, Canon Medical Systems and Aquilion ONE Genesis Edition, Canon Medical Systems, Otawara, Japan). A peak tube voltage of 100-135 kV with a tube current of 140-580mA was used. Detector collimation, gantry rotation time and temporal resolution were 320 x 0.5mm, 275ms and 137ms, for the Aquilon ONE Genesis Edition and 320 x 0.5mm, 350ms and 175ms, for the Aquilon ONE (PRISM Edition)

respectively. The antecubital vein was used for administration of 50–90 mL of contrast agent (Iomeron 400, Bracco, Milan, Italy) followed by a 1:1 mixture of 20 mL contrast and saline and finally 25 mL of saline. Peak tube voltage, tube current and amount of contrast agent varied based on patient size (18). After contrast administration CCTA was performed the next heartbeat when a threshold of 300 Hounsfield units was reached in the descending aorta. Subsequently, 70-80% of the RR interval was scanned using prospective electrocardiogram (ECG) triggering.

2.3 MRI Data acquisition

Cardiac MRI was performed using a 1.5-T Gyroscan ACS-NT/Intera MR system (Philips Medical Systems, Best, The Netherlands) or a 3.0-T Ingenia MR system (Philips Medical Systems, Best, The Netherlands) using retrospective ECG gating. Imaging parameters were as follows for the 1.5-T Gyroscan ACS-NT/Intera MR system: field of view (FOV) 400 × 320 mm^2; matrix, 256 × 206 pixels; slice thickness, 10 mm with no slice gap; flip angle (α), 35°; echo time (TE), 1.67 ms; and repetition time (TR), 3.3 ms. For the 3.0-T Ingenia MR system typical parameters were: FOV 400 × 350 mm; matrix, 232 × 192 pixels; slice thickness, 8 mm with no slice gap; α, 45°; TE, 1.5 ms and TR, 3.0 ms. The heart was imaged in 1 or 2 breath-holds with short-axis slices at various levels dependent on the heart size.

2.4 Image processing

Images were transferred to a workstation for quantitative analysis. In-house developed MASS software (Leiden University Medical Centre) was used for short-axis reformatting in the CCTA scans and for LV contour placement in the CCTA and MRI scans. The software has been validated and supported for clinical purposes. A study by Kawel provides robust evidence of its efficacy and reliability (19).

CCTA and MRI data were analysed independently and no visual reference to the other could be made at any time. Also, the observer was blinded to the results of LV mass and LV wall thickness of each scan. Quantitative analysis of both modalities as well as short-axis reformatting in the CCTA was done automatically by using machine learning models. Contours were manually corrected if needed. The AI model used for MRI and CCTA based LV segmentation used a deep learning-based approach. Specifically, a convolutional neural network architecture, known as the U-Net, was employed for this purpose. The AI model was trained on a large dataset of cardiac MRI and CCTA scans, where both the raw images and manually annotated LV contours are provided as input. During the training process, the model learns to map the input images to the corresponding LV contours, optimizing its parameters to minimize the difference between the predicted and ground truth segmentations. Finally, the performance of the AI model was evaluated on an independent testing dataset, which consists of additional cardiac MRI and CCTA scans. The model's predictions on the testing set were compared against manual ground truth annotations to assess its performance in real-world scenarios. Training and use of the

machine learning models is discussed in more detail for both CCTA and cardiac MRI in two separate papers (16, 17).

First, CCTA images were automatically reformatted into a short-axis orientation covering the complete LV with a slice thickness of 4 mm. Cardiac MRI images with a slice thickness of 8 or 10 mm were already available in short axis hence, no further reformatting was needed. Once short-axis slice stacks were created a reference point was placed in a mid-slice at the site of the inferior attachment of the right ventricle (RV) to LV, both for CCTA and cardiac MRI. The segment numbering within a specific level depends on the location of the reference point. Hence, this allows for anatomical alignment of CCTA and cardiac MRI. Finally, LV epicardial and endocardial contours were automatically detected first in the CCTA and hereafter in the cardiac MRI for each patient. The 75% phase was chosen for LV segmentation on both the CCTA and cardiac MRI as this phase is most ideal for LV mass and wall thickness calculation (20). Figure 2 depicts the results of LV segmentation for both CCTA and cardiac MRI.

We have opted not to include LV volume as the basis for its calculation (as is with LV mass) is based on endo- and epicardial LV contours using MASS software. As the main goal of this study was to evaluate the matter of agreement between CCTA and MRI derived LV contours we chose LV mass as a derivative of these contours. Therefore, including a comparison of LV volume between imaging modalities will not provide additional meaningful insights beyond what is already captured in the LV mass calculation process.

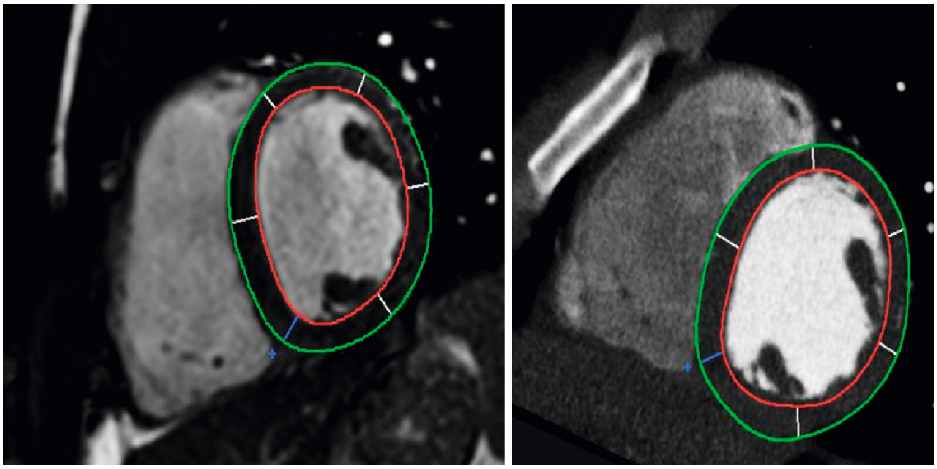

Figure 2. Example of LV segmentation of a middle region slice of the same patient for both cardiac MRI (left panel) and CCTA (right panel). The red lines represent the endocardial contours. The green lines represent the epicardial contours. The reference point is marked by the small blue cross. Middle region wall thickness for this patient was 8 mm on MRI and 6 mm on CCTA.

2.5 LV mass and wall thickness calculation

Using the LV contours, LV mass and wall thickness were calculated automatically using the aforementioned software. Average LV wall thickness as well as segmental wall thickness, using the standard 16-segment model were derived (21). Furthermore, segments were combined to provide wall thickness per LV region consisting of the basal, mid and apical regions (21) which is depicted in Figure 3. LV wall thickness for the entire LV and per region were calculated using the following formulas.

$$LV\,wall\,thickness = \frac{\text{segment } 1 + \text{segment } 2 + \ldots + \text{segment}16}{16}$$

$$LV\,wall\,thickness\,basal = \frac{\text{segment } 1 + \text{segment } 2 + \text{segment } 3 + \text{segment } 4 + \text{segment } 5 + \text{segment } 6}{6}$$

$$LV\,wall\,thickness\,mid = \frac{\text{segment } 7 + \text{segment } 8 + \text{segment } 9 + \text{segment } 10 + \text{segment } 11 + \text{segment } 12}{6}$$

$$LV\,wall\,thickness\,apical = \frac{\text{segment } 13 + \text{segment } 14 + \text{segment } 15 + \text{segment } 16}{4}$$

To assess inter-observer reproducibility a second independent observer performed quantitative analysis in a randomly selected cohort of twenty subjects. Since manual adjustments to the automatically detected contours was occasionally required, the results between observers may vary. Correlations of LV mass and LV wall thickness for both CCTA and cardiac MRI between both observers were subsequently tested using Pearson's correlation coefficient.

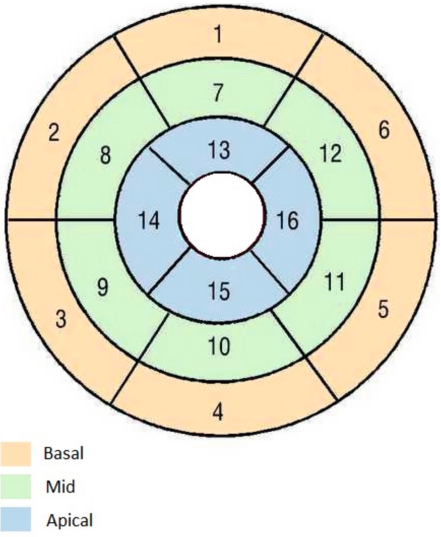

Figure 3. Standard 16-segment model depicting how different segments make up 3 different major regions; basal, mid and apical.

2.6 Statistical analysis

The agreement between LV mass and wall thickness derived from CCTA and cardiac MRI was assessed using Bland-Altman plots and Pearson's correlation coefficient. Inter-observer correlations were tested using Pearson's correlation coefficient. SPSS software version 25, SPSS IBM Corp, Armonk, New York) was used for all statistical analysis.

3. Theory

Performing a comparison of CCTA and LV mass and wall thickness using machine learning algorithms serves both a practical and time-saving purpose. For instance, patients with contraindications for cardiac MRI, such as those with pacemakers, claustrophobia, or conditions prohibiting prolonged MRI examinations could potentially benefit from CCTA as prior mentioned factors play no role in CCTA acquisition (9). Furthermore, the increased availability, cost-effectiveness and speed of CCTA compared to cardiac MRI make it an attractive alternative for routine clinical use (12, 13). Lastly, LV segmentation is time consuming and machine learning algorithms for automatic LV segmentation have already been proved to speed up this process (14, 16, 17). An important consideration is whether use of these algorithms does not compromise the accuracy of LV segmentation as compared to the gold standard of cardiac MRI.

4. Results

CCTA -and cardiac MRI images from 57 participants were used in the current analysis hence a total of a 114 scans were analysed. Table 1 lists a detailed description of patient characteristics. Mean LV mass derived from CCTA and cardiac MRI including the standard deviation were 127 ± 31.6 and 128 ± 31.0 g, respectively. Mean wall thickness derived from CCTA and cardiac MRI including the standard deviation were 7 ± 1.5 mm and 8 ± 1.3 mm, respectively. Correlation between CCTA and cardiac MRI derived LV mass was very strong ($r = 0.908$, $p < 0.001$). Furthermore, corresponding mean differences and 95% limits of agreement for LV mass as demonstrated by the Bland-Altman plot were -1.26 (25.06;-27.58). LV wall thickness correlation between CCTA and cardiac MRI was strong ($r = 0.644$, $p < 0.001$) for average wall thickness and ($r = 0.662$, $p < 0.001$), ($r = 0.668$, $p < 0.001$) for the basal and mid regions, respectively. Average wall thickness in the apical regions demonstrated a moderate correlation ($r = 0.524$, $P < 0.001$). Corresponding mean differences and 95% limits of agreement were -0.57 (1.78;-2.92), -0.75 (1.34;-2.83), -0.58 (2.14;-3.30) and -0.29 (3.21;-3.79) for average wall thickness, basal, mid and apical regions, respectively. The average value for the thickest segments on MRI and CCTA including the standard deviation were 11 ± 1.8 and 10 ± 2.5 mm respectively and demonstrated a strong correlation ($r=0.687$ $p<0.001$). Corresponding mean differences and 95% limits of agreement were -1.06 (2.47;-4.60). Relevant charts for LV mass and wall thickness

correlations between CCTA and MRI as well as limits of agreement including mean difference are depicted in figure 4, figure 5, figure 6 and figure 7. All results are listed numerically in Table 2 as well as LV mass and LV wall thickness values according to clinical diagnosis in Table 3.

Mean differences per segment were assessed using the standard 16-segment model. Results are depicted in figure 8.

Interobserver correlations and intraclass correlation coefficients for CCTA derived LV mass, MRI derived LV mass, CCTA derived average wall thickness and MRI derived average wall thickness were excellent yielding Pearson's correlations coefficients of ($r = 0.994$, $p < 0.001$), ($r = 0.970$, $p < 0.001$), ($r = 0.971$, $p < 0.001$), ($r = 0.956$, $p < 0.001$), ($r = 0.965$, $p < 0.001$) ($r = 0.877$, $p < 0.001$), ($r = 0.825$, $p < 0.001$) and ($r = 0.820$, $p < 0.001$) respectively.

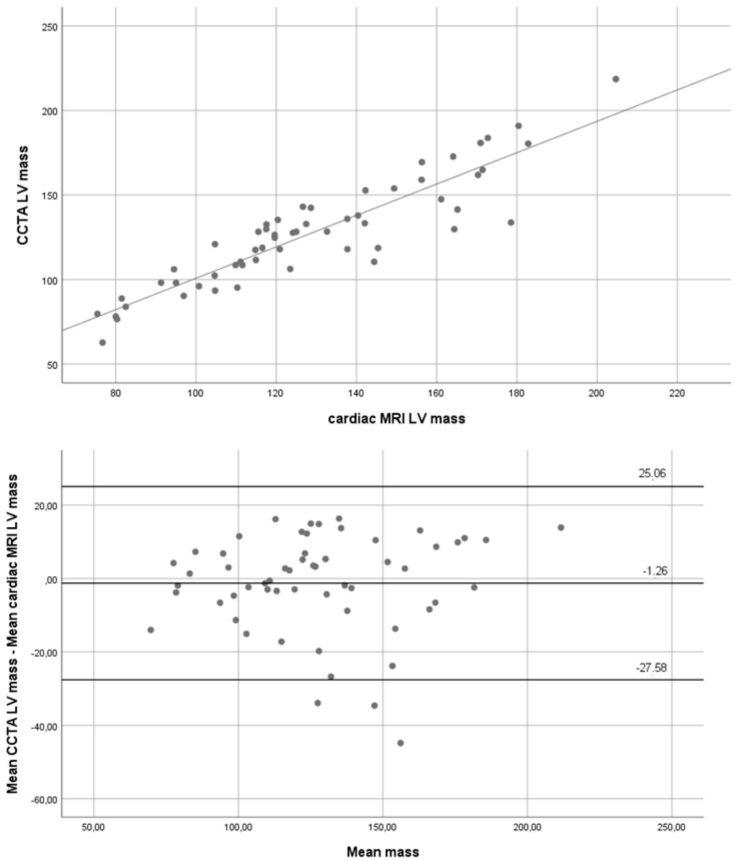

Figure 4. Correlations and mean differences with corresponding 95% limits of agreement for mean LV mass in grams. CCTA: Cardiac computed tomography angiography. MRI: Magnetic resonance imaging. LV: Left ventricle.

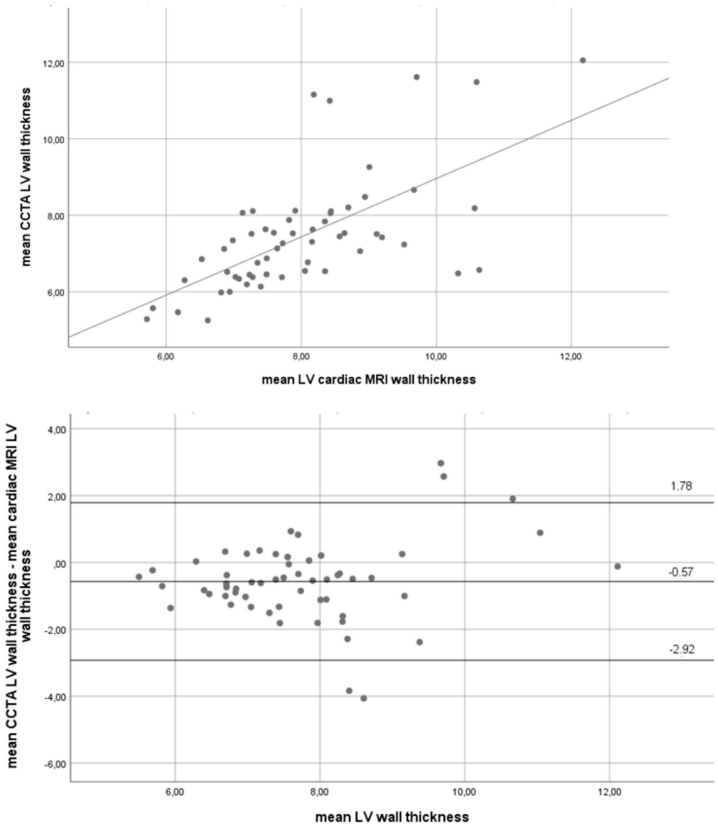

Figure 5. Correlations and mean differences with corresponding 95% limits of agreement for mean LV wall thickness in millimeters. CCTA: Cardiac computed tomography angiography. MRI: Magnetic resonance imaging. LV: Left ventricle.

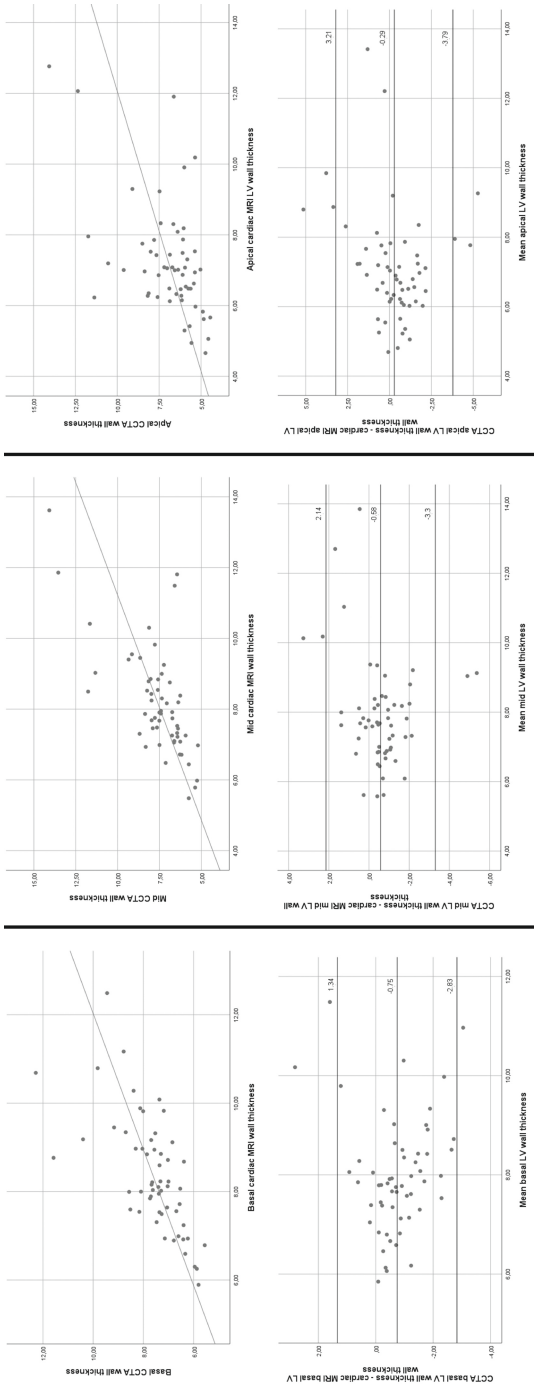

Figure 6. Correlations and mean differences with corresponding 95% limits of agreement for mean LV wall thickness in millimeters according to regions. CCTA: Cardiac computed tomography angiography. MRI: Magnetic resonance imaging. LV: Left ventricle.

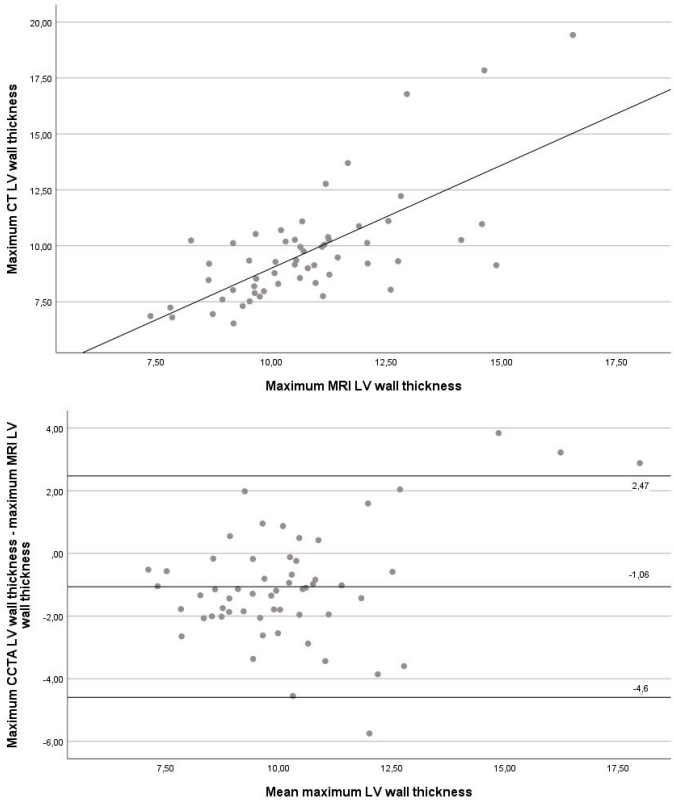

Figure 7. Correlations and mean differences with corresponding 95% limits of agreement for LV wall thickness differences corresponding to the thickest segments in millimeters. CCTA: Cardiac computed tomography angiography. MRI: Magnetic resonance imaging.

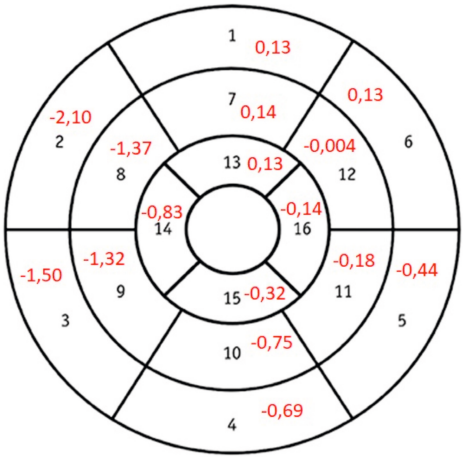

Figure 8. Mean differences in millimeters between CCTA and MRI wall thickness per segment are represented by the red numbers.

Table 2

	Pearson's correlation coefficient R	Mean differences and 95% limits of agreement
LV mass	0.908 (p<0.001)	-1.26 (25.06;-27.58)
LV wall thickness entire LV	0.644 (p<0.001)	-0.57 (1.78;-2.92)
LV wall thickness basal region	0.662 (p<0.001)	-0.75 (1.34;-2.83)
LV wall thickness mid region	0.668 (p<0.001)	-0.58 (2.14;-3.30)
LV wall thickness apical region	0.524 (p<0.001)	-0.29 (3.21;-3.79)
Maximum LV wall thickness	0.687 (p<0.001)	-1.06 (2.47;-4.60).

Correlations and limits of agreement between CCTA and MRI. LV: Left ventricle.

Table 3

Diagnosis	Average CCTA LV mass	Average MRI LV mass	Average CCTA LV wall thickness	Average MRI LV wall thickness
Diabetes mellitus (N=3)	130 grams	123 grams	9 mm	8 mm
Hypertension (N=24)	135 grams	137 grams	8 mm	9 mm
Hyperlipidaemia (N=12)	142 grams	140 grams	9 mm	9mm

Average LV mass and wall thickness on CCTA and MRI according to comorbidity. CCTA: Cardiac computed tomography angiography. LV: Left ventricle. MRI: Magnetic resonance imaging.

5. Discussion

This study assessed the comparison of LV mass and LV wall thickness between CCTA and cardiac MRI calculated from LV epi- and endocardial contours whilst using machine learning algorithms for automatic placement of these contours. Results demonstrate that CCTA shows good correlation with MRI with regard to LV mass and LV wall thickness. Also, Bland-Altman plots show narrow limits of agreement and minimal bias. As a result, (CCTA) can serve not only in the evaluation of coronary stenoses but also in the assessment of LV mass and wall thickness. This capability positions CCTA as a viable alternative to cardiac MRI.

Koo et al. performed an analysis in which they evaluated the accuracy of a deep learning-based algorithm for the segmentation of the LV on CCTA. However, instead of comparing this to MRI the results were compared to manual segmentations. It was demonstrated that deep learning-based segmentation results were comparable to those provided by manual segmentation with a high Dice index. They also concluded that based on visual analysis, automated LV segmentation using deep learning is superior to semi-automatic segmentation performed by an expert reader. Unfortunately, no statistical evidence was given to back up this last claim (14).

In a comprehensive review by Kawel et al. reference values of LV mass were given for cardiac MRI. An average LV mass of 121 grams was found for men and 83 grams for women. As the goal of our study was to assess the agreement of LV mass and LV wall thickness between CCTA and MRI men and women were not assessed separately. Still, our average LV mass value on cardiac MRI of 128 g closely matches the value found by Kawel et al. Given the predominant representation of men in our study (75 vs. 25% women), it is noteworthy that this gender distribution imbalance could contribute to an elevated average LV mass value, given the generally higher LV mass observed in men compared to women (22). It is also important to realize that due to the retrospective nature of this study the cohort consists of clinical participants, hence we cannot exclude the possibility of this cohort having a higher than average LV mass as compared to a sample of the general population which was used by Kawel et al. Furthermore, in another study by Kawel et al. the normal values for LV wall thickness on cardiac MRI were assessed per segment according to the standard 16-segment model. An average of 6 and 7 mm were found respectively for women and men when combining all regions. This closely matches our result of 8 mm for average LV wall thickness. Again, the result in our study could be slightly higher due to the fact that we have included vastly more men than women (19, 21) and that due to the retrospective nature of this study the cohort consists of clinical participants which may have a higher average LV mass as compared to the general population.

A study by Kara et al. also compared myocardial LV mass between CCTA and MRI using manual LV contour tracing for both modalities. It was also found that LV mass derived from CCTA correlated strongly with cardiac MRI using Pearson's correlation coefficient ($r = 0.884$, $p < 0.001$), which is comparable to our study. Furthermore, Bland-Altman plots by Kara et al. demonstrated a mean difference of 19.50 g with corresponding 95% upper and lower limits of agreement of 66.05 and -27.05 g, respectively (9). The difference between the upper limit and the lower limit in our study for LV mass as well as the mean difference is much lower as compared to Kara et al. This could be attributed to the fact that Kara et al. used a 64 slice computed tomography (CT) scanner whereas in our study this was a 320 slice CT scanner greatly increasing image quality (23). Also, no machine learning model was used for LV segmentation in the study by Kara et al.

Wang et al. similarly used automatic software for LV wall thickness comparison between CCTA and cardiac MRI. The methodology of our study is comparable to the study by Wang et al. as the borders of the endocardium and epicardium were automatically segmented. However, MRI contours were segmented manually. A Pearson's correlation coefficient for average LV wall thickness between CCTA and cardiac MRI of $r = 0.698$ ($p < 0.01$) was found by Wang et al. This is slightly higher compared to ours $r = 0.644$ ($p < 0.01$). However, Bland-Altman plots obtained by Wang et al. revealed a mean difference of 0.6 mm with 95% upper and lower limits of agreement of 4.0 mm and -2.7 mm, respectively (8). Although the mean difference is equivalent to our study, their observed difference between the upper and lower limits is considerably more than in our study. Again, this could be partly

explained due to the use of different scanner settings. Unfortunately, the slice capacity of the scanner used was not provided by Wang et al.

Given the Bland-Altman plots for mass differences between CCTA and MRI in our study it is important to note how these upper and lower limits would affect the diagnosis of LV hypertrophy. For instance, Levy et al. investigated the cut-off values for LV mass that define LV hypertrophy. It was found that a LV mass of 294 g or more for men and 198 g or more for women would implicate LV hypertrophy. Our study found mean LV mass of 127 and 128 g for CCTA and cardiac MRI respectively and 95% limits of agreement for differences between CCTA and cardiac MRI of 25.06;-27.58 implicate that diagnosing LV hypertrophy would still be possible as potential differences between CCTA and cardiac MRI measurements are well below that of LV hypertrophy (24).

Interestingly, when observing the mean differences between CCTA and cardiac MRI derived wall thickness per segment in Figure 8 it can be observed that the mean differences are greater in septal regions compared to other regions. This could be due to the fact that on cardiac MRI it is easier to differentiate between the septum wall and the RV as compared to CCTA as with the latter there is less contrast in the RV as compared to the LV (25). Furthermore, it is observed that correlation coefficient and limits of agreement considering wall thickness on CCTA and cardiac MRI are less strong for the apical region compared to other regions. This is mainly due to the fact that smaller contours which are more present apically are more prone to bias as was also described by Mitchell et al (26).

5.1 Limitations

This study has several limitations, which are innate to its retrospective design and novel nature. Firstly, it was conducted at a single centre, which may limit the generalizability of our findings to broader patient populations and clinical settings. Consequently the sample size in our study was limited, which may affect the statistical power and precision of our results. Secondly, the absence of clinical endpoints in our study restricts our ability to directly assess the impact of CCTA compared to cardiac MRI on patient outcomes. Thirdly, it was not possible to use similar cardiac gating parameters for the CCTA and cardiac MRI. Hence, differences in LV mass and LV wall thickness between CCTA and cardiac MRI may be attributed due to differences in the cardiac timing of the image acquisition. Still for both imaging modalities the phase on 75% of the RR interval was used for contour placement and subsequent LV mass and wall thickness comparison. However, differences in heartbeat may still have negatively impacted equal cardiac timing of CCTA and cardiac MRI. It is worth noting that different scanners with different tesla strengths (1.5 and 3.0 T) were used for MRI image acquisition in our study. Although using a 3.0 T scanner can substantially decrease scanning time compared to a 1.5 T scanner it has been demonstrated that there is no difference regarding LV mass and wall thickness measurements. Therefore use of different MRI scanners in this study is unlikely to have influenced the LV contour placement accuracy (27). Fourthly, images derived from CCTA

and MRI have a different slice thickness. We cannot entirely exclude the possibility that this has influenced the accuracy of LV contour placement. However, multiple studies have demonstrated that the accuracy of LV segmentation is not affected by slice thickness both for CCTA and MRI (28, 29). Lastly, In our study, we deliberately chose not to include papillary muscles and trabeculae in the LV mass assessment as our primary objective was to conduct a uniform comparison between cardiac MRI and CCTA for LV mass and wall thickness quantification. Furthermore, including papillary muscles and trabeculae in the assessment is time consuming and may introduce variability, potentially confounding the comparison between the two imaging modalities (30). Still, not including papillary muscles and trabeculae may have introduced bias as this can lead to lower LV volumes as compared to the reference values, especially in patients with LV hypertrophy (30).

6. Conclusions

Utilizing CCTA for assessment of LV mass and wall thickness whilst using a machine learning model for LV segmentation shows good agreement with cardiac MRI. Consequently, CCTA may offer a reliable alternative for individuals with contraindications to cardiac MRI in the context of LV mass and wall thickness assessment. Notably, CCTA offers advantages in terms of greater accessibility, cost-effectiveness, and faster imaging acquisition compared to MRI (12, 13), albeit with the caveat of increased radiation exposure (31). Despite being conducted at a single center and without clinical endpoints, our findings offer important preliminary evidence that warrants further investigation and validation in larger, multicenter studies with clinical outcomes.

References

1. Haider AW, Larson MG, Benjamin EJ, Levy D. Increased left ventricular mass and hypertrophy are associated with increased risk for sudden death. J Am Coll Cardiol. 1998;32(5):1454-9.
2. Fulton N, Rajiah P. Utility of magnetic resonance imaging in the evaluation of left ventricular thickening. Insights Imaging. 2017;8(2):279-93.
3. Opincariu D, Benedek T, Chitu M, Rat N, Benedek I. From CT to artificial intelligence for complex assessment of plaque-associated risk. Int J Cardiovasc Imaging. 2020;36(12):2403-27.
4. Budoff MJ, Ahmadi N, Sarraf G, Gao Y, Chow D, Flores F, et al. Determination of left ventricular mass on cardiac computed tomographic angiography. Acad Radiol. 2009;16(6):726-32.
5. Klein R, Ametepe ES, Yam Y, Dwivedi G, Chow BJ. Cardiac CT assessment of left ventricular mass in mid-diastasis and its prognostic value. Eur Heart J Cardiovasc Imaging. 2017;18(1):95-102.
6. Khatri PJ, Tandon V, Chen L, Yam Y, Chow BJ. Can left ventricular end-diastolic volumes be estimated with prospective ECG-gated CT coronary angiography? Eur J Radiol. 2012;81(2):226-9.
7. Juneau D, Erthal F, Clarkin O, Alzahrani A, Alenazy A, Hossain A, et al. Mid-diastolic left ventricular volume and mass: Normal values for coronary computed tomography angiography. J Cardiovasc Comput Tomogr. 2017;11(2):135-40.
8. Wang R, Meinel FG, Schoepf UJ, Canstein C, Spearman JV, De Cecco CN. Performance of Automated Software in the Assessment of Segmental Left Ventricular Function in Cardiac CT: Comparison with Cardiac Magnetic Resonance. Eur Radiol. 2015;25(12):3560-6.
9. Kara B, Nayman A, Guler I, Gul EE, Koplay M, Paksoy Y. Quantitative Assessment of Left Ventricular Function and Myocardial Mass: A Comparison of Coronary CT Angiography with Cardiac MRI and Echocardiography. Pol J Radiol. 2016;81:95-102.
10. Andreini D, Conte E, Mushtaq S, Melotti E, Gigante C, Mancini ME, et al. Comprehensive Evaluation of Left Ventricle Dysfunction by a New Computed Tomography Scanner: The E-PLURIBUS Study. JACC Cardiovasc Imaging. 2023;16(2):175-88.
11. Alnasser TN, Abdulaal L, Maiter A, Sharkey M, Dwivedi K, Salehi M, et al. Advancements in cardiac structures segmentation: a comprehensive systematic review of deep learning in CT imaging. Front Cardiovasc Med. 2024;11:1323461.
12. Papanicolas I, Woskie LR, Jha AK. Health Care Spending in the United States and Other High-Income Countries. JAMA. 2018;319(10):1024-39.
13. Tidwell AS, Jones JC. Advanced imaging concepts: a pictorial glossary of CT and MRI technology. Clin Tech Small Anim Pract. 1999;14(2):65-111.
14. Koo HJ, Lee JG, Ko JY, Lee G, Kang JW, Kim YH, et al. Automated Segmentation of Left Ventricular Myocardium on Cardiac Computed Tomography Using Deep Learning. Korean J Radiol. 2020;21(6):660-9.
15. Lu YL, Connelly KA, Dick AJ, Wright GA, Radau PE. Automatic functional analysis of left ventricle in cardiac cine MRI. Quant Imaging Med Surg. 2013;3(4):200-9.
16. van Driest FY, Bijns CM, van der Geest RJ, Broersen A, Dijkstra J, Jukema JW, et al. Correlation between quantification of myocardial area at risk and ischemic burden at cardiac computed tomography. Eur J Radiol Open. 2022;9:100417.
17. Alabed S, Alandejani F, Dwivedi K, Karunasaagarar K, Sharkey M, Garg P, et al. Validation of Artificial Intelligence Cardiac MRI Measurements: Relationship to Heart Catheterization and Mortality Prediction. Radiology. 2022;304(3):E56.
18. Abbara S, Blanke P, Maroules CD, Cheezum M, Choi AD, Han BK, et al. SCCT guidelines for the performance and acquisition of coronary computed tomographic angiography: A report of the society of Cardiovascular Computed Tomography Guidelines Committee: Endorsed by the North American Society for Cardiovascular Imaging (NASCI). J Cardiovasc Comput Tomogr. 2016;10(6):435-49.
19. Kawel N, Turkbey EB, Carr JJ, Eng J, Gomes AS, Hundley WG, et al. Normal left ventricular myocardial thickness for middle-aged and older subjects with steady-state free precession cardiac magnetic resonance: the multi-ethnic study of atherosclerosis. Circ Cardiovasc Imaging. 2012;5(4):500-8.
20. Isma'eel H, Hamirani YS, Mehrinfar R, Mao S, Ahmadi N, Larijani V, et al. Optimal phase for coronary interpretations and correlation of ejection fraction using late-diastole and end-diastole imaging in cardiac computed tomography angiography: implications for prospective triggering. Int J Cardiovasc Imaging. 2009;25(7):739-49.

21. Cerqueira MD, Weissman NJ, Dilsizian V, Jacobs AK, Kaul S, Laskey WK, et al. Standardized myocardial segmentation and nomenclature for tomographic imaging of the heart. A statement for healthcare professionals from the Cardiac Imaging Committee of the Council on Clinical Cardiology of the American Heart Association. Circulation. 2002;105(4):539-42.
22. Kawel-Boehm N, Hetzel SJ, Ambale-Venkatesh B, Captur G, Francois CJ, Jerosch-Herold M, et al. Reference ranges ("normal values") for cardiovascular magnetic resonance (CMR) in adults and children: 2020 update. J Cardiovasc Magn Reson. 2020;22(1):87.
23. Khan A, Khosa F, Nasir K, Yassin A, Clouse ME. Comparison of radiation dose and image quality: 320-MDCT versus 64-MDCT coronary angiography. AJR Am J Roentgenol. 2011;197(1):163-8.
24. Levy D, Savage DD, Garrison RJ, Anderson KM, Kannel WB, Castelli WP. Echocardiographic criteria for left ventricular hypertrophy: the Framingham Heart Study. Am J Cardiol. 1987;59(9):956-60.
25. Lee H, Kim SY, Gebregziabher M, Hanna EL, Schoepf UJ. Impact of ventricular contrast medium attenuation on the accuracy of left and right ventricular function analysis at cardiac multi detector-row CT compared with cardiac MRI. Acad Radiol. 2012;19(4):395-405.
26. Mitchell SC, Bosch JG, Lelieveldt BP, van der Geest RJ, Reiber JH, Sonka M. 3-D active appearance models: segmentation of cardiac MR and ultrasound images. IEEE Trans Med Imaging. 2002;21(9):1167-78.
27. Gandy SJ, Lambert M, Belch J, Cavin I, Crowe E, Littleford R, et al. 3T MRI investigation of cardiac left ventricular structure and function in a UK population: The tayside screening for the prevention of cardiac events (TASCFORCE) study. Journal of Magnetic Resonance Imaging. 2016;44(5):1186-96.
28. DOĞAN H, VELDKAMP WJH, DIBBETS-SCHNEIDER P, SPIJKERBOER AM, MERTENS BJA, KROFT LJM, et al. Effects of heart rate, filling and slice thickness on the accuracy of left ventricular volume measurements in a dynamic cardiac phantom using ECG-gated MDCT. The British Journal of Radiology. 2008;81(967):577-82.
29. Higgins CB, de Roos A. MRI and CT of the Cardiovascular System: Lippincott Williams & Wilkins; 2006.
30. Yang C, Xu H, Qiao S, Jia R, Jin Z, Yuan J. Papillary and Trabecular Muscles Have Substantial Impact on Quantification of Left Ventricle in Patients with Hypertrophic Obstructive Cardiomyopathy. Diagnostics (Basel). 2022;12(8).
31. Hausleiter J, Meyer T, Hermann F, Hadamitzky M, Krebs M, Gerber TC, et al. Estimated Radiation Dose Associated With Cardiac CT Angiography. JAMA. 2009;301(5):500-7.
32. Ommen SR, Mital S, Burke MA, Day SM, Deswal A, Elliott P, et al. 2020 AHA/ACC Guideline for the Diagnosis and Treatment of Patients With Hypertrophic Cardiomyopathy: Executive Summary: A Report of the American College of Cardiology/American Heart Association Joint Committee on Clinical Practice Guidelines. Circulation. 2020;142(25):e533-e57.

7 Summary, conclusions and future perspectives

Summary

Chapter1 includes the general introduction and thesis outline. CCTA in combination with CTP allows for quantitative, qualitative and functional assessment of CAD. Furthermore, quantification of myocardial ischemia on CTP and using a Voronoi algorithm for myocardial segmentation allows for quantitative correlation of myocardial ischemia to the corresponding coronary stenosis which is vital for revascularization. Following the widespread use of CCTA use of serial CCTA has emerged in recent years allowing for the assessment of changes in plaque burden and plaque morphology. Technological advancements have enabled the use of automatic alignment in the comparison of baseline and follow-up scans whilst also allowing for quantitative assessment of plaque changes. Specific advancements in CCTA image quality have enabled CCTA to be used for LV dimension assessment, a task still mainly performed by cardiac MRI. **Chapter 2** consists of a review article exploring the use of serial CCTA for predicting plaque progression and MACE. The following topics are described. Quantitative baseline plaque features as well as quantitative plaque changes seem to be more predictive of MACE and/or plaque progression as compared to qualitative plaque features. Furthermore, higher epicardial fat volume (EFV) at baseline was associated with the progression or development of coronary artery plaque. Serial CCTA has also been proven useful in the assessment of statin therapy efficacy on plaque progression as it has been revealed that statins slowed the overall progression of coronary atherosclerosis volume and induced an increase in plaque calcification and reduction of high risk plaque features. Certain challenges remain with regard to the clinical use of serial CCTA. For instance, different scanners may be used at baseline and follow-up scans leading to a variability in plaque volume assessment. This highlights the importance of using standardized acquisition protocols for both baseline and follow-up CT scans. Furthermore, no expert consensus is available on the ideal inter-scan interval between baseline and follow-up CT scans but based on recent studies this interval could potentially be set at 1-2 years. **Chapter 3** describes the development of patient specific thresholds for determining plaque progression and/or regression on serial CCTA. Delineation of coronary vessel and lumen contours is necessary for plaque quantification which is vital for CAD assessment on both CCTA and serial CCTA. This delineation process is dependent on scan quality which can be quantified using the contrast to noise ratio (CNR). Consequently, thresholds are necessary to differentiate actual changes in plaque thickness from changes caused by inaccuracies in vessel and lumen wall delineation. A cohort of 50 patients with available CCTA was used in which two different phases from each scan were used for the delineation of 300 coronary vessels and CNR calculation for each vessel. The average CNR value was 13.4 ± 3.6. The average positive and negative differences in measured plaque thickness were 0.7 ± 0.3 and -0.9 ± 0.6 mm, respectively. The inter-observer correlation for CNR values was excellent, with a correlation coefficient of 0.872 ($p < 0.001$). Found plaque differences among these two phase scan sets may be attributed to inaccuracies in plaque delineation as plaque differences between two reconstructed phases from the

same scan from the same patient should always be zero. Subsequently, largest positive and negative plaque differences were plotted against the vessel-specific CNR. Plots revealed a small trend in which larger plaque differences corresponded with a lower CNR. By using linear regression analysis vessel specific and patient specific thresholds could be obtained based on the vessel-specific CNR. **Chapter 4** demonstrates the possibility of full quantification of myocardial perfusion defects as assessed by CTP. Nowadays assessment of CTP is done semi quantitatively by visual analysis. Full quantification of myocardial perfusion defects and subtended myocardial mass seems feasible as it allows for identifying the distribution of myocardial ischemia over the coronary artery lesion(s). Thirty-three patients with a combined CCTA and CTP protocol with good or excellent imaging quality on CTP were analyzed using the Voronoi algorithm. This algorithm allows for dividing tissue in different segments according to which blood vessel is closest to the segment. A total of 64 relevant coronary artery lesions were assessed. Average values for total subtended mass, subtended mass per lesion, perfusion defect mass and perfusion defect mass per lesion were 69, 36, 7 and 3 grams respectively. In 19/33 patients (58%) the total perfusion defect mass could be distributed over the relevant coronary artery lesion(s). **Chapter 5** explores the correlation between the quantified myocardial area at risk and quantified areas of myocardial ischemia. Forty-two patients with a combined CCTA and CTP protocol and at least one stenosis of ≥ 50% on CCTA were selected for analysis. The myocardial area at risk was calculated using a Voronoi-based segmentation algorithm on CCTA and was defined as the sum of all territories related to a ≥ 50% stenosis as a percentage of the total LV mass. The ischemic burden was calculated as the quantified area of myocardial ischemia as a percentage of the total LV mass. LV contours were automatically placed using a machine learning algorithm. A total of 77 coronary lesions with a luminal stenosis of ≥ 50% were assessed. Analysis was done separately for stenosis of ≥ 50% and ≥ 70%. Average myocardial area at risk for stenosis ≥ 50% and ≥ 70% were 59% and 37%, respectively. Average ischemic burden for stenosis ≥ 50% and ≥ 70% were 23% and 24%, respectively. There was a moderate correlation of the ischemic burden versus myocardial area at risk for stenosis of ≥ 50% ($r = 0.564$; $p < 0.01$). A good correlation was found for the ischemic burden versus the area at risk for stenosis of ≥ 70% ($r = 0.708$; $p < 0.01$). **Chapter 6** assesses the use of CCTA for LV mass and wall thickness assessment as compared to the gold standard of cardiac MRI. Fifty-seven patients with available CCTA and MRI with an interscan interval of 6 months maximum were analyzed. Average LV mass and wall thickness for CCTA and cardiac MRI were 127 grams, 128 grams, 7mm and 8 mm, respectively. Bland–Altman plots demonstrated mean differences and corresponding 95% limits of agreement of –1.26 (25.06; –27.58) and –0.57 (1.78; –2.92), for LV mass and average LV wall thickness, respectively. Mean differences and corresponding 95% limits of agreement for wall thickness per region were –0.75 (1.34; –2.83), –0.58 (2.14; –3.30), and –0.29 (3.21; –3.79) for the basal, mid, and apical regions, respectively. Ultimately, use of CCTA for LV dimension assessment is feasible and shows good agreement with cardiac MRI.

General discussion

This thesis explores the evolving role of CCTA in cardiovascular imaging. Hereby focusing on the utilization of serial CCTA on plaque progression and/or regression, quantifying myocardial ischemia on CTP and subsequently correlating this to the myocardial area at risk and lastly using CCTA as an imaging tool for LV morphology evaluation.

Across five original studies, the results support the increasing clinical value of CCTA as a multipurpose imaging tool for both anatomical and functional assessment, especially when aided by advanced computational methods.

A proposed method for the objective assessment of plaque dynamics using patient-specific thresholds on CCTA allows for the direct visualization and quantification of plaque thickness differences, and shows good visual agreement with the plaque localization. Absence of a gold standard may be regarded as a severe limitation however Cao et al demonstrated excellent correspondence using artificially created plaque changes (1).

Adequate detection of plaque changes is highly important as multiple studies have demonstrated that especially quantitative plaque features (contrary to qualitative features) are predictive of plaque progression and MACE (2-5). Furthermore, the capability of subclinical atherosclerosis progression and/or regression detection may be especially beneficial for timely treatment in order to prevent atherosclerosis progression (6).

In two additional studies the utility of CCTA was expanded to the functional domain in terms of ischemia detection using CTP. Primarily it was demonstrated that ischemia may be quantified and subsequently correlated with the subtended mass as is determined by the coronary stenosis. These studies hereby confirmed that CCTA combined with adenosine stress protocols such as CTP can provide insight into myocardial ischemia and its relation to relevant CAD localization. This reinforces the emerging notion that CCTA aided by a adenosine stress protocol could perhaps replace or complement other myocardial perfusion techniques such as PET or SPECT in specific patient cohorts (7).

Lastly, an evaluation was made using CCTA for quantifying left ventricular mass and wall thickness and compared with the gold standard of cardiac MRI using AI-driven segmentation showing excellent agreement. An alternative to MRI is especially important as patient may have insurmountable contraindications such as cardiac devices or claustrophobia (8). This further supports the idea of CCTA as a single modality capable of assessing coronary arteries, myocardial perfusion - by means of adding an adenosine stress protocol - and cardiac morphology.

What strengthens this thesis is the focus on automation -for example by leveraging AI algorithms- and consistent use of advanced image analysis techniques such as applying a Voronoi algorithm for myocardial segmentation.

However, there are also limitations. All studies were retrospective in nature and based om relatively small single-center cohorts, limiting generalizability. Although the review article on the utilization of serial CCTA for the assessment of plaque progression and/or regression included clinical endpoints none of the other studies include this feature. This prevents definitive conclusions about the prognostic implications of the derived metrics. However we do feel this is inherent to research focusing on the development of new technological methods for (aided) image analysis as is the case in this thesis. Furthermore, while AI tools improve efficiency, they can lack transparency, raising questions about model robustness across diverse datasets (9).

Conclusion and future perspectives

CCTA has become a widely used imaging modality for the detection of coronary artery stenosis with a high degree of diagnostic accuracy (10). As such, serial CCTA has become available in the assessment of plaque progression and or regression. Furthermore, it allows for studying the relationship of both quantitative and qualitative plaque features with regard to the prediction of plaque progression and MACE over time (11, 12). Following, the results of a review paper included in chapter 2 of this thesis is has been shown that not primarily qualitative plaque features but quantitative plaque features have the biggest impact on plaque progression and MACE. This underlies the potential importance for serial CCTA which is yet to be introduced in regular risk stratification of patients. With regard to further implementation of serial CCTA chapter 3 of this thesis describes the use of automatic co-registration of baseline and follow-up scans as well as development of patient specific cut-off values for determining plaque progression or regression for optimal usage of serial CCTA (1).

Addition of CTP to CCTA is beneficial as it allows for functional assessment of coronary artery stenosis which is crucial in the decision to revascularize patients (13). Nowadays, assessment of CTP is still done semi-quantitatively by visual analysis. In chapter 4 and 5 of this thesis it has been demonstrated that fully quantifying perfusion defects is possible and allows for quantitative correlation of hemodynamically significant lesions to areas of myocardial hypoperfusion. Furthermore, this allows for correlation of the "subtended mass"—the myocardial mass distal to a stenosis—with the area of myocardial hypoperfusion, demonstrating a good relationship with increasing stenosis degree.

The use of CCTA has been primarily focussed on coronary artery stenosis assessment yet with regard to its increasing spatial resolution other potential uses arise such as LV

dimension assessment (14). To this day cardiac MRI remains the gold standard when it comes to LV dimension assessment (15). Assessment of LV dimensions is crucial as both LV hypertrophy and LV wall thickness are independent risk factors of cardiac death (16). This thesis has demonstrated that CCTA has proven to be a reliable alternative for LV mass and LV wall thickness assessment as compared to MRI. This process may be further optimized by use of machine learning for LV contour placement on both CCTA and MRI allowing for substantial time gain as is pointed out before in several other studies (17, 18).

With the coming age of quantum computing and artificial intelligence it is interesting to see how these processes may be automated further in the (near) future (19).

Recently, use of photon counting CT has emerged and is capable of very high resolution imaging due to its increased spatial and temporal resolution which is essential for the assessment of small structures such as coronary plaques (20). Phantom studies have also demonstrated the feasibility of photon counting CT for the accurate quantification of iodine concentrations across various levels and body sizes, this is especially vital for the potential use of photon counting CT in the assessment of myocardial ischemia (21). Current assessment of iodine maps using standard multidetector CT scanners is often hindered due to beam hardening and other artefacts. As such photon counting CT may prove especially useful by reducing these artefacts along its increased spatial and temporal resolution (22). Furthermore, the ability to count photon numbers and energy enables the reconstruction of multienergy spectral images allowing for material decomposition analysis and thus better characterization of plaques. As such photon counting CT offers numerous potential advantages as compared to current standard multidetector CT scanners and is highly likely to be routinely used in CCTA assessment in the future (23). In this thesis photon counting CT was highlighted due to its direct relevance to CCTA and CTP for atherosclerosis and ischemia assessment as well as use of CCTA for LV morphology analysis, which are central to the studies presented. However, photon counting CT represents just one of several highly anticipated innovations in cardiac imaging. For example, fluripiridaz PET/CT is another notable advancement and has demonstrated superior image quality, higher diagnostic accuracy and lower radiation exposure as compared to traditional SPECT imaging. As such, fluripiridaz PET/CT is particularly advantageous in myocardial perfusion imaging, hereby offering improved detection of coronary artery disease (24).

Henceforth, a combination of easy-to-use tools aided by artificial intelligence and increased image quality will pave the route for new frontiers in cardiovascular imaging.

References

1. Cao Q, Broersen A, Kitslaar PH, Yuan M, Lelieveldt BPF, Dijkstra J. Automatic coronary artery plaque thickness comparison between baseline and follow-up CCTA images. Med Phys. 2020;47(3):1083-93.
2. Han D, Kolli KK, Al'Aref SJ, Baskaran L, van Rosendael AR, Gransar H, et al. Machine Learning Framework to Identify Individuals at Risk of Rapid Progression of Coronary Atherosclerosis: From the PARADIGM Registry. J Am Heart Assoc. 2020;9(5):e013958.
3. Lee SE, Sung JM, Andreini D, Al-Mallah MH, Budoff MJ, Cademartiri F, et al. Differences in Progression to Obstructive Lesions per High-Risk Plaque Features and Plaque Volumes With CCTA. JACC Cardiovasc Imaging. 2020;13(6):1409-17.
4. Motoyama S, Ito H, Sarai M, Kondo T, Kawai H, Nagahara Y, et al. Plaque Characterization by Coronary Computed Tomography Angiography and the Likelihood of Acute Coronary Events in Mid-Term Follow-Up. J Am Coll Cardiol. 2015;66(4):337-46.
5. van Rosendael AR, Lin FY, van den Hoogen IJ, Ma X, Gianni U, Al Hussein Alawamlh O, et al. Progression of whole-heart Atherosclerosis by coronary CT and major adverse cardiovascular events. J Cardiovasc Comput Tomogr. 2021;15(4):322-30.
6. Garg PK, Bhatia HS, Allen TS, Grainger T, Pouncey AL, Dichek D, et al. Assessment of Subclinical Atherosclerosis in Asymptomatic People In Vivo: Measurements Suitable for Biomarker and Mendelian Randomization Studies. Arterioscler Thromb Vasc Biol. 2024;44(1):24-47.
7. Pontone G, Rossi A, Gimelli A, Neglia D. Should we choose CT angiography first instead of SPECT/PET first for the diagnosis and management of coronary artery disease? Atherosclerosis. 2023;385.
8. Sammet S. Magnetic resonance safety. Abdom Radiol (NY). 2016;41(3):444-51.
9. Fehr J, Citro B, Malpani R, Lippert C, Madai VI. A trustworthy AI reality-check: the lack of transparency of artificial intelligence products in healthcare. Front Digit Health. 2024;6:1267290.
10. Knuuti J, Ballo H, Juarez-Orozco LE, Saraste A, Kolh P, Rutjes AWS, et al. The performance of non-invasive tests to rule-in and rule-out significant coronary artery stenosis in patients with stable angina: a meta-analysis focused on post-test disease probability. Eur Heart J. 2018;39(35):3322-30.
11. Weber C, Deseive S, Brim G, Stocker TJ, Broersen A, Kitslaar P, et al. Coronary plaque volume and predictors for fast plaque progression assessed by serial coronary CT angiography-A single-center observational study. Eur J Radiol. 2020;123:108805.
12. Yu M, Li W, Lu Z, Wei M, Yan J, Zhang J. Quantitative baseline CT plaque characterization of unrevascularized non-culprit intermediate coronary stenosis predicts lesion volume progression and long-term prognosis: A serial CT follow-up study. Int J Cardiol. 2018;264:181-6.
13. Neumann FJ, Sousa-Uva M, Ahlsson A, Alfonso F, Banning AP, Benedetto U, et al. 2018 ESC/EACTS Guidelines on myocardial revascularization. Eur Heart J. 2019;40(2):87-165.
14. Tatsugami F, Higaki T, Kawashita I, Fukumoto W, Nakamura Y, Matsuura M, et al. Improvement of Spatial Resolution on Coronary CT Angiography by Using Super-Resolution Deep Learning Reconstruction. Acad Radiol. 2023;30(11):2497-504.
15. Fulton N, Rajiah P. Utility of magnetic resonance imaging in the evaluation of left ventricular thickening. Insights Imaging. 2017;8(2):279-93.
16. Haider AW, Larson MG, Benjamin EJ, Levy D. Increased left ventricular mass and hypertrophy are associated with increased risk for sudden death. J Am Coll Cardiol. 1998;32(5):1454-9.
17. Koo HJ, Lee JG, Ko JY, Lee G, Kang JW, Kim YH, et al. Automated Segmentation of Left Ventricular Myocardium on Cardiac Computed Tomography Using Deep Learning. Korean J Radiol. 2020;21(6):660-9.
18. Alabed S, Alandejani F, Dwivedi K, Karunasaagarar K, Sharkey M, Garg P, et al. Validation of Artificial Intelligence Cardiac MRI Measurements: Relationship to Heart Catheterization and Mortality Prediction. Radiology. 2022;304(3):E56.
19. Wei L, Liu H, Xu J, Shi L, Shan Z, Zhao B, et al. Quantum machine learning in medical image analysis: A survey. Neurocomputing. 2023;525:42-53.
20. Meloni A, Cademartiri F, Positano V, Celi S, Berti S, Clemente A, et al. Cardiovascular Applications of Photon-Counting CT Technology: A Revolutionary New Diagnostic Step. J Cardiovasc Dev Dis. 2023;10(9).
21. Leng S, Zhou W, Yu Z, Halaweish A, Krauss B, Schmidt B, et al. Spectral performance of a whole-body research photon counting detector

CT: quantitative accuracy in derived image sets. Phys Med Biol. 2017;62(17):7216-32.
22. Sharma SP, Lemmens MDK, Smulders MW, Budde RPJ, Hirsch A, Mihl C. Photon-counting detector computed tomography in cardiac imaging. Neth Heart J. 2024;32(11):405-16.
23. Williams MC, Newby DE. Photon-counting CT: A Step Change Leading to a Revolution in Coronary Imaging. Radiology. 2023;307(5):e231234.
24. Maddahi J, Agostini D, Bateman TM, Bax JJ, Beanlands RSB, Berman DS, et al. Flurpiridaz F-18 PET Myocardial Perfusion Imaging in Patients With Suspected Coronary Artery Disease. J Am Coll Cardiol. 2023;82(16):1598-610.

Appendices

Dutch summary

Hoofdstuk 1 bevat de algemene introductie en scriptieopzet. Coronary computed tomography angiography (CCTA) gecombineerd met computed tomography perfusion (CTP) maakt het mogelijk om een kwantitatieve, kwalitatieve en functionele beoordeling uit te voeren van coronary artery disease (CAD). Myocardiale segmentatie door middel van een Voronoi algoritme in combinatie met de kwantificatie van myocardiale ischemie bij CTP maakt het mogelijk om deze laatste kwantitatief te correleren aan de corresponderende locatie van de coronairstenose, hetgeen van essentieel belang is voor een eventuele revascularisatie. Naar aanleiding van het wijdverspreide gebruik van CCTA is het gebruik van seriële CCTA de laatste jaren in opkomst voor de beoordeling van veranderingen in plaque hoeveelheid en morfologie. Technologische vooruitgang maakt automatische registratie van baseline en follow-up coronair scans mogelijk waarbij ook een kwantitatieve analyse van plaque veranderingen kan worden verricht. Specifieke vooruitgang bij de beeldkwaliteit van CCTA heeft ertoe geleid dat CCTA ook gebruikt kan worden voor de beoordeling van left ventricle (LV) dimensies, een taak welke tot op heden vooral wordt uitgevoerd door magnetic resonance imaging (MRI). **Hoofdstuk 2** bevat een review artikel welke ingaat op het gebruik van seriële CCTA voor de voorspelling van plaque progressie en major adverse cardiac events (MACE). De volgende onderwerpen worden beschreven; Kwantitatieve baseline plaque kenmerken alsmede kwantitatieve plaque veranderingen zijn meer voorspellend voor MACE en/of plaque progressie vergeleken met kwalitatieve plaque kenmerken. Daarnaast werd een hoger epicardial fat volume (EFV) bij baseline geassocieerd met de progressie of ontwikkeling van coronair plaque. Seriële CCTA is ook bewezen effectief gebleken bij de beoordeling van de effectiviteit van statine therapie op plaque progressie. Hierbij is het bewezen dat statines de algehele progressie van het atherosclerose volume vertraagde en een toename induceerde van gecalcificeerde plaque met een afname van high risk plaque features. Toch kent seriële CCTA nog uitdagingen waaronder het gebruik van verschillende scanners bij baseline en follow-up scans hetgeen zal leiden tot een variabiliteit in gemeten plaque volumes. Dit onderstreept het belang van gestandaardiseerde acquisitie protocollen voor zowel baseline als follow-up CT scans. Tevens is er tot op heden geen expert consensus beschikbaar wat betreft het ideale inter-scan interval tussen baseline en follow-up CT scans, alhoewel recente studies hebben aangetoond dat mogelijk een interval van 1-2 jaar kan worden gebruikt. **Hoofdstuk 3** beschrijft het gebruik van patiënt specifieke afkapwaarden voor het bepalen van plaque progressie en/of regressie op seriële CCTA. Contouring van de coronaire vaatwand en het lumen is nodig voor plaque kwantificatie, hetgeen essentieel is voor de beoordeling van CAD bij zowel CCTA als seriële CCTA. Accuraatheid van de contour plaatsing is afhankelijk van de scankwaliteit welke gekwantificeerd kan worden met behulp van de contrast-to-noise ratio (CNR). Zodoende zijn er afkapwaarden nodig om te kunnen differentiëren tussen reële veranderingen in plaque dikte en veranderingen veroorzaakt door inacuraatheid van de contouren. Een cohort van vijftig patiënten welke CCTA hebben

ondergaan en elk beschikt over 2 scanfasen werd gebruikt voor contourplaatsing van in totaal 300 coronairen, hierbij werd tevens voor elk vat de CNR berekend. De gemiddelde CNR was 13.4 ± 3.6. De gemiddelde positieve en negatieve verschillen in gemeten plaque dikte waren 0.7 ± 0.3 en -0.9 ± 0.6mm respectievelijk. De inter-observer correlatie voor de CNR waarden was uitstekend met een correlatiecoëfficiënt van 0.872 ($p<0.001$). Gevonden plaque verschillen tussen deze twee scan fasen kunnen worden veroorzaakt door inacuraatheden in de contour plaatsing, aangezien plaque verschillen tussen twee scanfasen van dezelfde patient op dezelfde tijd altijd nul moeten zijn. Vervolgens werden de grootste positieve en negatieve plaque verschillen uitgezet tegen de vaat specifieke CNR. De gecreëerde grafieken toonde een lichte trend waarbij grotere plaque verschillen overeen kwamen met een lagere CNR. Een lineaire regressie analyse werd toegepast op deze grafieken zodat vaat specifieke en patiënt specifieke afkapwaarden kunnen worden verkregen, gebaseerd op de vaat specifieke CNR. **Hoofdstuk 4** toont de mogelijkheid voor volledige kwantificatie van myocardiale perfusiedefecten zoals vastgesteld met CTP. Tegenwoordig wordt CTP nog steeds beoordeeld op een semi-kwantitatieve manier met behulp van visuele analyse. Echter, volledige kwantificatie van myocardiale perfusie defecten en bijhorende myocardiale massa distaal van de stenose lijkt wenselijk aangezien het dan mogelijk is om de distributie van myocardiale ischemie te koppelen aan de coronair stenose(n). Drieëndertig patiënten met een gecombineerd CCTA en CTP protocol met beelden van goede of uitstekende scankwaliteit werden geanalyseerd middels het Voronoi algoritme. Dit algoritme maakt het mogelijk om weefsel te verdelen in segmenten op basis van welk bloedvat het dichtst in de buurt ligt. In totaal werden 64 coronair stenosen geanalyseerd. Gemiddelde waarden voor de totale massa distaal van de coronair stenose(n), massa per stenose, perfusiedefect massa en perfusiedefect massa per stenose waren 69, 36, 7 en respectievelijk 3 gram. Bij 19/33 patiënten (58%) kon de totale perfusiedefect massa worden verdeeld over de relevante coronair stenose(n). **Hoofdstuk 5** onderzoekt de relatie tussen het gekwantificeerde myocardiale gebied "at risk" door een stenose en het gekwantificeerde gebied van myocardiale ischemie. Tweeënveertig patiënten met een gecombineerd CCTA en CTP protocol en op zijn minst een stenose van ≥ 50% op CCTA werden geselecteerd voor analyse. Het myocardiale gebied "at risk" werd berekend met behulp van een Voronoi segmentatie algoritme en werd gedefinieerd als de som van alle myocardiale gebieden gerelateerd aan een ≥ 50% stenose als percentage van de totale LV massa. De ischemische "burden" werd berekend als het gekwantificeerde gebied van myocardiale ischemie als percentage van de totale LV massa. LV contouren werden automatisch geplaatst met behulp van een machine learning algoritme. In totaal werden 77 coronaire lesies beoordeeld met een luminale stenose van ≥ 50%. Er werd een separate analyse uitgevoerd voor stenosen van ≥ 50% en ≥ 70%. Het gemiddelde myocardiale gebied "at risk" voor stenosen van ≥ 50% en ≥ 70% was respectievelijk 59% en 37%. Gemiddelde ischemische "burden" voor stenosen van ≥ 50% en ≥ 70% was respectievelijk 23% en 24%. Er was een matige correlatie tussen de ischemische "burden" en het myocardiale gebied "at risk" bij een stenose van ≥ 50% ($r = 0.564$; $p < 0.01$). Een goede correlatie werd gevonden voor stenosen van ≥ 70% ($r =$

0.708; p < 0.01). **Hoofdstuk 6** beschrijft het gebruik van CCTA voor LV massa en wanddikte bepaling, vergeleken met de gouden standaard, MRI. Zevenenvijftig patiënten met zowel een beschikbare CCTA en MRI met een interscan interval van maximaal 6 maanden werden geanalyseerd. Gemiddelde LV massa en wanddikte voor CCTA en cardiale MRI waren respectievelijk 127 gram, 128 gram, 7mm en 8mm. Bland-Altman grafieken toonde gemiddelde verschillen en een 95% betrouwbaarheidsinterval voor de mate van overeenstemming van –1.26 (25.06; –27.58) en –0.57 (1.78; –2.92), respectievelijk voor LV massa en gemiddelde LV wanddikte. Gemiddelde verschillen en corresponderende 95% betrouwbaarheidsintervallen voor wanddikte per regio waren respectievelijk –0.75 (1.34;–2.83), –0.58 (2.14; –3.30), en –0.29 (3.21; –3.79) voor basale, middelste en apicale regio's. Gebruik van CCTA voor de beoordeling van LV dimensies is mogelijk en toont een goede overeenstemming met cardiale MRI.

List of publications

Comparison of left ventricular mass and wall thickness between cardiac computed tomography angiography and cardiac magnetic resonance imaging using machine learning algorithms (journal article)
van Driest, Finn Y | van der Geest, Rob J | Omara, Sharif K | Broersen, Alexander | Dijkstra, Jouke | Jukema, J Wouter | Scholte, Arthur J H A
European Heart Journal - Imaging Methods and Practice, volume 2, issue 3 (2024).
10.1093/ehjimp/qyae069

Automatic Quantification of Local Plaque Thickness Differences as Assessed by Serial Coronary Computed Tomography Angiography Using Scan-Quality-Based Vessel-Specific Thresholds (journal article)
van Driest, Finn Y. | Broersen, Alexander | van der Geest, Rob J. | Wouter Jukema, J. | Scholte, Arthur J. H. A. | Dijkstra, Jouke
Cardiology and Therapy, volume 13, issue 1, pages 103-116 (2024).
10.1007/s40119-023-00341-6

Utilizing (serial) coronary computed tomography angiography (CCTA) to predict plaque progression and major adverse cardiac events (MACE): results, merits and challenges (journal article)
van Driest, F. Y. | Bijns, C. M. | van der Geest, R. J. | Broersen, A. | Dijkstra, J. | Scholte, A. J. H. A. | Jukema, J. W.
European Radiology, volume 32, issue 5, pages 3408-3422 (2022).
10.1007/s00330-021-08393-9

Transmural ischemia visualized using routine Chest CTA (journal article)
van Driest, F.Y. | Hertgers, O | Scholte, A.J.H.A. | Jukema, J.W. | de Graaf, M.A.
Radiology Case Reports, volume 17, issue 5, pages 1734-1736 (2022).
10.1016/j.radcr.2022.03.019

Correlation between quantification of myocardial area at risk and ischemic burden at cardiac computed tomography (journal article)
van Driest, F.Y. | Bijns, C.M. | van der Geest, R.J. | Broersen, A. | Dijkstra, J. | Jukema, J.W. | Scholte, A.J.H.A.
European Journal of Radiology Open, volume 9 (2022).
10.1016/j.ejro.2022.100417

COVID-19 associated perimyocarditis (journal article)
van Driest, Finn Y. | Fejzovic, Vedad | Scholte, Arthur J.H.A. | Jukema, J. Wouter | Lamb, Hildo J.
Magnetic Resonance Imaging, volume 84 (2021).
10.1016/j.mri.2021.08.012

Quantification of myocardial ischemia and subtended myocardial mass at adenosine stress cardiac computed tomography: a feasibility study (journal article)
van Driest, F. Y. | van der Geest, R. J. | Broersen, A. | Dijkstra, J. | el Mahdiui, M. | Jukema, J. W. | Scholte, A. J. H. A.
The International Journal of Cardiovascular Imaging, volume 37, issue 11, pages 3313-3322 (2021).
10.1007/s10554-021-02314-z

A case of tortuous anatomy: cervical aortic arch (journal article)
van Driest, Finn Y | Stöger, J Lauran | Scholte, Arthur J H A | Jukema, J Wouter | Egorova, Anastasia D
European Heart Journal, volume 42, issue 18, pages 1811-1811 (2021).
10.1093/eurheartj/ehaa713

Early nerve repair in traumatic brachial plexus injuries in adults: treatment algorithm and first experiences (journal article)
Pondaag, Willem | van Driest, Finn Y. | Groen, Justus L. | Malessy, Martijn J. A.
Journal of Neurosurgery, volume 130, issue 1, pages 172-178 (2018).

CV

Finn van Driest was born on the 12th of April 1990 in The Hague. He attended the atheneum of the Montessori high school in that same city. Hereafter, he went on to study medicine at Leiden University. On finishing his medical studies he worked as a senior house officer in clinical addiction care within a large rehabilitation clinic in Utrecht. Missing the thrill of intramural medicine and looking for more clinical experience he joined the cardiology department at the Leiden University Medical Centre as a senior house officer. With a great interest in cardiac imaging he was awarded a PhD position in that same department under supervisor of Prof Jukema and Dr Scholte. Fond of medical technology and imaging he now resides as a 3rd year radiology resident in the same institution. (Head of department: Prof Bennink. Residency supervisor: Dr Pereira Arias-Bouda)

Acknowledgements

This thesis has been written at the cardiology department of the Leiden University Medical Center. I have very much enjoyed my time at this department and have learned tremendously along the way. This has been a period that has helped me grow not only scientifically, but also socially and personally. Fond am I of the many memories of inspiring conferences, engaging lectures and fun moments shared with colleagues. I would hereby like to sincerely thank everyone that has contributed to this thesis one way or another.

Prof. Dr. Jukema, Promotor. Dear Wouter, I am extremely grateful for your guidance and support throughout this PhD journey, I owe it partly to you that I was given the opportunity to carry out this thesis with the cardiology department in collaboration with the division of image processing. Your enthusiasm for (cardiac) imaging—something that was especially obvious during our time together in the cardiac CT reading team - has been very contagious and has further inspired me greatly to indeed pursue a career in imaging.

Dr. Scholte, Copromotor. Dear Arthur, you have made an immense effort at the start of my PhD to make sure this trajectory would be possible and supported by both the cardiology department and the division of image processing. I greatly appreciate the way you have offered guidance but also gave me the freedom to tackle my PhD at my own desirable pace and partly according to my own ideas.

Dear members of the imaging division; Rob, Alexander and Jouke. Your support has been invaluable during the writing of this thesis. I could never have overcome the many hurdles without your help and out-of-the-box mindset. I am extremely grateful for helping me with the challenging technical aspects of this thesis.

Dear fellow researchers and CT reading team, I am extremely grateful for the fun and inspiring times we have had in the imaging room and beyond. The collective enthusiasm during CT readings has been a great motivation throughout my PhD. Fond am I of the group memories during ski trips and conferences both nationally and abroad. Not only have you brightened my working days, you have also given me friendships for life.

Dear parents, Jan and Carenza. Both of you have always shown a sincere interest in my research and working life which have been very motivating. You have always made it clear that ambitions should be strived for but have also shown me the beauty and importance of all things outside of work. I am lucky to be your son and to have seen so much of the world already.

Dearest Floor, you have always been a great support during my PhD journey and large part of my medical career. You have always had my back especially during late night working days and have always encouraged me to keep going. Our many trips together

and passion for food have always been a great escape from the busy working life and I hope to go on many more.